BENCHMARKING AND SAFETY ASSESSMENT FOR MODIFIED LATERAL SPREADING DESIGN PROCEDURE USING THREE-DIMENSIONAL NONLINEAR FINITE ELEMENT ANALYSIS

FINAL PROJECT REPORT

by

Christopher R. McGann and Partha S. Bhattacharjee
Washington State University

Sponsorship
PacTrans

for
Pacific Northwest Transportation Consortium (PacTrans)
USDOT University Transportation Center for Federal Region 10
University of Washington
More Hall 112, Box 352700
Seattle, WA 98195-2700

In cooperation with US Department of Transportation-Research and Innovative Technology Administration (RITA)

Disclaimer

The contents of this report reflect the views of the authors, who are responsible for the facts and the accuracy of the information presented herein. This document is disseminated under the sponsorship of the U.S. Department of Transportation's University Transportation Centers Program, in the interest of information exchange. The Pacific Northwest Transportation Consortium, the U.S. Government and matching sponsor assume no liability for the contents or use thereof.

Technical Report Documentation Page

1. Report No.	2. Government Accession No.	3. Recipient's Catalog No.

4. Title and Subtitle	5. Report Date
Benchmarking and Safety Assessment for Modified Lateral Spreading Design Procedure Using Three-Dimensional Nonlinear Finite Element Analysis	6/30/3017
	6. Performing Organization Code

7. Author(s)	8. Performing Organization Report No.
Christopher McGann, Partha Bhattacharjee	

9. Performing Organization Name and Address	10. Work Unit No. (TRAIS)
PacTrans Pacific Northwest Transportation Consortium University Transportation Center for Region 10 University of Washington More Hall 112 Seattle, WA 98195-2700	**11. Contract or Grant No.** DTRT13-G-UTC40

12. Sponsoring Organization Name and Address	13. Type of Report and Period Covered
United States of America Department of Transportation Research and Innovative Technology Administration	Research 6/1/2016-7/1/2017
	14. Sponsoring Agency Code

15. Supplementary Notes

Report uploaded at www.pacTrans.org

16. Abstract

Liquefaction-induced lateral spreading is a critical design consideration for many bridges in high-seismicity regions of the Pacific Northwest, with broad impacts on safety for the general public. The bridge design procedures currently used in the region tend to account for the effects of lateral spreading in a simplified manner that captures the general impact of this phenomenon on the bridge components but omits many key details such as three-dimensional soil deformation. Modifications to this current design approach will not only lead to more cost-effective design solutions, but will increase public safety by reducing the potential for bridge collapse and minimizing lost service time. An improved design framework has been proposed to supplant the current method; however, relatively little focus has been given to the validation and verification of this new procedure. Before widespread acceptance of this modified approach, it is critical to verify that its application will result in improved design solutions that reduce the costs associated with the conventional approach while remaining safe for use. This work aims to verify the modified simplified design procedure against 3D finite element models and to increase our understanding of the site geometry conditions that necessitate a more comprehensive consideration of 3D effects in foundation design by using a large parameter study.

17. Key Words	18. Distribution Statement
Bridge foundations; lateral spreading; pile pinning; 3D FEA	No restrictions.

19. Security Classification (of this report)	20. Security Classification (of this page)	21. No. of Pages	22. Price
Unclassified.	Unclassified.		NA

Form DOT F 1700.7 (8-72) **Reproduction of completed page authorized**

Table of Contents

List of Figures

List of Tables

Acknowledgments

The authors would like to thank the Pacific Northwest Transportation Consortium for funding and supporting this work. We also wish to thank Tony Allen from the Washington State Department of Transportation for providing the original inspiration for this research, as well as Professor Pedro Arduino at the University of Washington for providing key insights and guidance. Lastly, the authors would like to thank the NHERI DesignSafe-CI team at TACC and QuakeCoRE for providing the additional computational resources needed to complete the large number of complex analyses that this research required in a timely manner.

Executive Summary

Liquefaction-induced lateral spreading is a critical design consideration for many bridges in high-seismicity regions of the Pacific Northwest, with broad impacts on safety for the general public. For designing bridge foundations in seismic regions, particularly the foundations near approach embankments, the forces engaged by the foundations due to liquefaction-induced lateral spreading and pile pinning become important. Bridge foundation design procedures for this load case typically make use of simplifying assumptions because of the complexity of the problem. The most common current approach is an equivalent static analysis (ESA) procedure based on a two-dimensional pile pinning concept. This ESA approach is able to adequately account for the forces on the bridge foundation; however, relatively little validation or verification efforts have been undertaken. Additionally, the current simplified approach does not offer much guidance on the expected level of foundation pinning because of the three-dimensional aspects of the problem. Before widespread application of this ESA approach, it is critical to verify that it will result in improved design solutions that reduce the costs associated with the conventional approach while keeping bridges safe for use. This work aims to verify the modified simplified design procedure against 3D finite element models, and to increase our understanding of the site geometry conditions that necessitate a more comprehensive consideration of 3D effects in foundation design by using a large parameter study.

The aims of this study were encompassed by two primary objectives related to the lateral spreading bridge foundation analysis problem:

(1) Identify the critical site geometry features that lead to reductions in foundation demands because of 3D (or other) effects and analyze the relative demands on the

foundation considering the full three-dimensionality of a site by using 3D finite element analysis (FEA).

(2) Further investigate the problem and verify an existing ESA procedure for the lateral spreading case by comparing the results from ESA and 3D FEA procedures for identical cases

These objectives were accomplished by analyzing 200 distinct cases using both 3D FEA and simplified ESA models of the soil-foundation system. The cases for these parameter studies considered different combinations of bridge approach embankment width, non-liquefiable crust thickness, liquefiable layer thickness, and foundation size/stiffness. The 3D FEA models considered a continuum representation for the soil domain, displacement based beam-column elements for the shaft foundation, and beam-to-solid contact elements that enabled kinematically consistent consideration of the soil-foundation interface. The demands of lateral spreading on the foundation were introduced in these models through the application of an applied lateral displacement profile, based on a simplified shear strain profile, to the free-field boundaries of the models. The ESA models comprised two sub-models, a beam on nonlinear Winkler foundation model used to assess the effects of lateral spreading on the foundation, and a pseudostatic limit equilibrium slope stability model that provided the expected levels of deformation, given a set foundation resisting force and seismic demand.

The parameter studies carried out during this research indicated that consideration for the 3D geometry of the bridge site results in tangible changes in the foundation bending demands and abutment displacements in comparison to those corresponding to the free-field lateral spreading demands. Increasing approach embankment width results in less foundation pinning and greater foundation bending demands, and these effects can be offset by increasing the size or stiffness of the embedded deep foundations. The results of both modeling efforts also indicated

that there is a limiting thickness of non-liquefiable crust after which the significance of 3D effects on the bridge abutment foundation demands is sharply reduced. Additionally, the ESA parameter study identified that for the simplified flat soil profiles considered in this work and a constant seismic demand, there is a tendency for the method to return overall lateral spreading deformations that decrease sharply with increasing crust thickness because of the decreased likelihood for the development of significant deformations in these configurations. The results of the ESA parameter study also identified a tendency for increasing overall deformations with increasing thickness of the liquefied layer because of similar (but reverse) mechanisms.

Perhaps most importantly, the agreement identified between the results of the 3D FEA and the simplified ESA methods, when applied to the same set of site configurations, provided verification for both modeling approaches. This verification is particularly important in regard to the ESA procedure, as the agreement between the two approaches provided further indication that this simplified method is consistent with a fully three-dimensional description of the lateral spreading bridge foundation system. Given the practical nature of this approach, it is far more likely to be used for foundation assessment, and this verification is a critical benchmarking step.

Chapter 1 Introduction

Liquefaction-induced lateral spreading is a critical design consideration for many bridges located in high seismicity regions of the Pacific Northwest, and worldwide, with broad economic and safety impacts for the general public. The bridge design procedures traditionally used in the region (e.g., WSDOT, 2011a,b) tend to account for the effects of lateral spreading on the bridge and foundations with a simplified analytical approach based on a plane strain description of the site geometry. This analytical approach captures the general impact of the lateral spreading event on the bridge components in a conservative manner, but to because of the omission of several key details (e.g., 3D soil deformation, foundation pinning effects), the use of this approach in design may result in overly conservative and expensive solutions. In some cases, this over-conservatism limits the feasibility of entire bridge projects.

Numerous bridges affected by lateral spreading during past earthquakes have displayed three-dimensional (3D) soil deformation effects, and evidence from a traditional simplified plane strain lateral spreading analysis has suggested that these 3D deformations have reduced the demands imposed upon the bridge foundations relative to what was returned. Such responses have been observed in Japan (Hamada and O'Rourke, 1992), Central and South America (Youd, 1993; GEER, 2010a; FHWA, 2011; Ledezma et al., 2012), and New Zealand (GEER, 2010b, 2011; Cubrinovski et al., 2014), among others. In many of these documented cases, it has also become apparent that the bridge and foundations altered the near-field deformation during lateral soil movement (the foundation pinning effect). Because the resistance provided by the bridge led to a reduction in the near-field displacement demand, the corresponding structural demands on the bridge and foundations were less than would be expected under the full free-field displacement demand. Because of this difference between the near and free-field deformations,

an analysis procedure that assesses the foundation response to the free-field lateral spreading displacements can be overly conservative.

An improved simplified analytical framework (Martin et al., 2002; Zha, 2004; Ashford et al., 2011) based on compatibility between the foundation and soil displacements during lateral soil flow (the pile pinning concept) has been proposed as an alternative to the plane strain procedures historically used to analyze this problem. This analytical framework separates the problem into two cases:

1. a restrained ground displacement case in which it is expected that foundation pinning will be significant, e.g., an approach embankment and bridge abutment;
2. an unrestrained ground displacement case in which it is assumed that the foundation resistance is minimal relative to the mass of displacing soil, e.g., an interior bridge pier.

The restrained ground case was of primary interest in the current study, as the main focus of this project was related to the verification of the recommended analysis approach for this case. The analysis procedure for the restrain ground case is based on an equivalent static analysis approach comprising three main steps:

1. Estimate the embankment displacement for a range of pile restraining forces by using limit equilibrium slope stability analysis.
2. Estimate the foundation restraining forces (internal shear force demand at the enter of the liquefiable layer) for a range of imposed ground displacements by using a beam on nonlinear Winkler foundation (BNWF) pushover analysis.
3. Determine the point of compatibility in the force-displacement curves obtained from the first two steps.

This pile pinning analysis framework is a marked improvement upon the assumption of plane strain; however, the equivalent static procedure overly simplifies the complex 3D problem, decouples the response of the soil layers in the profile, and restricts the analysis to simple scenarios that may not correlate well with actual conditions. Armstrong et al. (2014) also showed that the equivalent static pile pinning analysis procedure offers little insight into the complexities of the seismic response of the soil and structure, and both Armstrong et al. (2014) and McGann and Arduino (2014) found that it is sensitive to input parameters and analysis assumptions.

Relatively little focus has been given to the validation and verification of the equivalent static pile pinning analysis procedure for the restrained ground case, or to demonstrating its use for real bridge designs and site conditions. Previous studies that have validated or verified the pile pinning procedure against actual bridge performance (McGann and Arduino, 2014), centrifuge tests (Boulanger et al., 2006; Armstrong et al., 2014), or more sophisticated 3D numerical models (McGann and Arduino, 2014; Ghofrani et al., 2016) have demonstrated that despite the shortcomings of the assumptions associated with this approach, the compatible displacement solutions returned are consistent with the considered case histories, experiments, and numerical analyses. There is great potential for this procedure to produce more efficient lateral spreading foundation design solutions that reduce the unnecessary costs associated with the over-conservatisms of traditional simplified design approaches. This increased economic efficiency will be greatly beneficial to local agencies; however, before the simplified pile pinning analysis framework is widely accepted, it is critical to further validate, verify and demonstrate the use of this procedure.

For the unrestrained ground displacement case, it is assumed that no foundation pinning takes place and the analysis is essentially unchanged from current plane strain procedures. There

are several issues with this current approach. Firstly, the assumption of no foundation pinning is conservative, as post-earthquake reconnaissance (e.g., FHWA, 2011) has suggested that some foundation pinning may take place in such conditions, though the degree of foundation resistance that should be expected is not currently clear. Secondly, the distinction between restrained and unrestrained conditions is made entirely on engineering judgment; cases in which it is expected that foundation resistance will be significant are analyzed as restrained cases, and cases in which it is not expected that foundation resistance will be significant are analyzed as unrestrained. Just as it is important to validate, verify, and demonstrate the use of the restrained ground displacement case, it is equally important to provide further guidance on the boundary between restrained and unrestrained conditions and to provide the means with which to quantify the expected level of foundation pinning for a particular site and foundation. This guidance and quantification method can be achieved through an assessment of the critical 3D site geometries that influence the foundation pinning that may be expected at a particular site.

1.1 Scope of Work

The two primary research objectives of this study were achieved by using the specific actions detailed below. All of the numerical work was performed using the OpenSees finite element analysis (FEA) platform (McKenna, 1997, 2011; McKenna et al., 2010), an open-source computational framework maintained by the Pacific Earthquake Engineering Research (PEER) Center (unless explicitly noted otherwise). Both objectives were based on the results of a large parameter study carried out with a series of 3D finite element models. This parameter study was an expansion of the work begun by McGann and Arduino (2015), who considered 72 different site profiles/geometries, but determined that this was an insufficient number of cases with which to make a conclusive statement about the relationship between site geometry and soil profile and

the expected level of foundation pinning. The efforts undertaken to expand this original parameter study are detailed in Objective 1 below, as well as in subsequent chapters of this report.

Objective 1: Quantify the level of foundation pinning based on 3D geometric factors and further definition of the boundary between restrained and unrestrained ground displacement cases.

- Establish a new set of considered cases on the basis of the addition of new values for the site geometry terms considered by McGann and Arduino (2015). The additional cases considered in the current study included two new liquefiable layer thickness values and two new thicknesses for the non-liquefied crust below the approach embankment. These additions resulted in 128 new site geometries for the parameter study and a total of 200 distinct cases when combined with the original data set.
- Develop the nonlinear 3D FE models for the 128 new cases.
- Analyze the 128 new models by making use of high-performance computing (HPC) resources as needed to reduce the analysis time.
- Use the structural foundation demands (displacement, shear force, and bending moment) returned in the parameter study cases to quantify the expected level of foundation pinning for the considered site geometries though comparison with the free-field displacement demands. Develop a correlation or first-order prediction tool to be used in deciding whether a site should be analyzed as restrained or unrestrained and/or to inform the results of subsequent analyses.

Objective 2: Verify the simplified equivalent static pile pinning analysis procedure for a restrained ground displacement case.

- Conduct a detailed review of the restrained ground displacement analysis procedure discussed by Ashford et al. (2011), Boulanger et al. (2006), and Armstrong et al. (2014).
- Develop the models necessary to conduct simplified equivalent static pile pinning analyses of the 200 site profiles/geometries analyzed with 3D FEA. The necessary models include the following:
  - Laterally loaded foundation models analyzed with a beam on nonlinear Winkler foundation (BNWF) approach, with beam elements for the foundation and *p-y* spring elements to capture the soil-structure interaction. Obtain pushover curves describing the relationship between foundation shear force and surficial displacement.
  - Pseudo-static limit equilibrium slope stability models to assess the relationship between seismic demand (as represented by slope yield acceleration) and the foundation shear force required to resist the failure of the slope.
  - Newmark sliding block analysis to link the slope yield accelerations to lateral displacement demands and subsequently define a relationship between the expected lateral displacements and the shear force required to resist those displacements.
- Determine the compatible design displacement for each case through comparison of the force-displacement curves resulting from the pushover and slope stability analysis phases.
- Compare the results of the equivalent static pile pinning analysis procedure to the simulated foundation response from the 3D FE models to verify the results from each approach and to comment on the differences and similarities between the results of each method.

The work undertaken to achieve these two research objectives is discussed in the subsequent chapters of this report. The initial chapters present a review of the equivalent static analysis procedure and a discussion of the development of the parameter study cases considered. This is followed by discussions of the development of the models necessary to perform the 3D FEA and equivalent static analyses, as well as discussions of the individual results of these two parameter studies. These latter chapters also present and discuss the results in the context of objectives 1 and 2 of this study. Objective 2 is addressed through a comparison of the results of the two analysis types for the 200 site profiles/geometries in question, and Objective 1 is addressed by using the insights gained from each individual analysis type and the comparisons between them.

Chapter 2 Summary of Simplified Lateral Spreading Design Procedure and Considerations

A number of simplified design procedures have been developed for the case of bridge foundations subject to liquefaction-induced lateral spreading. These procedures vary in complexity, assumptions, and analysis techniques; however, the general approach is to determine the foundation demands for a given amount of free-field lateral spreading displacement while seeking a balance between simplicity of use and applicability to the problem. The simplified design approach considered in this work was an equivalent static analysis (ESA) procedure based on the pile pinning concept (Martin et al., 2002) as refined as expanded upon by other researchers (e.g., Zha, 2004; Boulanger et al., 2006) and fully synthesized by Ashford et al. (2011).

2.1 Equivalent Static Analysis Procedure

The equivalent static pile pinning analysis procedure of Ashford et al. (2011) is based on the NCHRP (2002) design recommendations, which effectively separate the lateral spreading design problem into two distinct cases:

(1) an unrestrained ground displacement case, in which it is assumed that the foundation is subject to a broad failure mass and will not provide significant resistance to lateral soil movement; and

(2) a restrained ground displacement case, in which it is assumed that the failure mass has a limited width and that the foundation provides resistance to soil deformation during lateral spreading (pile pinning).

The design processes for the restrained and unrestrained ground displacement cases, per Ashford et al. (2011), are described below.

2.1.1 Restrained Ground Displacement Case

The restrained design case applies to foundations that are assumed to provide partial restraint to soil flow during lateral spreading. The prototype for this case is an approach embankment acting on a pile-supported abutment, as shown schematically in figure 2.1. Because of the limited width of the approach embankment, it is assumed that the lateral stiffness of the abutment foundation will provide resistance to soil movement. The procedure recommended for this design case is based on the pile pinning analysis concept (Martin et al., 2002). In the pile pinning approach, a beam on nonlinear Winkler foundation (BNWF) model of the foundation is combined with a limit equilibrium slope stability analysis of the embankment and soil profile to determine the force-displacement state at which the resistance of the foundation is compatible with the deformation of the laterally spreading soil. This method consists of seven primary steps:

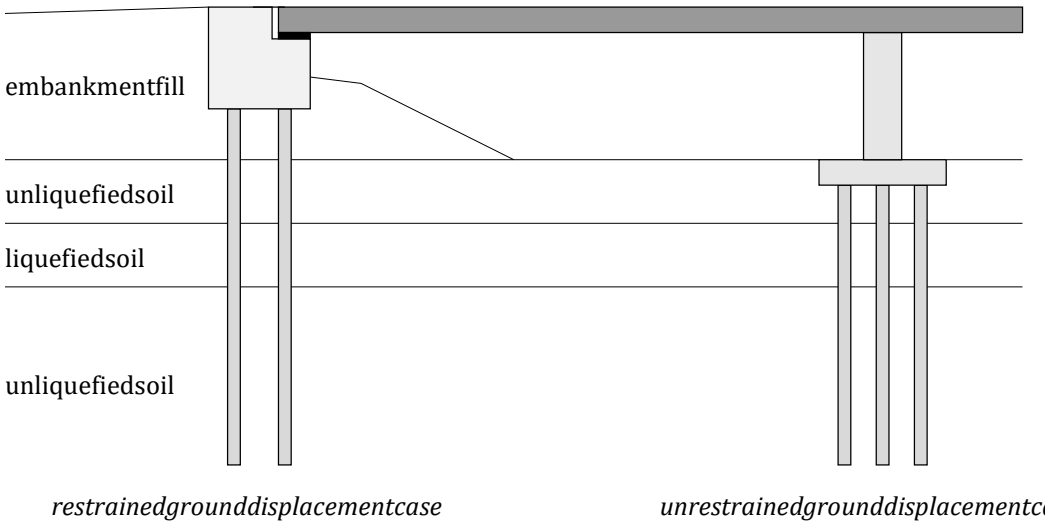

Figure 2.1 Prototype examples for restrained and unrestrained ground displacement cases.

1. **Assess liquefaction potential**. The liquefaction potential of the site soils is characterized for a peak ground acceleration (PGA) corresponding to a 5 percent in 50 years hazard. This is

typically accomplished by using a simplified approach (e.g., Youd et al., 2001). Per AASHTO (2010), the assumption of reduced strength due to pore pressure build-up or full liquefaction is required for soils that have a factor of safety against liquefaction of less than 1.2.

2. **Estimate the residual strength of liquefied soils**. Two options can be used to account for the residual strength of the *p-y* curves representing liquefied layers in the BNWF model of the soil-foundation system. No explicit preference for method is stated in Ashford et al. (2011).
   a. The *p*-multiplier (m_p) approach (e.g., Brandenberg et al., 2007b) may be used to obtain scaled *p-y* curves for liquefied soils on the basis of a sand-type backbone curve.
   b. The residual strength of the liquefied soil may be estimated by using an empirical method (e.g., Wang, 2003) and thus used as the ultimate resistance in the definition of *p-y* curves for liquefied soils on the basis of a clay-type backbone curve.
3. **Develop a foundation model**. The numerical BNWF model used to analyze the foundation requires definitions for the equivalent beam representing the foundation, the *p-y* curves for soil-pile interaction, and a force-displacement curve to capture abutment-embankment interaction. The commercial software LPILE is typically used for this purpose.
   a *Definition of equivalent beam:* The equivalent beam used to model the foundation (piles and cap/abutment) may be defined by assuming linear elastic or nonlinear elastoplastic behavior. In both cases, the spatial arrangement of the piles is largely ignored, and the equivalent beam is developed in a simplified manner. For linear elastic behavior, the equivalent beam model is obtained by multiplying the bending stiffness, *EI*, of a single pile by the number of piles in the group. For nonlinear behavior, the moment-curvature

response of a single pile is scaled by the number of piles in the group. The pile cap/abutment is incorporated into the equivalent beam by using a large linear elastic bending stiffness that approximates its rigidity relative to the piles. The rotational stiffness of the pile group is modeled by using a rotational restraint located at the connection of the piles to the cap/abutment. This restraint is assigned a stiffness equivalent to the estimated rotational stiffness of the pile group after Mokwa and Duncan (2003).

b *Definition of p-y curves for piles:* The *p-y* curves used for soil-pile interaction are based on the work of Matlock (1970) for soft clay, Reese and Welch (1975) for stiff clay, and Reese et al. (1974) for sand. The base *p-y* curves determined with these methods are modified to account for pile group effects and the effects of liquefaction.

- Group effects are considered by using a composite group efficiency factor computed as the average of the reduction factors for each row in the pile group, as recommended by Mokwa and Duncan (2001).
- The *p-y* curves of liquefied soils are defined as discussed in step 2. The influence of the weaker layer of liquefied soil on the surrounding material is accounted for by using a linearly smeared ultimate lateral resistance profile, as shown in figure 2.2.

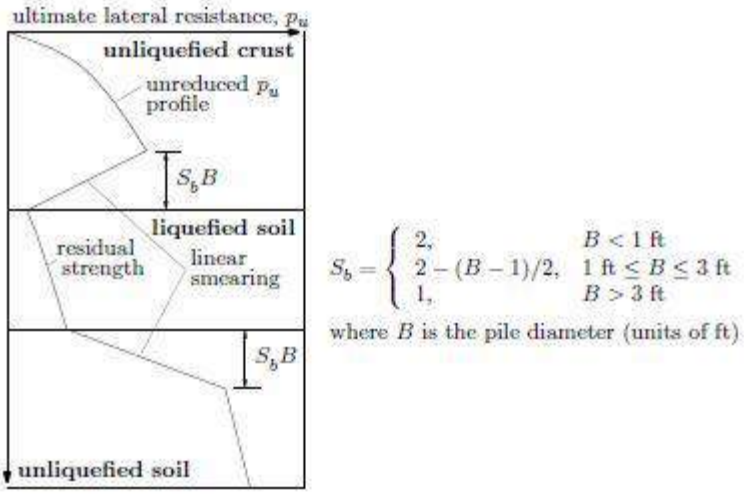

Figure 2.2 Profile of ultimate lateral resistance to account for the presence of the liquefied layer on the strength of the surrounding soil (after Ashford et al., 2011).

c. *Definition of cap/abutment-soil interaction curve:* A tri-linear force-displacement curve describing the interaction of the cap/abutment with the surrounding soil is defined by using the maximum passive load of the soil on the foundation, F_{ult}, and the displacement, Δ_{max}, required to mobilize this force. This curve is shown in figure 2.3. Two failure cases are considered to determine F_{ult}, with the lesser force controlling the design. The two cases are as follows:

- A log-spiral passive wedge acting on the cap/abutment combined with the lateral resistance provided by the portions of the piles extending through the crust (i.e., soil above the liquefied layer).
- A Rankine passive wedge acting on foundation elements above the liquefied layer, assuming that the cap/abutment, crust soil beneath the cap/abutment, and piles within the crust all act as a composite block.

The displacement, Δ_{max}, corresponding to the ultimate passive force is taken as the sum of 5 percent of the cap/abutment height with an adjustment factor that accounts for the effects of the depth of the liquefied material and the transverse thickness of the cap/abutment after Brandenberg et al. (2007a).

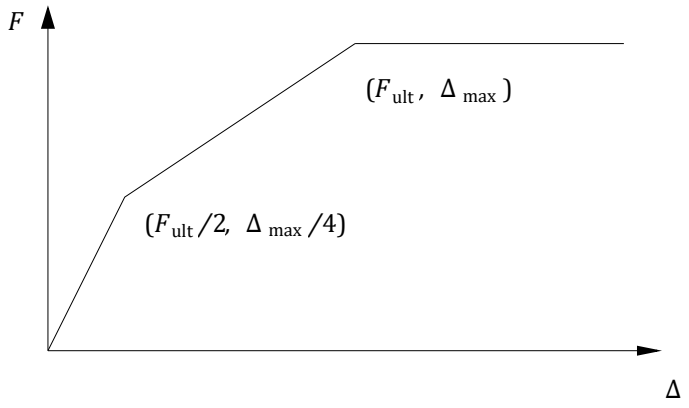

Figure 2.3 Tri-linear force-displacement curve for pile cap/abutment-soil interaction in foundation model (after Ashford et al., 2011).

4. **Displacement analysis of the foundation model**. Once the foundation model has been completed, a series of pushover analyses are conducted in which increasing crustal displacements are considered. Displacements are applied to the soil end of the *p-y* springs by using a prescribed displacement profile that simulates the effects of lateral spreading. The simplified displacement profile shown in figure 2.4 may be used for this purpose, or a displacement profile can be obtained by using a lateral displacement index approach (Zhang et al., 2004; Idriss and Boulanger, 2008). In this latter option, discussed in greater detail by Armstrong et al. (2014) and Cubrinovski et al. (2014), the estimated shear strains in the liquefiable soils are integrated with depth to achieve an approximate shape for the displacement profile.

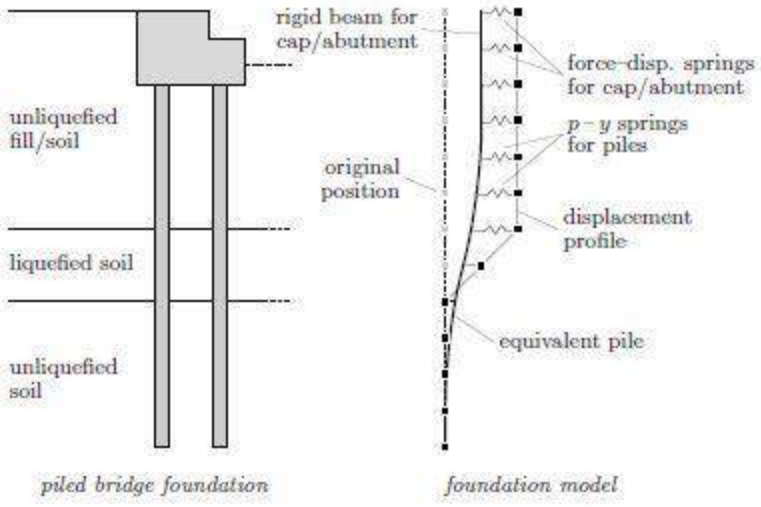

Figure 2.4 Transition from physical bridge foundation to foundation model showing the applied displacement profile for lateral spreading pushover analysis.

Once a displacement profile has been established, it is gradually imposed on the soil end of the *p-y* springs until a desired level of surface displacement has been achieved. During this incremental pushover analysis, the pile cap displacement and a running average of the shear force at the center of the liquefied layer are recorded to obtain a lateral spreading pushover curve for the foundation. The running average shear force for each displacement increment is computed as the sum of the current and all previous shear force values divided by the number of terms in the sum. This running average approach was introduced by Boulanger et al. (2006) to account for the discrepancy between the pushover analysis of this design step, in which the shear force increases with increasing ground displacement, and the slope deformation analyses of the next step, in which only constant foundation resisting forces are considered.

5. **Slope stability and deformation analysis of the approach embankment**. A pseudo-static slope stability model is used to determine foundation resisting forces, *R*, at the center of the

liquefied layer for a series of horizontal accelerations, k_h, applied in the model as a constant inertial force

$$F_h = k_h W \tag{2.1}$$

where W is the weight of the failure mass. For each considered acceleration value, the resisting force for which the slope factor of safety reaches 1.0 is recorded.

In these analyses, the restraining forces are applied on the lower edge of the failure surface, and the failure surface is constrained to the center of the liquefied layer, as depicted in figure 2.5. No specific recommendations on the slope stability analysis method are made, and various approaches have been used in previous studies. For example, Zha (2004) used the method of Janbu (1973) while Armstrong et al. (2014) used the non-circular surface method of Spencer (1967). When any analysis method is used, it is recommended that the failure surface be limited to extending ≤ 4 times the height of the embankment away from the bridge abutment. If it is assumed that the bridge deck will provide longitudinal resistance to abutment movement, a deck resisting force computed from the full passive resistance of the soil acting on the deck is applied during the slope stability analysis.

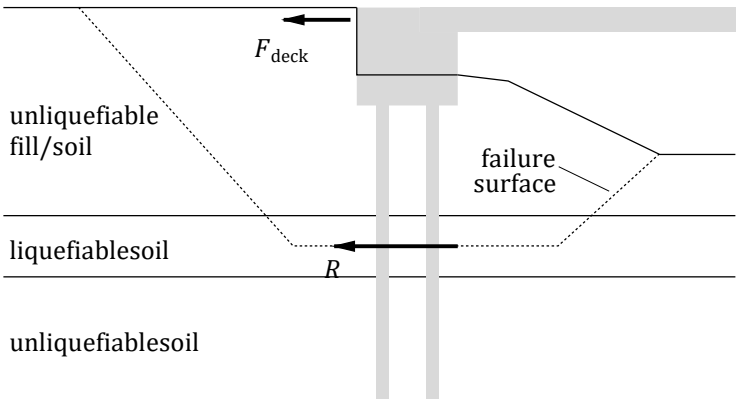

Figure 2.5 Schematic of slope stability analysis considering a deck resisting force, F_{deck}, and foundation resisting force, R.

Newmark's (1965) rigid sliding block analysis is used to compute the slope displacements corresponding to the k_h coefficients used to determine the resisting forces in the slope stability analyses. Typically, a simplified procedure (e.g., Bray and Travasarou, 2007) is used in lieu of site-specific sliding block analysis.

6. **Determine force-displacement compatibility**. The results of the pushover and slope stability/deformation analyses are used to determine a compatible force-displacement state that considers the restraining effects of the bridge foundation on the deformation of the soil-foundation system during lateral spreading. This is accomplished by plotting the slope force-displacement curve determined from the slope stability/deformation analyses (step 5) with the foundation running average shear force-displacement curve determined in the pushover analyses (step 4) in the manner shown in figure 2.6.

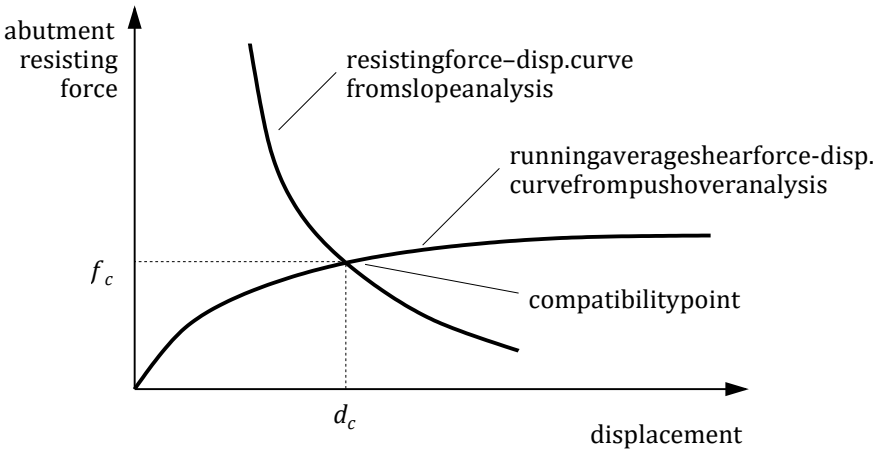

Figure 2.6 Determination of compatible force-displacement state.

The running average forces are used for the foundation force-displacement curve to account for the differences in how the resisting force is handled in the two curves (constant in the slope deformation curve, non-constant in the pushover curve). Because the resisting

forces obtained in the slope stability phase represent a force per unit thickness of soil, the lateral spreading pushover curve must be scaled by an appropriate width. The tributary width of the embankment proposed by Boulanger et al. (2006), determined as shown in figure 2.7, is used for this scaling.

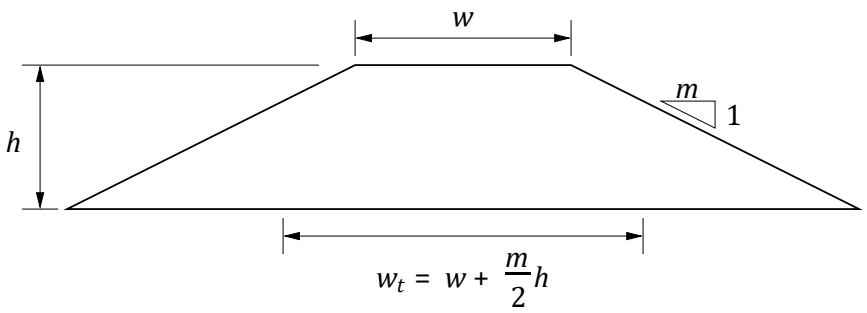

Figure 2.7 Tributary width of embankment, w_t (after Boulanger et al., 2006).

7. **Assess foundation performance**. The final performance evaluation for the foundation is conducted by using a lateral spreading pushover analysis, which considers the combined effects of kinematic and inertial loads. A kinematic loading is applied by using the specified displacement profile from step 4 with an applied surface displacement set as the compatible displacement, d_c, determined in step 6. Consideration for inertial effects is given during this analysis by applying 50 percent of the inertial loads from any associated superstructure or pile caps. The inertial effects of superstructure elements for typical bridge bents are considered by using an applied moment and shear force pair, which are determined on basis of the design of the bridge columns. There are two possibilities:
   a. In most cases, the bridge columns are designed to yield and develop plastic hinges prior to the onset of yield in the foundation elements. For this type of design, the inertial moment is set at 1.2 times the plastic moment capacity of the column. For columns that have a pinned connection at the top and a fixed connection at the bottom (free-fixed

configuration), the inertial shear force is determined by dividing this inertial moment by the height of the bridge column. For columns with a fixed-fixed configuration, the inertial shear force is set as the inertial moment divided by one-half the column height.

b. If the column is not expected to yield for the design event, then the inertial shear force is estimated as the product of the tributary mass carried by the bridge column with the spectral acceleration corresponding to the first mode of the column. The inertial moment is the product of the inertial shear force, with the column height for a free-fixed configuration, or one-half of this product for a fixed-fixed configuration.

For seat-type abutment foundations, the superstructure is supported by bearings that can freely rotate, and the only means of transferring inertial shear from the superstructure is through a backwall, typically designed as a weak fuse with limited capacity to transfer load. For these reasons, it is assumed that no inertial loads are transferred from the superstructure for seat-type abutments. To account for the inertial effects of relatively massive foundation bodies, such as a pile cap, an inertial force is computed as

$$f_{\text{cap}} = 0.65 m_{\text{cap}} a_{\text{noliq}} \tag{2.2}$$

where a_{noliq} is the design peak ground acceleration (PGA) without consideration for liquefaction, m_{cap} is the pile cap mass, and the 0.65 factor is used to represent a reduction in PGA due to the onset of liquefaction. The combined kinematic-inertial pushover analysis is used to determine whether the foundation has sufficient capacity under an assumed peak demand case. This analysis is used to evaluate the resulting shear force and bending moment demands for the deep foundations and to assess whether the displacement at the pile cap/abutment is acceptable for the overall bridge structure.

2.1.2 Unrestrained Ground Displacement Case

The unrestrained design case applies to foundations that are assumed to be unable to significantly restrain the flow of soil associated with lateral spreading. An example case is an interior bridge bent foundation embedded in a site with broad transverse continuity, as shown in figure 2.1. In this case, the lateral stiffness of the foundation is insignificant relative to the loads applied by the lateral soil flow. For design purposes, it is assumed that soil movement will be unaffected by the presence of the foundation, though evidence from previous earthquakes (e.g., FHWA, 2011) has shown that this is not always true at the local level.

The design process for the unrestrained ground displacement case begins in the same manner as the restrained ground displacement case, with the assessment of liquefaction potential (step 1), estimation of residual strength for liquefied soils (step 2), and the definition of a foundation model (step 3) corresponding exactly. After the completion of these steps, the remaining steps for the unrestrained case differ from those previously discussed.

Estimation of the design ground displacement for the unrestrained case is initiated by evaluating the slope stability factor of safety (FS), assuming the absence of the foundation. If the $FS \leq 1.05$, a flow-type failure is assumed. Typically, an assumption of 5 ft of displacement is made, as this is considered sufficient to mobilize the full passive force of the crust on the foundation, and it is stated in Ashford et al. (2011) that as long as the passive force is mobilized, the remaining analysis is insensitive to the specific displacement value. For cases where $FS > 1.05$, the crustal displacement is estimated by using one of two simplified techniques. When the slope has a predictable failure surface, a Newmark sliding block-based approach (e.g., Bray and Travasarou, 2007) is used with an input acceleration set equal to the design PGA. For gentle

slopes, where there is greater uncertainty in the failure surface, crustal displacements are estimated by using the strain potential procedure of Faris et al. (2006).

The foundation is evaluated by using a lateral spreading pushover analysis, with an applied displacement profile as shown in figure 2.4. The imposed surface displacement in this analysis is set equal to that required to mobilize the full passive soil resistance for the $FS \leq 1.05$ case, or to the estimated crustal displacement for the $FS > 1.05$ case. Inertial loads from the bridge superstructure (if any) are included in this analysis in the manner described in step 7 for the restrained ground deformation case. The bending moment, shear force, and displacement demands computed with the pushover analysis are compared to the allowable foundation performance criteria.

Chapter 3 Generic Site Layout and Geometric Combinations for Parameter Studies

The parameter studies carried out using 3D finite element analysis (FEA) and the simplified equivalent static analysis (ESA) procedure considered generic sites and soil profiles with systematic variations in several geometric aspects. Figure 3.1 shows the general soil profile layout assumed in the generation of the cases considered. As shown, this generic layout consisted of an approach embankment sitting atop a soil profile consisting of a layer of loose liquefiable sand and a layer of denser sand that is less susceptible to liquefaction. The groundwater table was assumed to be located within the looser sand layer, effectively dividing this layer into two zones: a zone of non-liquefiable crustal soil located above the water table and a layer of liquefiable soil below the water table. The geometric variations made to this generic profile consisted of changes in the thickness of the non-liquefiable crust, the thickness of the liquefiable soil, and the crest width of the embankment. In all cases, the height of the embankment was taken as 5 m, and the total thickness of the underlying soil layers was set as 20 m. The soil constitutive parameters used in these studies are discussed in the following section.

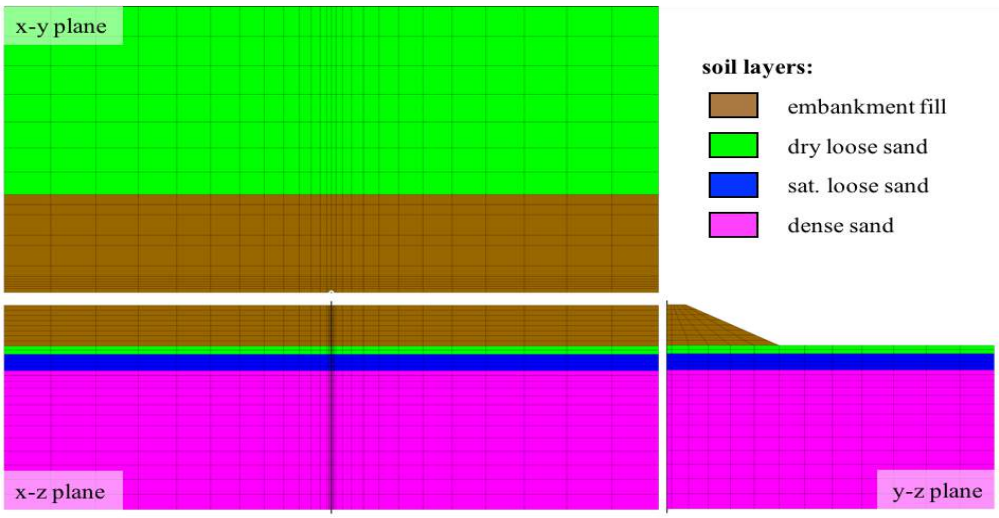

Figure 3.1 Generic site layout for cases considered in 3D FEA and simplified ESA parameter studies.

For all of the cases, a single deep foundation (i.e., pile or shaft) was assumed to be embedded through the soil profile up to a depth of 20 m below the original ground surface. Though the superstructure is not explicitly considered in any of the models, the head of the foundation was assumed to be fixed against rotations in the plane of bending to simulate the effect of a pile cap or other superstructure element. Two deep foundation diameter/stiffness cases were considered in the parameter studies to provide two soil-pile stiffness ratio cases, as previous work with these types of models has identified that the ratio of the soil and pile stiffness is of primary importance, rather than the actual stiffness values for each (McGann et al., 2012). The characteristics of the foundations are described in greater detail in a subsequent section.

3.1 Soil Properties

Generic soil properties were assumed for the various soil layers in the model and are listed in table 3.1. Four layers were defined: the embankment fill, a dry crustal sand layer, a liquefiable saturated loose sand layer, and an underlying denser sand layer. The constitutive models of Elgamal et al. (2003) were used to model the material response of all considered soils in the 3D FEA. The embankment fill, crust, and dense sand layers were modeled with Drucker-Prager type failure surfaces with friction angle dependent strengths, while the liquefied loose sand layer was modeled as a pressure independent material with a residual undrained shear strength defining the bounds of the failure surface. For the simplified ESA, the method of Brinch Hansen (1961) was used to compute the *p-y* spring parameters from the density and friction angles listed in table 3.1.

Table 3.1 Model properties for soil layers in parameter studies.

Layer	ρ (Mg/m^3)	φ ($^\circ$)	G_{max} (MPa)	K_{max} (MPa)	S_u (kPa)
dry loose sand	1.7	32	75	200	–
sat. loose sand	1.7	–	6.0	175	5.0
dense sand	2.0	38	100	300	–
embankment fill	1.9	38	130	390	–

3.2 Shaft Foundation Models

Two template pile/shaft models were considered, a 0.6-m-diameter pile and a 1.4-m-diameter shaft. These foundation models were based on actual deep foundation designs, and they considered linear elastic bending stiffness values determined from the initial tangent of the nonlinear moment curvature responses of the template cross-sections. The material and section properties used to define the shaft models are provided in table 3.2. The cross-sectional area, *A*, and second moment of the area, *I*, reported in this table were based on half of the shaft cross-section for consistency with the symmetry conditions assumed in the 3D FE models. The full values are used in the simplified equivalent static analyses, as no corresponding symmetry was applicable. The shaft elastic modulus values were chosen such that the linear elastic bending stiffness, *EI*, corresponded to the initial bending stiffness of the template cross-sections, and the elastic shear modulus, *G*, for each shaft was based on an assumed Poisson's ratio of 0.25. Further details on the template cross-section designs used to define these shaft models are discussed in McGann et al. (2012).

Table 3.2 Model material and section properties in parameter study shaft foundations.

Shaft diameter	A (m^2)	E (GPa)	G (GPa)	I (m^4)
0.6 m	0.15	31.3	12.5	0.0038
1.4 m	0.74	28.7	11.5	0.0869

3.3 Considered Site Geometries

The generic site layout and properties discussed in the preceding sections were used to examine the effects of different site geometries on the foundation demands developed during lateral spreading through the consideration of a large number of different geometric combinations. The geometric aspects varied to create the matrix of considered cases were the embankment crest width w, the thickness of the crust layer z (dry loose sand layer in figure 3.1), the thickness of the liquefiable layer t (saturated loose sand layer in figure 3.1), and the diameter/stiffness of the deep foundation. The current study was an expansion of the study performed by McGann and Arduino (2015), in which 72 distinct geometric combinations were considerd in 3D FEA: three crustal thicknesses (z =1.0, 3.0, 6.0 m), three liquefiable layer thicknesses (t =1.0, 3.0, 6.0 m), four embankment crest widths (w =4.0, 8.0, 16.0 m and full model width), and two pile/shaft diameters (0.6 and 1.4 m).

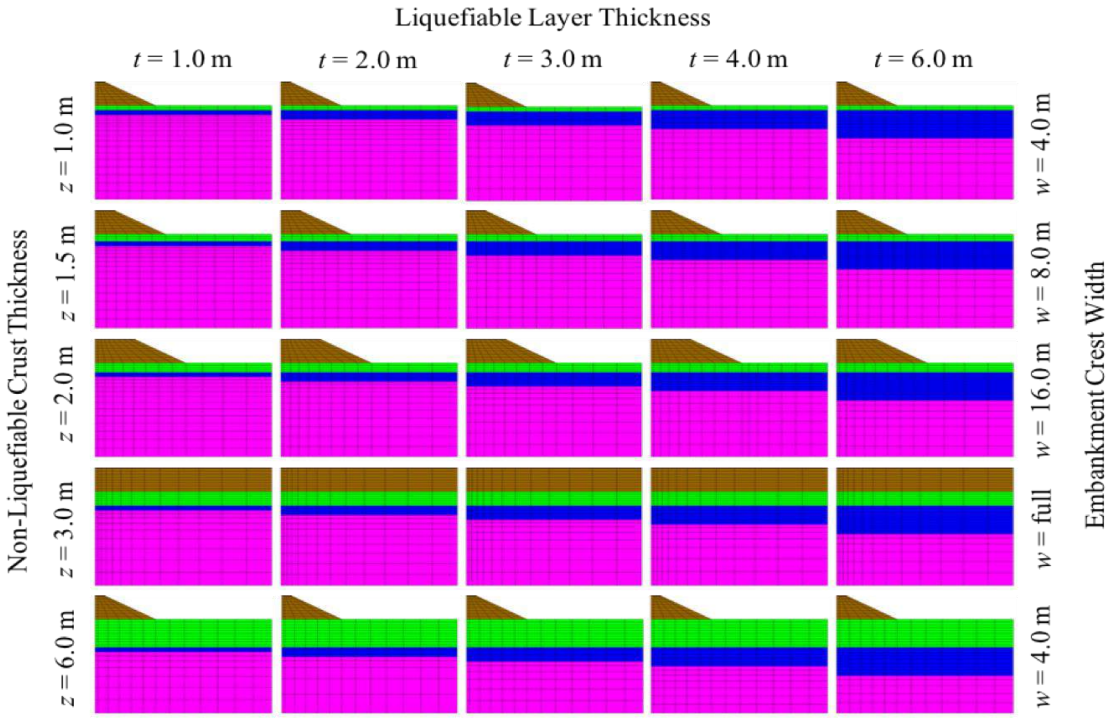

Figure 3.2 Summary of considered geometric configurations, including five liquefiable layer thicknesses (blue layer), five non-liquefiable crust thicknesses (green layer), and four embankment crest widths (brown layer).

McGann and Arduino (2015) identified several shortcomings in the case matrix for the original parameter study, in particular with regard to the lack of more realistic crustal and liquefiable layer thickness. To expand upon this previous effort, two new crustal thicknesses (z =1.5 and 2 m) and two new liquefiable layer thicknesses (t =2 and 4 m) were added to the case matrix, resulting in 128 distinct new cases. When combined with the 72 cases and results of McGann and Arduino (2015), this provided a total of 200 distinct geometric combinations. Figure 3.2 shows a summary of the soil profiles and embankment geometries considered in the overall case matrix. This plot does not show all of the considered combinations but is intended to portray the different parameter variations in relative terms. Of particular note are the embankment widths. Three of the embankment cases were representative of varying sizes of

finite-width embankments for which some degree of foundation pinning was expected. These embankments were distinguished by the crest widths and were defined with 2H:1V side slopes. The fourth embankment case considered an embankment that extends across the entire model domain and for which significant foundation pinning effects were not expected. Evaluation of the degree of pinning in each of the other three cases was made relative to the results of the full width case for the same combination of pile/shaft diameter, crust thickness, and liquefiable layer thickness.

Chapter 4 Development and Analysis of Three-Dimensional Finite Element Models

The 3D finite element models used in this study were intended to be the most simple representations of the problem that captured all of the relevant three-dimensional effects. Each model considered a single deep foundation embedded in a layered soil profile with an embankment sitting atop the upper soil layer. A schematic representation of the general layout used for these models is shown in figure 3.1, and a depiction of an example FE mesh used in the 3D study is shown in figure 4.1. As shown, and as discussed in the previous chapter, the generic site profile consists of three soil layers with an embankment placed on top of the uppermost native soil layer. For the purposes of the 3D models, the embankments were 5 m high in all cases, extended across the full length of the mesh in the direction of the longitudinal axis of a hypothetical bridge, and were defined with a 2H:1V side slope in the transverse direction, out away from the longitudinal bridge axis. The direction of loading for these models coincided with the longitudinal bridge axis, and no skew effects were considered in the current study.

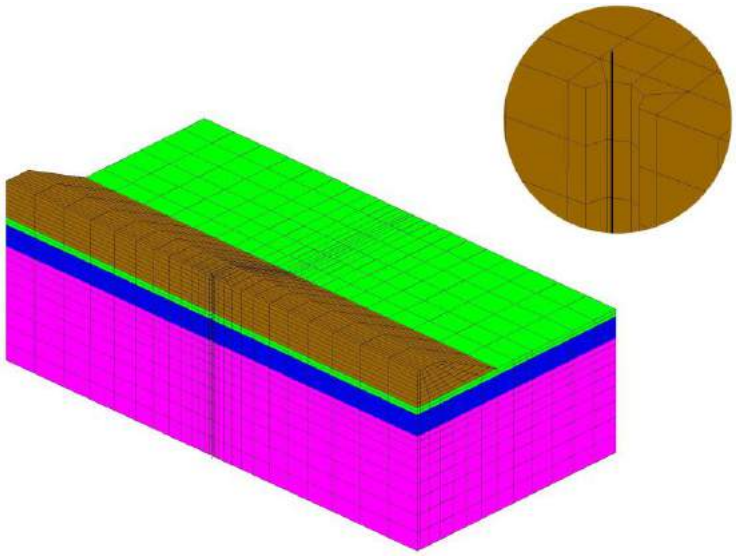

Figure 4.1 Example 3D finite element mesh used in the parameter study. Inset at top right shows close-up of the area around the shaft foundation in the model.

4.1 3D Finite Element Model Development

The following sections describe the development of the 3D finite element models used in this study. All of the models were developed and analyzed with the OpenSees computational framework (McKenna, 1997; McKenna et al., 2010). The commercial pre- and post-processing software GiD (CIMNE, 2008) was used to create the mesh for each case and to visualize some of the results shown in subsequent sections and chapters. Solid elements were used to model the soil, beam-column elements were used to represent the deep foundation body, and the beam-solid contact element of Petek (2006) was used to represent the soil-foundation interface. The mesh for each model was generated to minimize boundary effects on the important portion of the model (soil-pile interface), and symmetry and selective mesh refinement were used, as shown in figure 4.1.

4.1.1 Boundary and Loading Conditions

Boundary conditions were applied only on the outer surfaces of the soil mesh, with the nodes on each surface fixed against out-of-plane translations only. Symmetry was considered as shown in figure 4.1, with the symmetry plane cutting through the center of the shaft foundation such that only one half of the shaft was considered in the model. The nodes on the vertical boundary opposite the symmetry plane were fixed against all horizontal translation, and the nodes on the remaining non-symmetry vertical boundaries were fixed against out-of-plane translations only. The soil mesh boundaries were placed 35 m away from the shaft centerline in both horizontal directions, and the mesh was 20 m deep vertically, with a 5-m-tall embankment for all configurations. The 35-m distance was chosen on the basis of sensitivity studies, seeking to minimize the effects of the boundaries on the shaft and near-field soil elements. Elemental

body forces equal to the unit weights of each soil layer were applied to the solid elements to achieve a proper initial state of stress in the soil.

The shaft foundation was modeled with displacement-based beam-column elements that interfaced with the surrounding solid elements via the beam-solid contact elements of Petek (2006). A detail of the mesh immediately surrounding the shaft centerline is provided in figure 4.1. As shown, a semi-circular space was built into the solid element mesh to consider the physical size of the shafts considered in the study. The base node of the shaft was fixed against vertical translations, and the upper node was fixed against all rotations to simulate the rotational restraint provided by a pile cap or abutment. The assumption of complete rotational fixity was a simplified view of the actual rotational behavior at this point; however, the true behavior was closer to fixed than to free, so it was deemed sufficient for the purposes of this study. All of the nodes in the beam-column elements of the shaft body were fixed against translations normal to the symmetry plane, and they were only allowed rotations within the symmetry plane (i.e., out-of-plane and torsional rotations were fixed). No distinction was given to whether the deep foundation was a driven pile or drilled shaft beyond the foundation size; i.e., no installation effects were considered in the model set-up or analysis. A vertical force of 4000 kN was applied to the uppermost pile node during the gravity analysis phase for the models, and this force was held constant during the analysis to represent a loading from the superstructure.

The kinematic demands of lateral spreading were simulated in the models by incrementally imposing displacements to the non-symmetry vertical mesh boundaries. The applied displacement profile was roughly representative of the free-field lateral spreading deformation profile (in a very simplified sense), with constant displacements across the crust

layer, zero displacements in the lower non-liquefiable material, and a linearly increasing profile across the liquefiable layer. This simplified profile mirrored that recommended by Ashford et al. (2011) for use in the simplified ESA approach in the absence of better estimates based on something like shear strain profiles. The final free-field surface displacement for all of the models was 1.0 m. This approach is not able to capture effects related to pore pressure, inertia, or the initiation of liquefaction, but it is an effective way of imposing the kinematic demands of lateral spreading on the embedded foundation. Additionally, this approach enforced comparison-facilitating consistency across all of the analyses that would have been difficult to achieve with dynamic effective stress analyses. Further details on the loading conditions are available in McGann and Arduino (2014, 2015).

4.1.2 Elements and Constitutive Models

The nested yield surface constitutive models of Elgamal et al. (2003) were used to model the material response of the soils in the 3D FEA in alignment with the model properties summarized in table 3.1. The embankment, crust, and dense sand layers were modeled by using a Drucker-Prager type failure surface with overburden pressure-dependent strength, while the liquefied loose sand layer was modeled as a pressure independent material with a stiffness and undrained shear strength representing the residual strength of the liquefied material. This constitutive approach for the liquefiable layer was in accordance with the previously discussed overall modeling approach in which the liquefiable layer is assumed to be fully liquefied at the onset of the analysis. The displacement-only, hourglass stabilized, single-point integration, hexahedral elements of McGann et al. (2015) were used for the soil domain in a total stress analysis approach.

The shafts in the 3D FE models were considered to be linear elastic such that the demands could be assessed independently of strength. Displacement-based beam column elements were used to represent the shafts, and these elements were assigned a linear elastic section response with the section and material properties shown in table 3.2 for the selected 0.6- and 1.4-m-diameter shaft designs. The beam-solid contact elements of Petek (2006) were used to link the beam-column elements to the surrounding solid brick elements. This contact element created a frictional stick-slip interface between the beam and solid elements that considered the physical size of the shaft body and captured the full kinematics of the shaft deformation. The use of this element necessitated the semi-circular void built into the area surrounding the beam elements shown in the inset of figure 4.1, which is sized on the basis of the diameter of the shaft.

4.2 Summary of Overall 3D FEA Parameter Study Results

The effects of approach embankment and soil profile geometry on the flexural response of the shaft foundations in the 3D models were initially assessed through comparisons of the results obtained from the various cases considered in the parameter study. These comparisons were made both qualitatively and quantitatively, and the discussion of the observed effects is organized into several sections in order to isolate the individual effects of each considered geometric aspect. In general, the results of the 3D FE parameter study demonstrated that the presence of the shaft foundation alters the soil deformation field such that only the material near the boundaries experiences the full free-field displacement applied to the model. This resistance varies depending on the geometric configuration of the site, as certain combinations lead to greater and more widespread resistance, while others indicate a less significant effect.

To demonstrate the range of responses obtained from the models, and to provide an overall sense of the model results and performance, figures 4.2 and 4.3 show the deformed mesh

with contours of displacement in the loading direction (to the right in the figures) for section and plan views of the meshes of two models. The only difference between the two models shown is the embankment width. Figure 4.2 shows a case with an 8-m-wide embankment crest (w =8 m), and figure 4.3 consider a case in which the embankment extends over the full width of the mesh. The soil profiles for both cases shown considered a 0.6-m-diameter shaft with a 3-m-thick liquefied layer located 1 m below the base of the embankment fill (i.e., D =0.6 m, t =3 m, and z =1, using the terminology defined in the previous chapter).

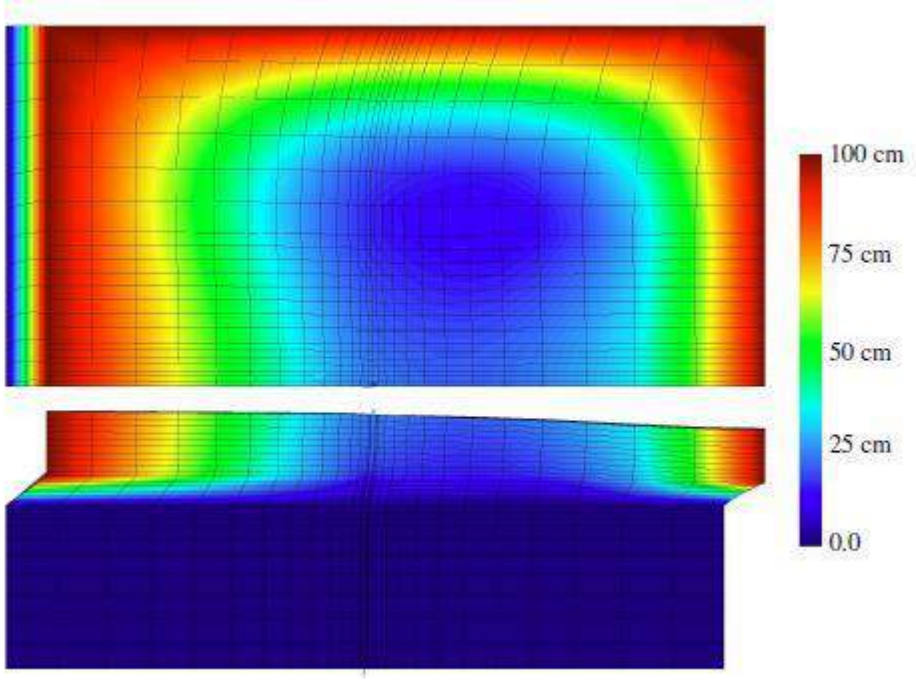

Figure 4.2 Deformed mesh (magnified 4 times) with contours of horizontal deformation for w = 8 m case with D =0.6 m, z =1 m, and t =3 m.

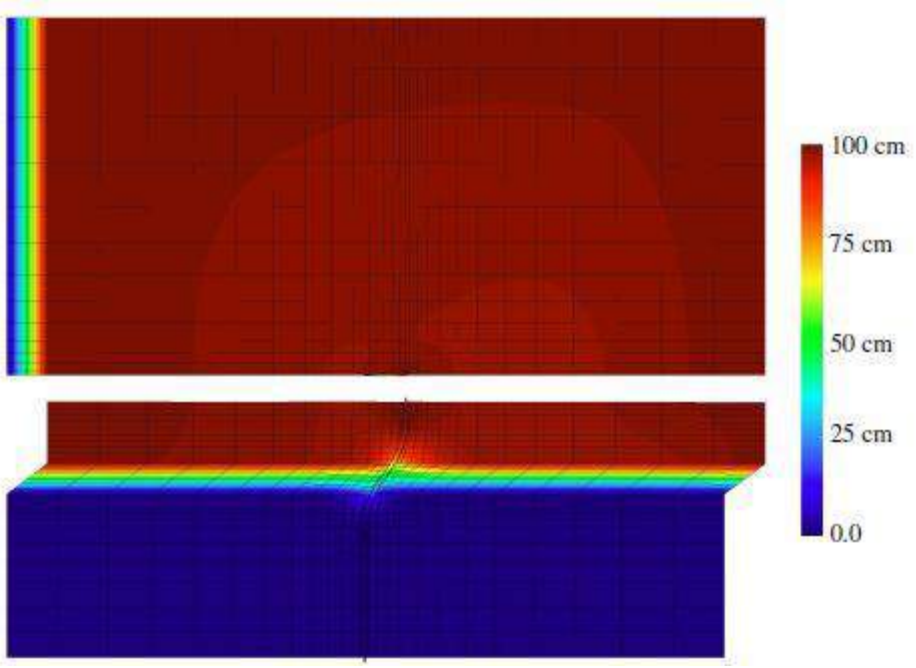

Figure 4.3 Deformed mesh (magnified 4 times) with contours of horizontal deformation for full width case with D =0.6 m, z =1 m, and t =3 m.

As shown in figures 4.2 and 4.3, the applied displacement profile was applied to the free-field boundaries of the soil mesh using the previously described simplified displacement profile. Because of these imposed free-field demands, the shaft was loaded laterally and offers resistance to this loading evidenced by the altered near-field soil deformations. The level of resistance observed in the models depended on the shaft stiffness/diameter and the particular geometric combination under consideration (i.e., the embankment width, crust thickness, and liquefiable layer thickness). For the case shown in figure 4.2, which considered an 8-m-wide embankment, the shaft provided substantial resistance to the lateral deformation of the soil, as the deformations near the shaft were approximately one-quarter of the free-field displacement, and this effect was manifested over a large portion of the soil domain that extended well beyond the immediate near-field soil surrounding the shaft. In contrast, in the results shown in figure 4.3, which shows the same results for the full width embankment, the shaft offered only minimal lateral resistance, as

nearly the entire soil domain experienced the free-field deformation profile. This general trend of increased embankment width leading to a more homogeneous soil deformation field and less apparent pinning resistance from the foundation was observed throughout all of the 3D models considered and is discussed in greater detail in the following section.

4.2.1 Effects of Embankment Crest Width

The general effects of increasing embankment width are demonstrated through a comparison of figures 4.2 and 4.3; however, it is also of interest to assess the differences in how the four considered embankment crest widths affected the embedded shaft foundations. The effects of the different embankment sizes on the foundation demands are shown in figures 4.4 and 4.5, which show the shaft bending demand profiles (displacement, shear force, and bending moment) for the indicated parameter combinations for the 0.6-m and 1.4-m-diameter shaft models, respectively, after the full application of the 1-m free-field lateral spreading pushover. In these plots, w1 through w4 correspond to the four embankment crest widths ordered from low to high (4, 8, 16, and 35 m). The thickness of the liquefiable material (t =1, 2, 3, 4, and 6 m) and the non-liquefiable crust (z =1, 1.5, 2, 3, and 6 m) are noted for each row and column in figures 4.4 and 4.5. For reference, the extents of the embankment fill and liquefiable zone are indicated by the tan and gray shaded zones, respectively, present in each plot. For visual comparisons made using these results, note that the axis limits for the shear force and bending moment profiles vary for each shaft diameter (i.e., across figures 4.4 and 4.5) and for some of the liquefiable layer thicknesses (i.e., columns of plots within each figure).

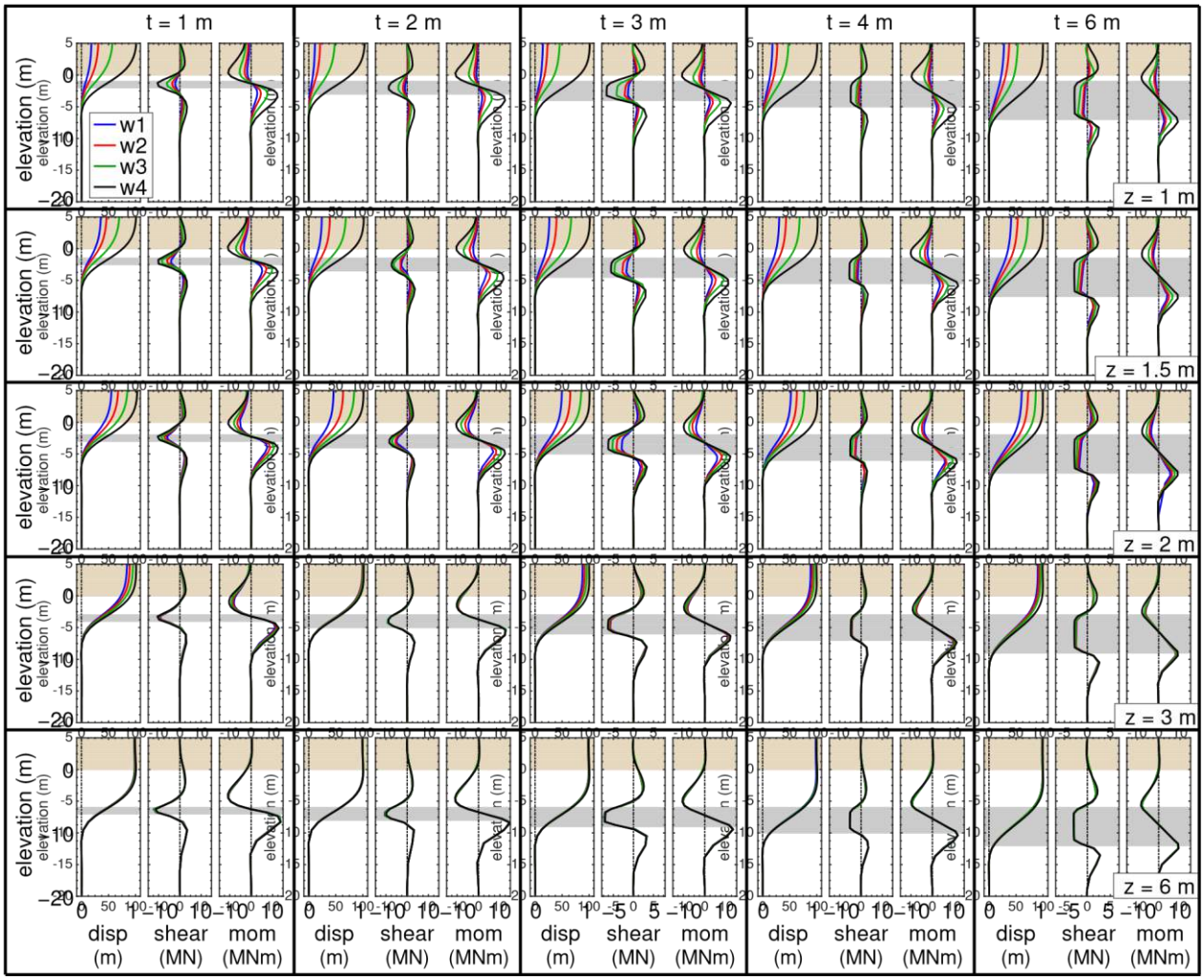

Figure 4.4 Shaft displacement, shear force, and bending moment demands for all 3D FE parameter study cases for 0.6-m-diameter shaft.

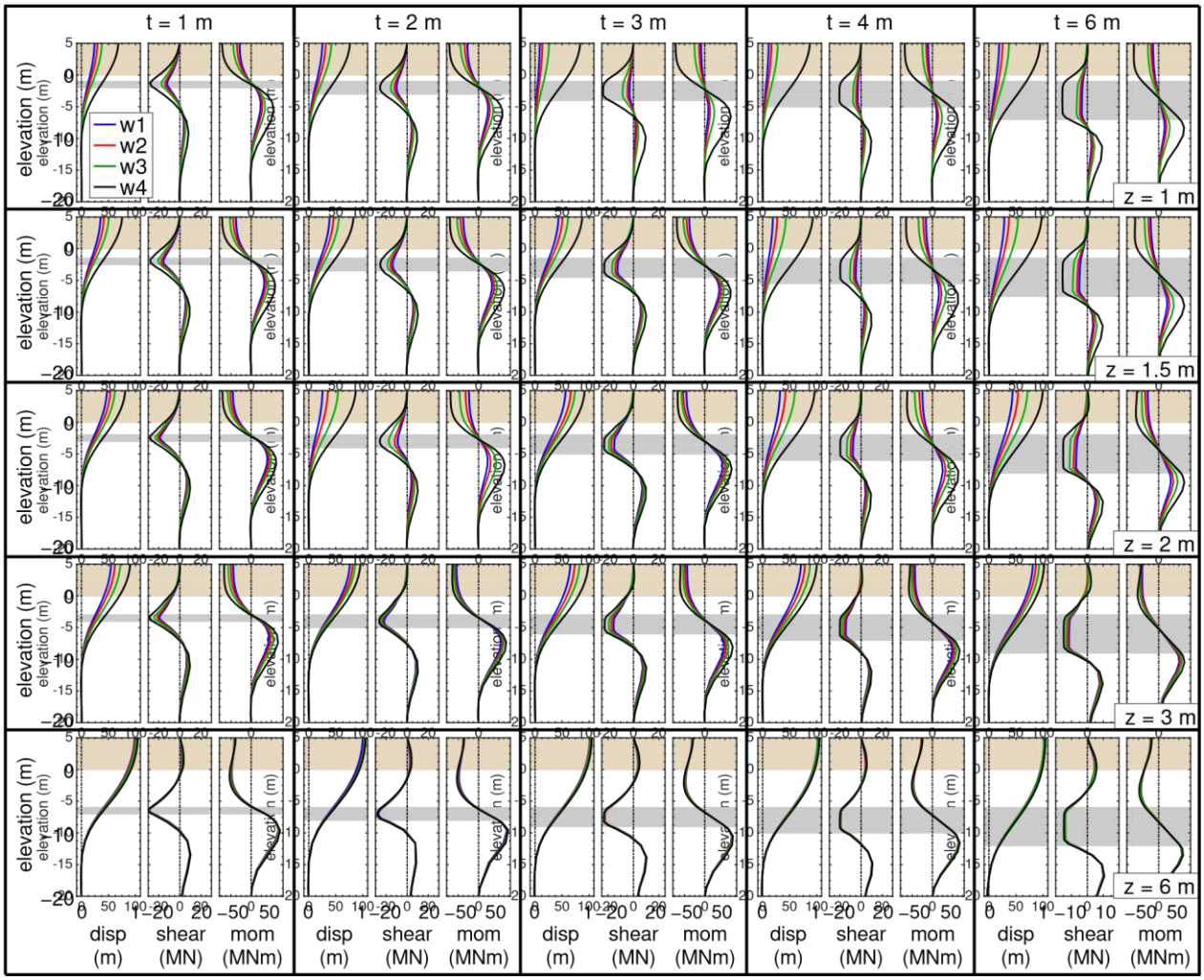

Figure 4.5 Shaft displacement, shear force, and bending moment demands for all 3D FE parameter study cases for 1.4-m-diameter shaft.

As expected on the basis of the soil deformation fields of figures 4.2 and 4.3, increased embankment width led to increased shaft bending demands, both in terms of the maximum displacement, shear force, and bending moment demands, as well as in terms of the overall profiles of these demands. This is most clearly seen for the shallow liquefiable layer cases in the first two or three rows of plots in figures 4.4 and 4.5, where the differences between the various embankment width cases are the largest, though it is evident to some degree in all of the results. It was observed that the general forms of the displacement, shear force, and bending moment

profiles remained similar for the four widths; however, the magnitudes became larger, and, in general, for constant D, z, and t, the locations of the shear and moment inflection points moved farther apart as the embankment became wider. It was also observed that the embankment width was not the only critical factor in the differences between the shaft demands for each case.

4.2.2 Effects of Non-Liquefied Crust Thickness

The thickness of the non-liquefied crust played an important role in defining how changes in embankment crest width affected the embedded foundation response during lateral spreading. For the cases with relatively thin crusts, the width of the embankment was very influential to the shaft response. This can be observed in the results of the first three rows of plots in figures 4.4 and 4.5, which show the results for cases with crustal thicknesses of z =1, 1.5, and 2 m. As shown in these plots, there were significant differences in the shaft bending demand profiles and in the maximum bending demands for the four considered embankment crest widths when the crust was relatively thin. As the crustal thickness (depth to the liquefied layer) was increased, the differences between the shaft bending demands resulting from the four widths became less significant. For example, with z =3 m, there was less variation in the shaft demands for increasing values of w than for the corresponding cases with z =1. With z =6 m, there was almost no difference in the demands manifested by the four crest widths.

These observations suggested that for these single shaft cases, there is a limiting liquefied layer depth at which the 3D embankment effects are no longer a significant factor in defining the structural demands in the foundation. When the liquefied layer is relatively shallow, the approach embankment is the primary source of kinematic demands on the shaft foundation during lateral spreading, and thus, differences in the geometry of the embankment are very influential on the foundation response. As the amount of crustal soil increases, a greater amount

of soil below the embankment is mobilized during the simulated lateral spreading event, and the kinematic demands placed on the foundation by the lateral movement of this crustal layer begins to control the overall shaft response. On the basis of the original 72 parameter study cases with t =1, 3, and 6 m and z =1, 3, and 6 m, McGann and Arduino (2015) noted that the apparent limiting crustal thickness was 3 m for the 0.6-m shaft and something more than 3 m for the 1.4-m shaft. The additional thinner crust thicknesses (z =1.5 and 2 m) considered in the expanded parameter study of the current work were added in part to examine whether the limiting crust thickness is something less than 3 m but greater than 1 m. On the basis of the results of figures 4.4 and 4.5, it appears that the observations of McGann and Arduino (2015) still hold, as there were still quite significant differences in the shaft bending demands for crustal thicknesses of 1.5 and 2 m.

4.2.3 Effects of Liquefied Layer Thickness

The effects of liquefied layer thickness were more subtle than those observed for the embankment crest width and liquefied layer depth. On the basis of the results shown in figures 4.4 and 4.5, a clear trend was not apparent for all cases demonstrated by changes in t; however, there were differences in how the foundation was affected for the considered liquefied layer thickness values. One effect of the liquefied layer thickness was manifested in the foundation shear force demands. As shown, for constant values of D, w, and z, thinner liquefied layers tended to lead to larger shear force demands. This was almost certainly due in part to how the applied displacement profile changed for thinner layers. As the thickness of the liquefied layer decreases, the shear demands on the shaft should approach the maximum possible value that would result in the absence of the linearly distributed portion of the applied displacement profile. In contrast, the bending moment demands were much less affected by changes in t, though the

distance between the maximum moment demands naturally increased with liquefied layer thickness.

The thickness of the liquefied layer also appeared to affect how the embankment width influenced the foundation response, and these effects showed a depth dependence. As shown in figures 4.4 and 4.5, the relative differences between the maximum bending demands for the four crest widths were not uniform for the five thicknesses considered. With t =1 and 2 m, there was less variation with width than for the 3-, 4-, and 6-m layer thicknesses, particularly for the shallower crustal thicknesses and the 1.4-m-diameter cases. For deeper liquefiable layer configurations, this effect was not as apparent, and there was more consistency in the relative demands for the four widths at each thickness value.

4.2.4 Effects of Shaft Bending Stiffness

Some of the differences observed for the two shaft designs were expected effects of the two bending stiffness values represented by the shafts. The smaller shaft had a lower bending stiffness in comparison to the soil stiffness ($EI_{0.6}$ =119 MN·m^2 in comparison to $EI_{1.4}$ =2494 MN·m^2); therefore, for corresponding soil profiles, the displacements of the 0.6-m shaft were larger and more closely resembled the applied displacement profile, while the larger shaft design offered more resistance to the lateral soil deformation. Because the larger shaft had a larger stiffness, for similar levels of shaft displacement, the shear and moment demands in the 1.4-m shaft were much larger than those in the 0.6-m shaft.

The crustal thickness effects discussed in the preceding sections appeared to change on the basis of the shaft bending stiffness. A comparison of figures 4.4 and 4.5 shows this effect; with z =3 m, there was more variation with width in the maximum bending demands for the 1.4-m shaft than for the 0.6-m shaft. This observation also holds for the z =6 m cases, as there was

essentially no variation with embankment width for the 0.6-m shaft cases, while the larger shaft still showed some visible differences for the considered crest widths. The implications of these observations make sense in the context of the problem, as it seems natural that the amount of crustal soil necessary to negate the three-dimensional effects of the embankment and soil on the foundation response would depend on the size and stiffness of the foundation itself.

4.3 Assessment of Maximum Bending Demands in 3D FEA

Figures 4.4 and 4.5 provide an essential overview of the shaft bending demands at the end of the applied lateral spreading pushover analysis for all of the 3D FE model parameter study cases; however, they provide no information on how the demands developed during the course of the analysis and only offer comparisons between the various embankment width cases in a relative visual sense. To supplement these results, the evolution of the maximum displacement, shear force, and bending moment demands in the shaft models for each case were computed and are plotted in figures 4.6 through 4.15. Each of these figures shows the maximum demands for all of the embankment width and crustal thickness cases corresponding to a single combination of shaft diameter D and liquefiable layer thickness t.

The results shown in figures 4.6 through 4.15 support many of the observations made in the discussion of the previous sections, while providing additional insights into how the maximum shaft bending demands changed with increasing free-field displacement. As shown, perhaps with the exception of the first few analysis steps, for all levels of free-field displacement, larger embankment widths led to larger maximum bending demands. The maximum displacement, shear, and moment demands were affected similarly by changes in w, and it appears that for constant values of D, z, and t, the relative difference between the results for each embankment width remained nearly constant over the course of the free-field displacement

application. In all cases, the bending demands obtained from the wide embankment geometry were greater than or equal to the bending demands for the 3D embankment geometries.

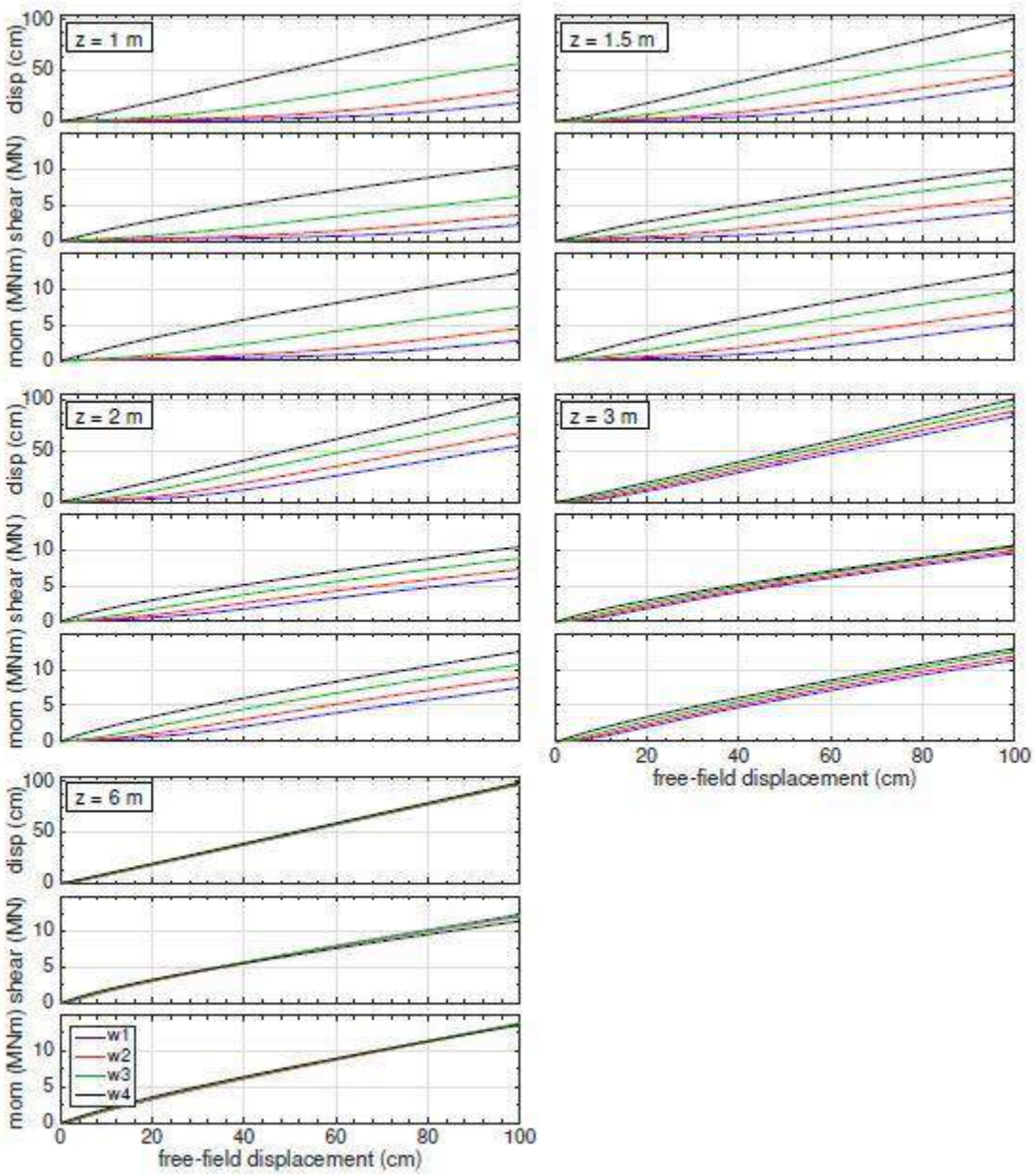

Figure 4.6. Maximum shaft bending demands with increasing free-field displacement for five crust thicknesses with D =0.6 m and t = 1 m.

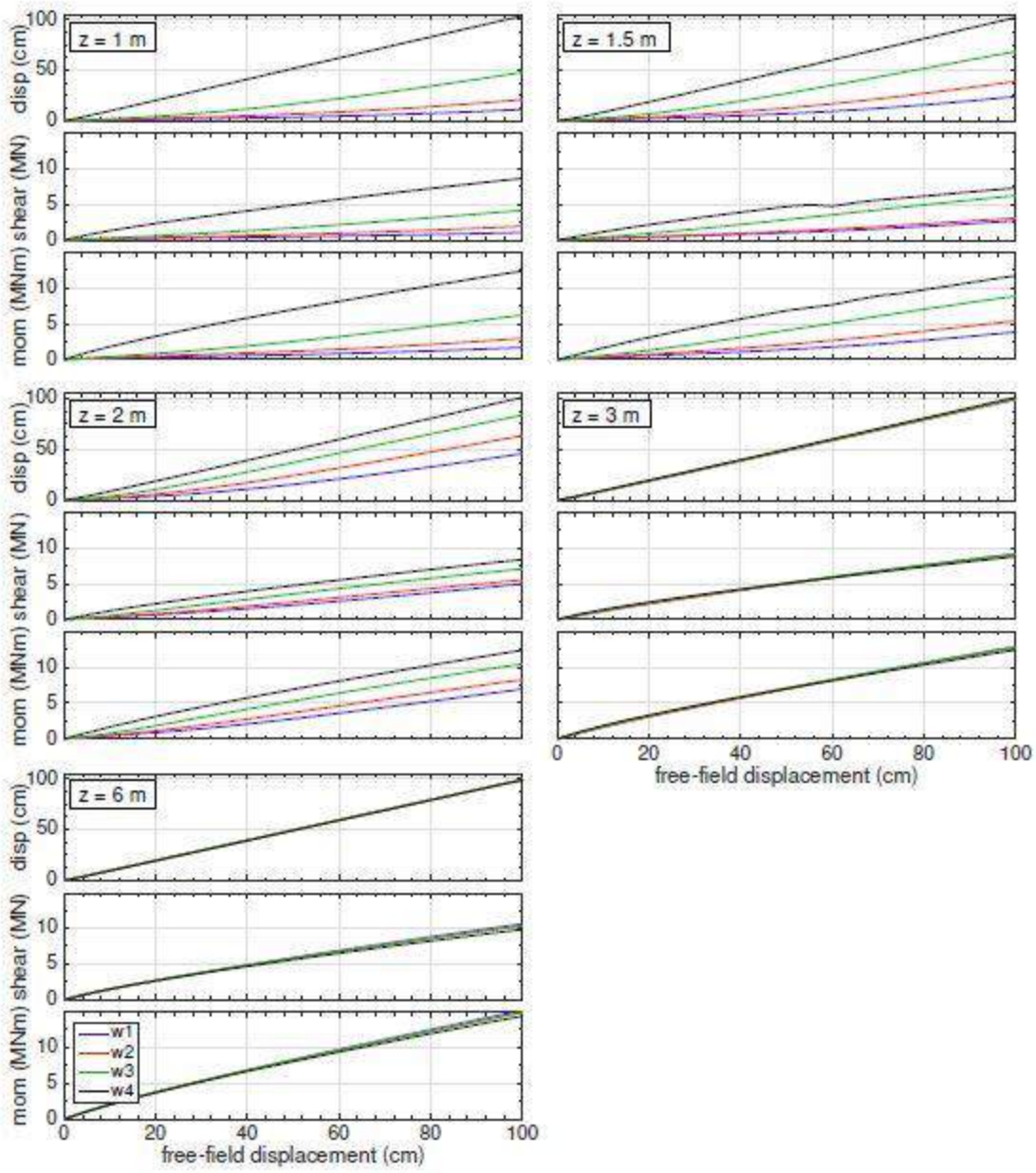

Figure 4.7 Maximum shaft bending demands with increasing free-field displacement for five crust thicknesses with D =0.6 m and t = 2m.

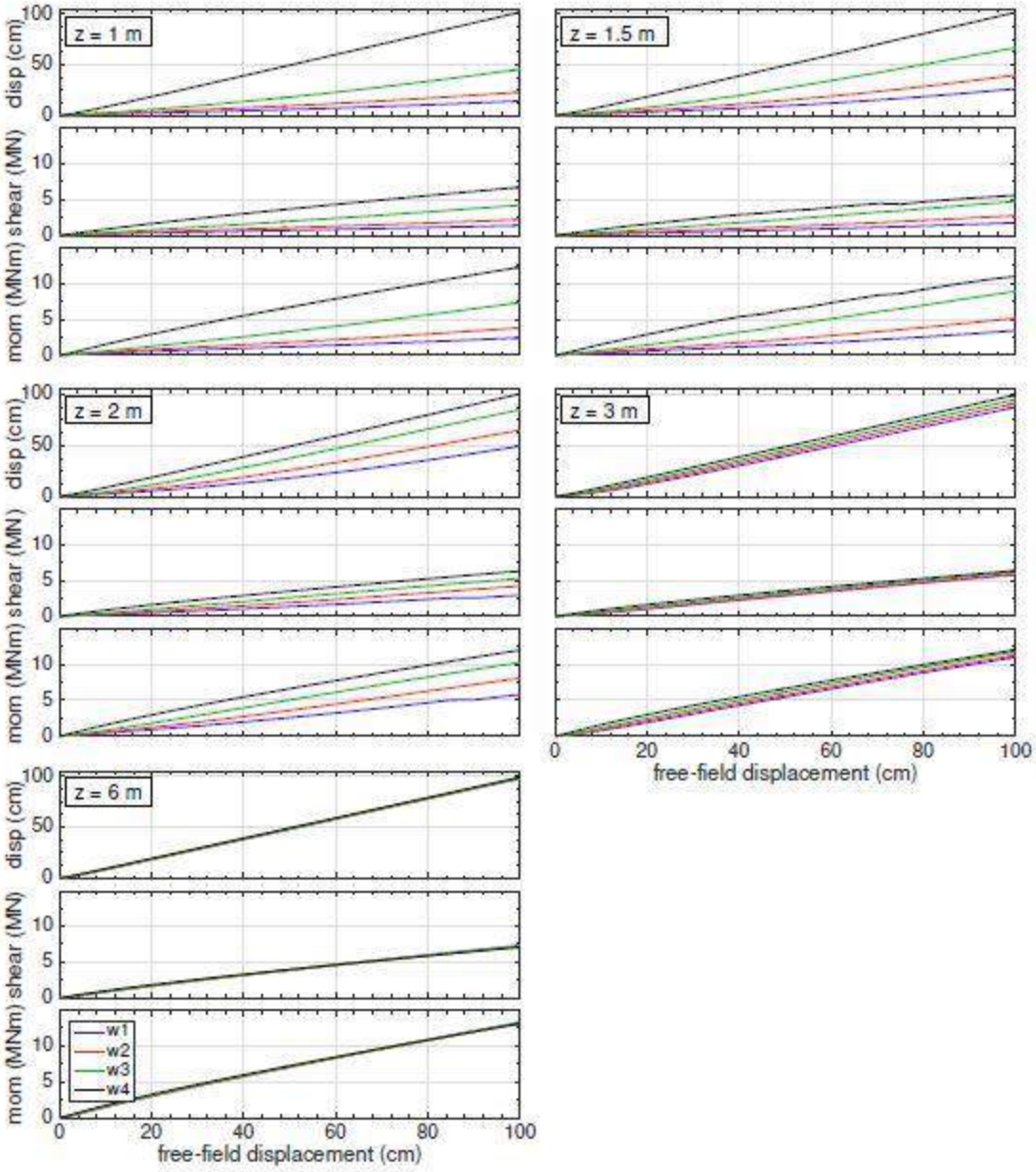

Figure 4.8 Maximum shaft bending demands with increasing free-field displacement for five crust thicknesses with D =0.6 m and t = 3 m.

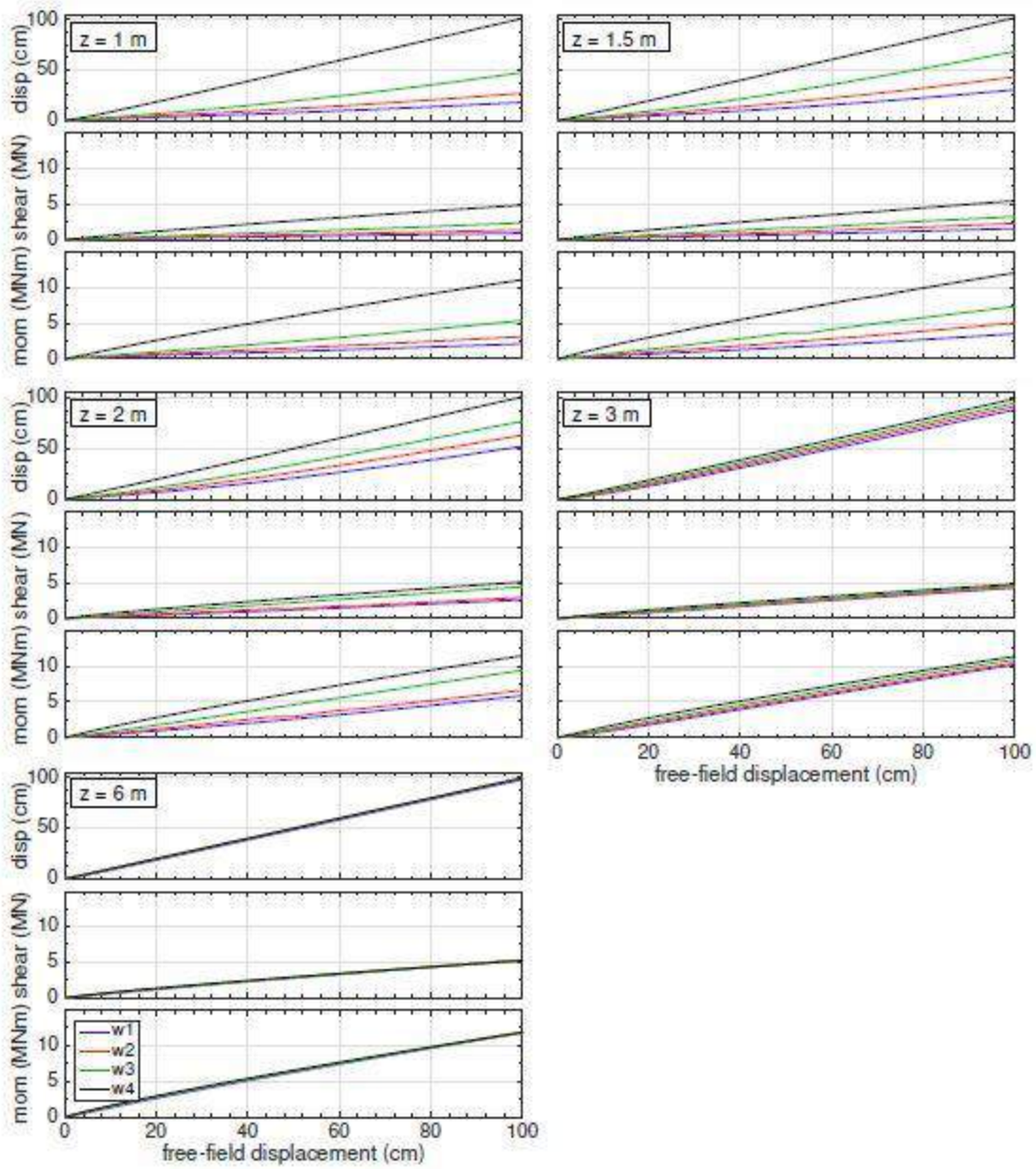

Figure 4.9 Maximum shaft bending demands with increasing free-field displacement for five crust thicknesses with D =0.6 m and t = 4 m.

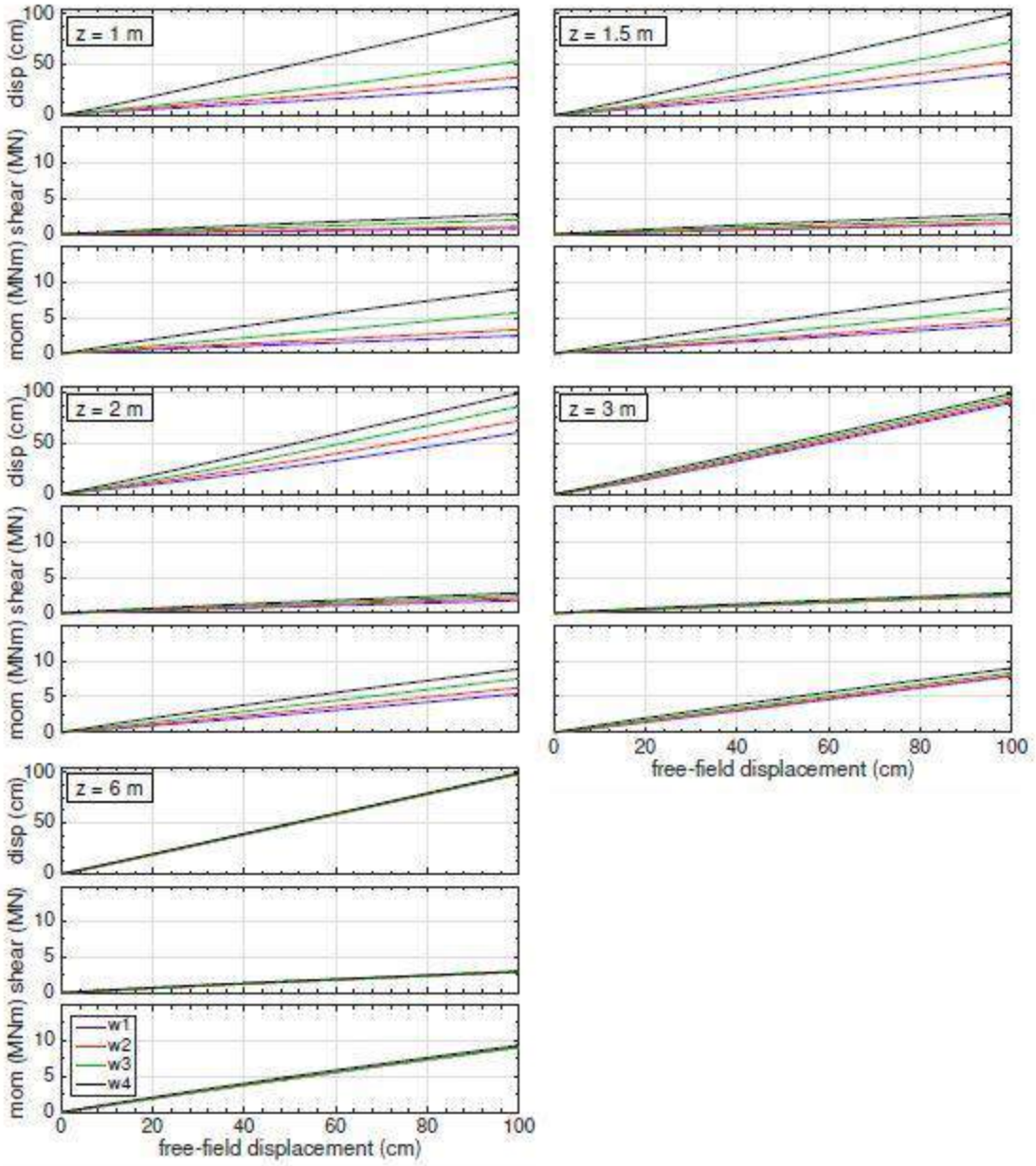

Figure 4.10 Maximum shaft bending demands with increasing free-field displacement for five crust thicknesses with D =0.6 m and t = 6 m.

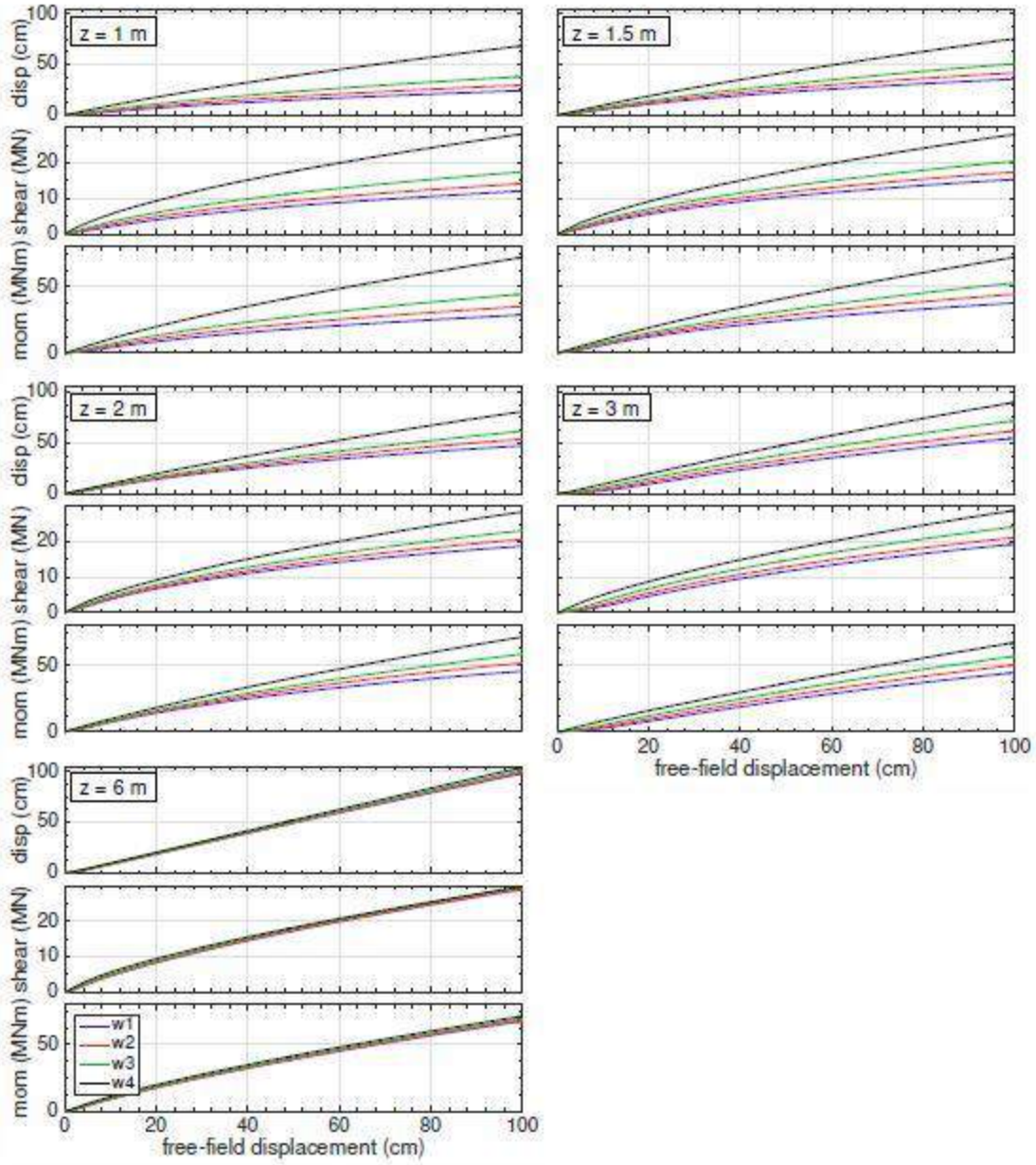

Figure 4.11 Maximum shaft bending demands with increasing free-field displacement for five crust thicknesses with D = 1.4 m and t = 1 m.

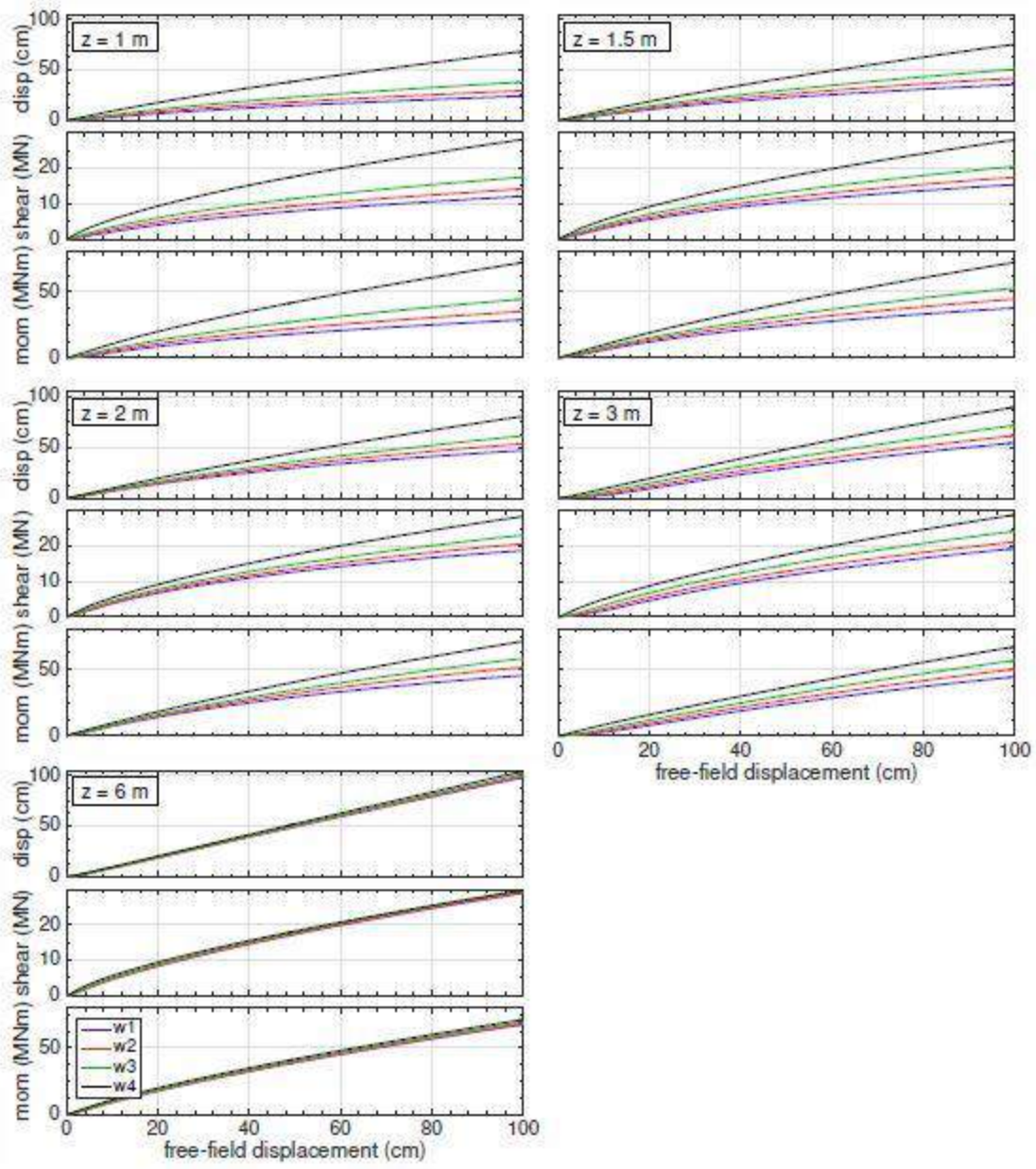

Figure 4.12 Maximum shaft bending demands with increasing free-field displacement for five crust thicknesses with D = 1.4 m and t = 2 m

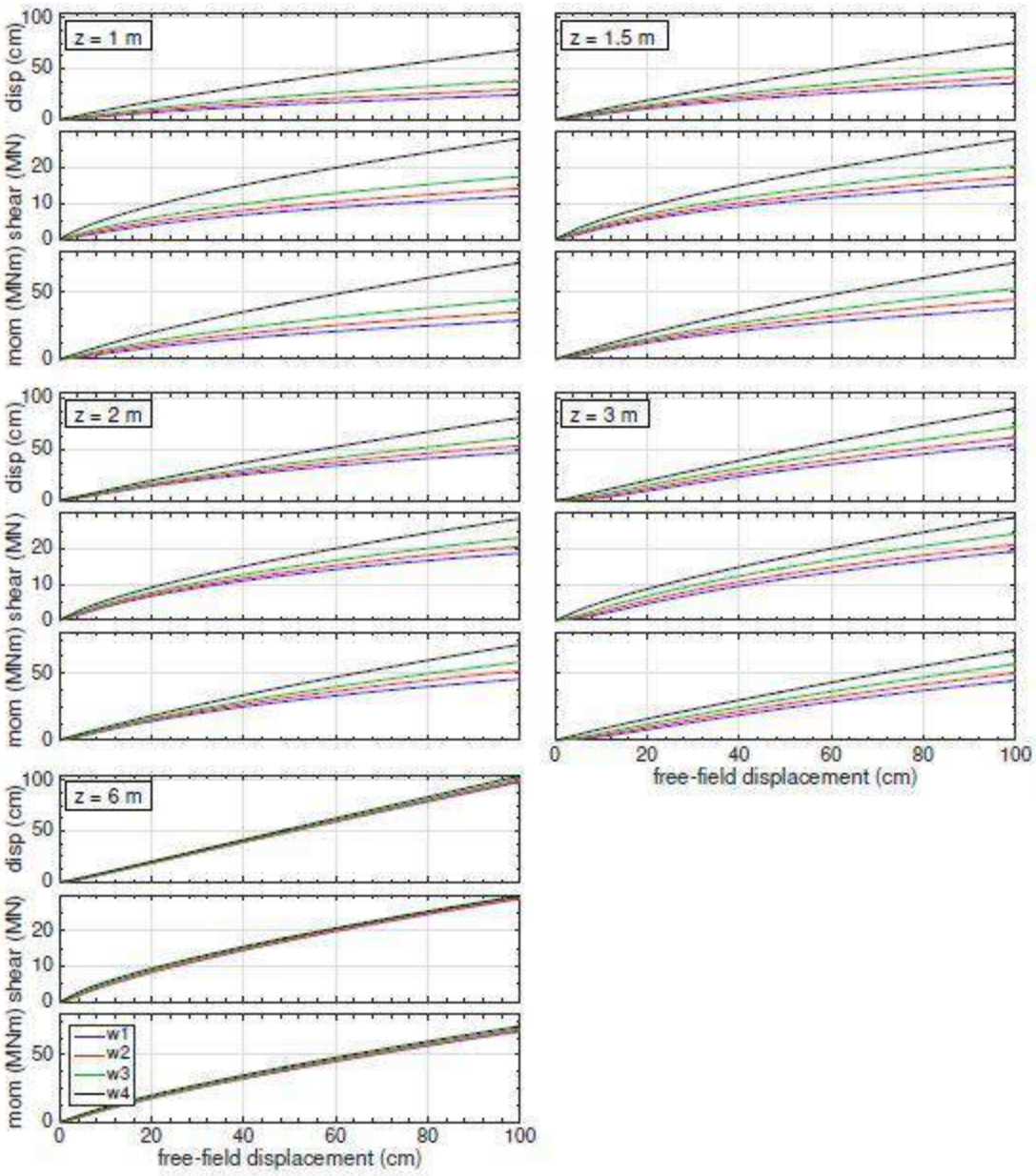

Figure 4.13 Maximum shaft bending demands with increasing free-field displacement for five crust thicknesses with D = 1.4 m and t = 3 m

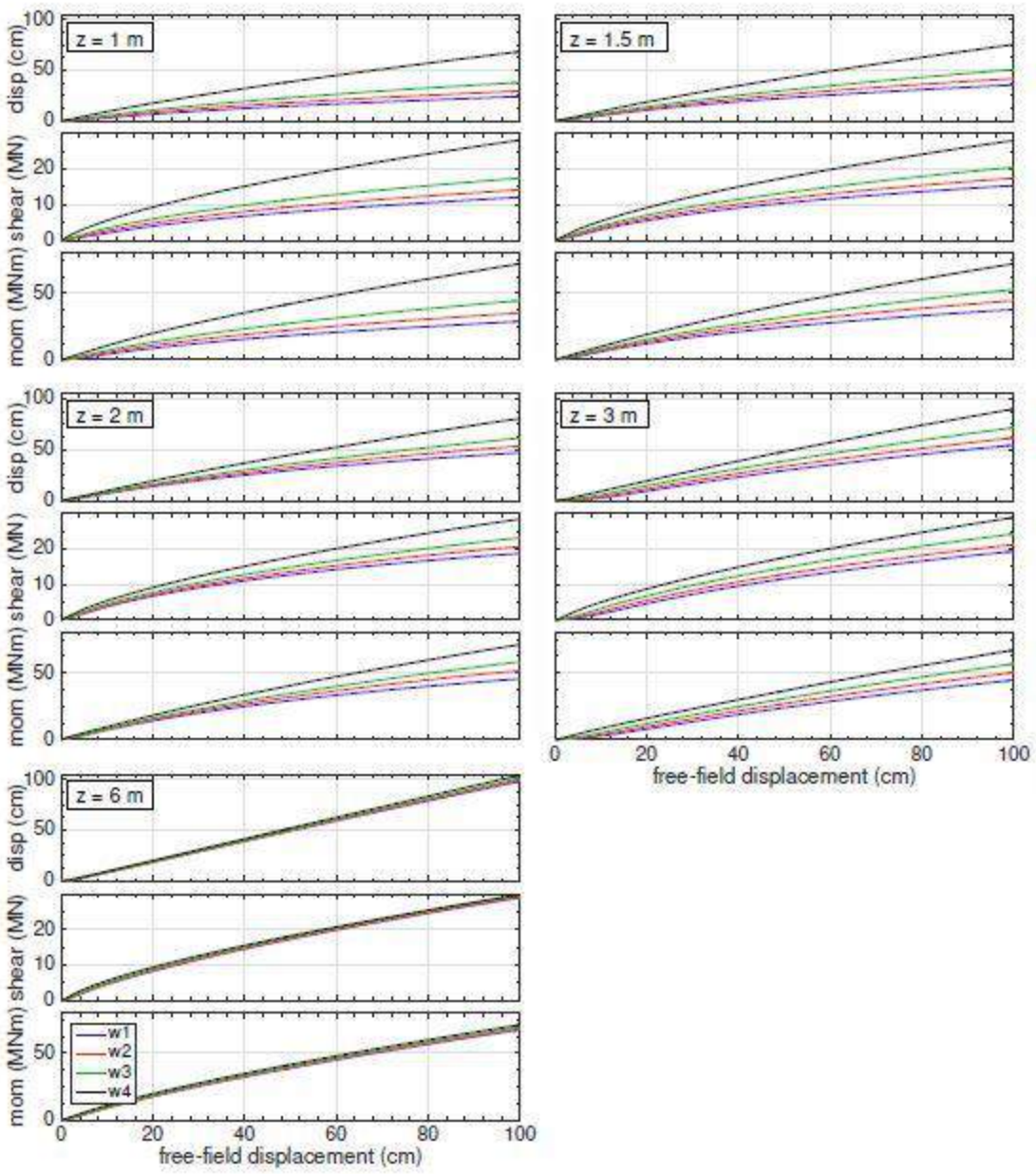

Figure 4.14 Maximum shaft bending demands with increasing free-field displacement for five crust thicknesses with D = 1.4 m and t = 4 m

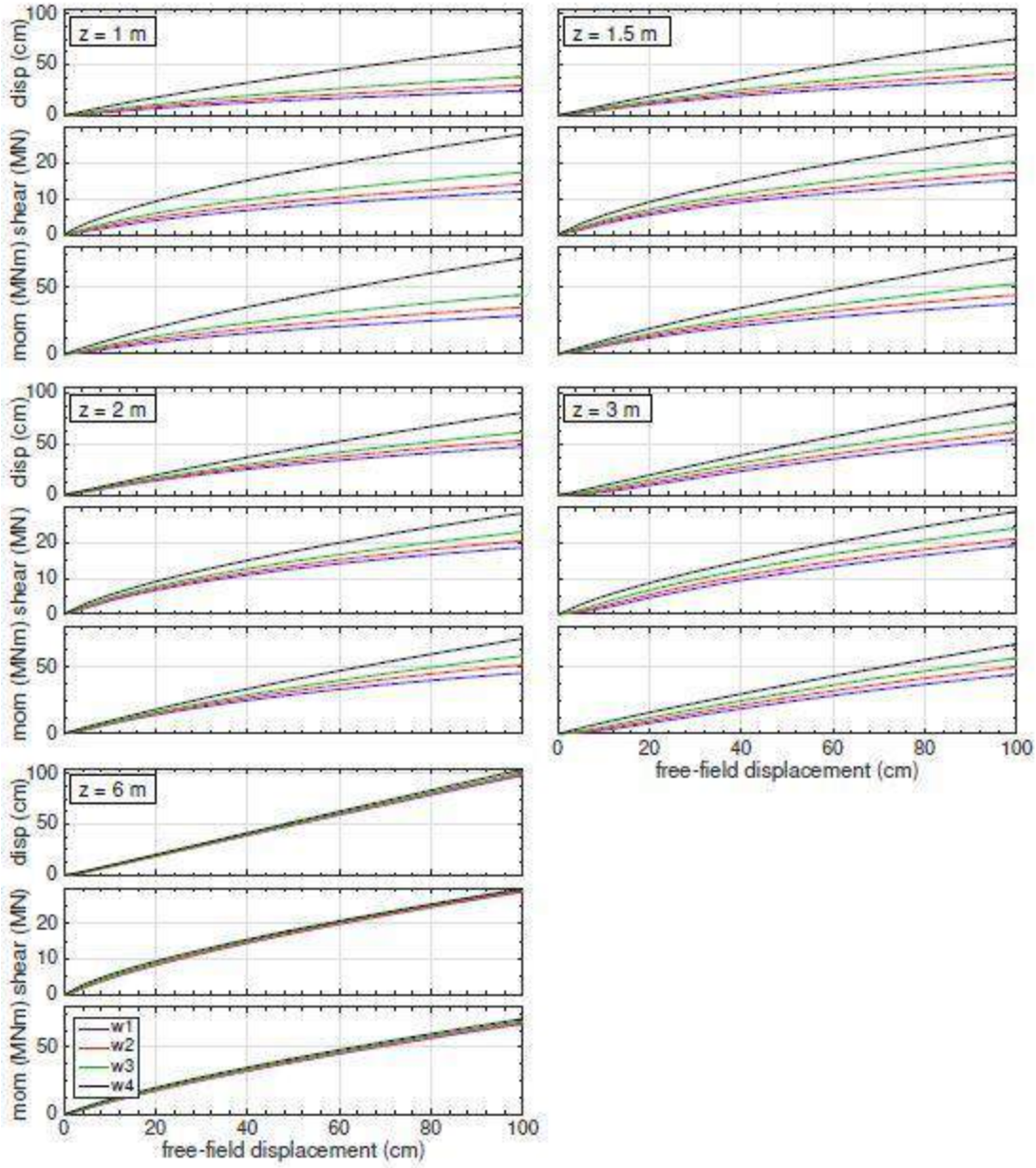

Figure 4.15 Maximum shaft bending demands with increasing free-field displacement for five crust thicknesses with D = 1.4 m and t = 6 m

4.3.1 Demand Reduction Ratios from Relative Maximum Shaft Bending Demands

In order to characterize the expected amount of lateral resistance for a particular case, the problem was framed in terms of a reduction in foundation bending demands from those returned by the pseudo plane strain geometry of the full width embankment cases. These reductions were characterized in terms of a reduction ratio computed by dividing the displacement, shear force, and bending moment demands at each analysis step by the corresponding demands for the wide embankment case with matching soil profile and shaft design. Figures 4.16 through 4.25 show these computed ratios plotted against the free-field displacement in the model. In these plots, a reduction ratio of 1.0 implies no reduction from the plane strain case, while a reduction ratio of less than 1.0 indicates a reduction in the bending demands. For example, a reduction ratio of 0.2 indicates bending demands that were 20 percent of those predicted using something similar to a two-dimensional description of the site geometry.

The reduction ratio plots of figures 4.16 through 4.25 support the observations made in the previous sections while providing a better representation of the relative differences between the maximum bending demands, and thus they illuminate aspects of the geometric site effects that may be obscured in previous plots. Most of the site configurations displayed a similar trend in how the reduction ratios developed; the ratios were lower over the initial portion of the free-field displacement and then gradually increased before reaching an essentially steady-state final value. There were some exceptions to this general trend, particularly for some of the $z = 1$ and 1.5-m configurations. See, for example, figure 4.20, in which the results display the opposite ratio development pattern, with initially higher ratios becoming smaller with increasing free-field displacement. Another trend that was evident in the reduction ratio plots for only certain cases was the tendency for the ratios to initially decrease before they began to gradually increase to

their steady-state values. This decrease to increase trend was particularly evident in the z =3 m cases of figures 4.16-4.25, though it was not observed universally for all such cases. It is not clear whether this was a relevant effect due to these geometric conditions or a numerical effect due to differences in the models between the initial state and the loading state.

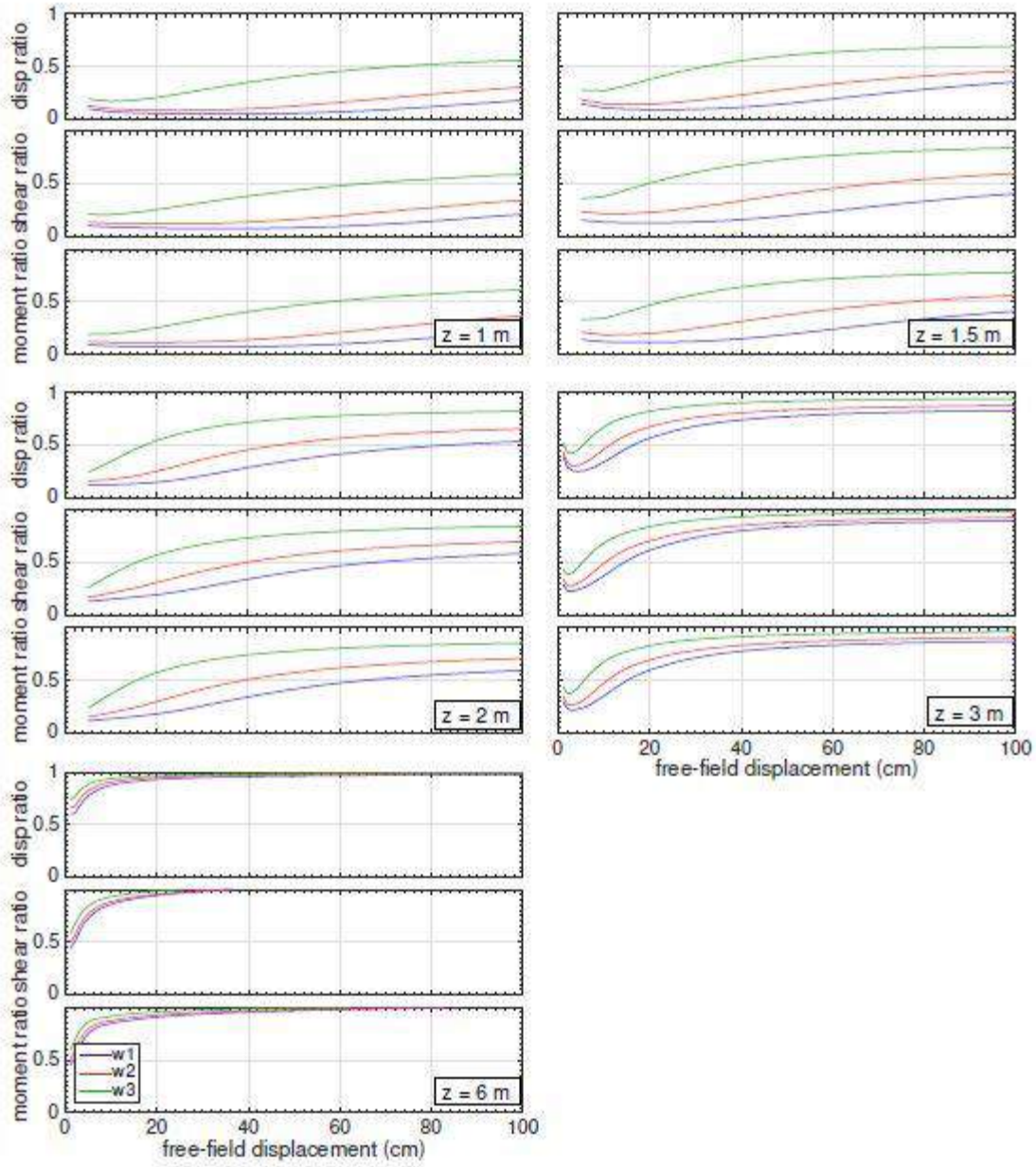

Figure 4.16 Bending demand ratios taken against the full-width embankment case for five crust thicknesses with D = 0.6 m and t = 1 m

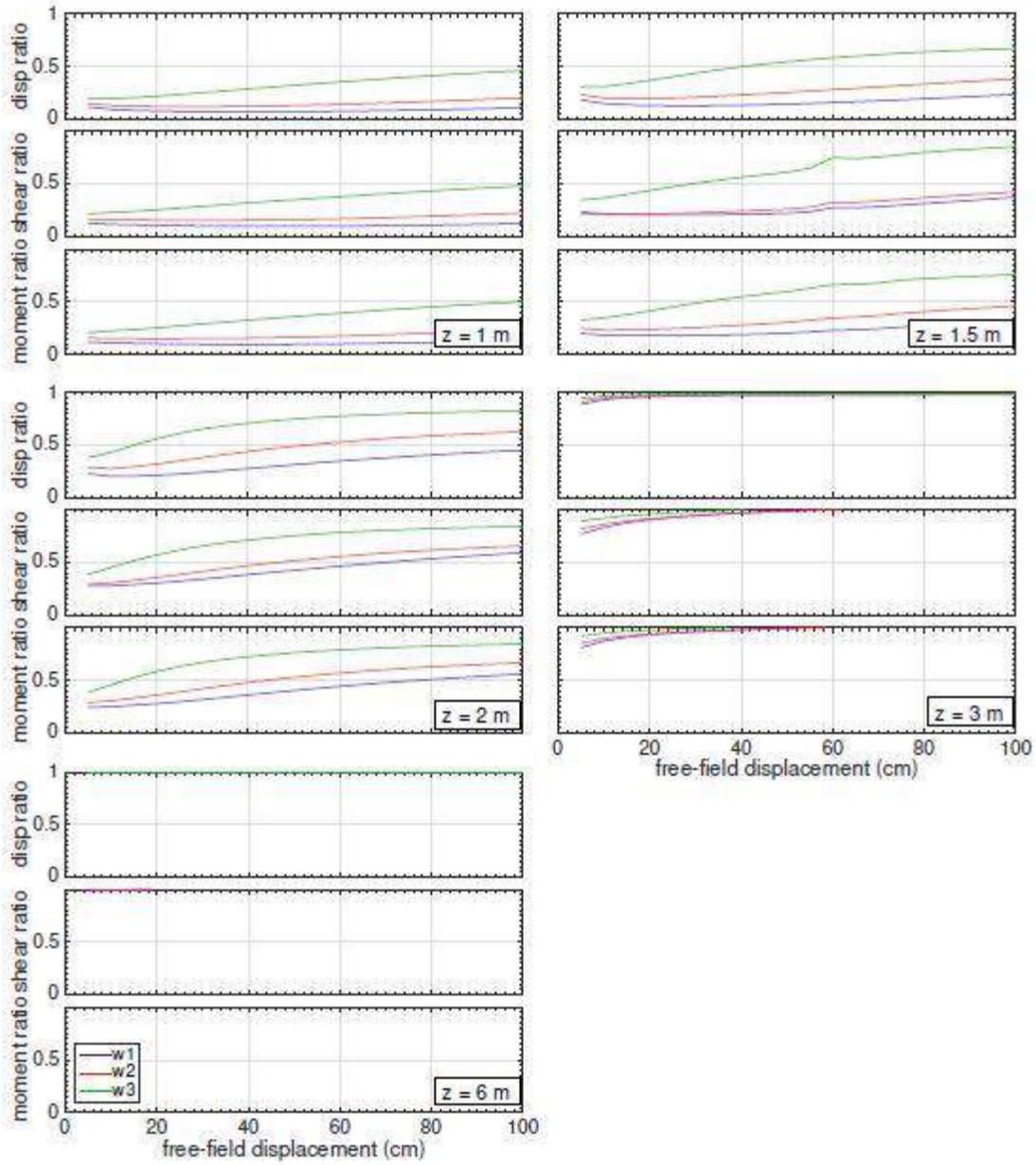

Figure 4.17 Bending demand ratios taken against the full-width embankment case for five crust thicknesses with D = 0.6 m and t = 2 m

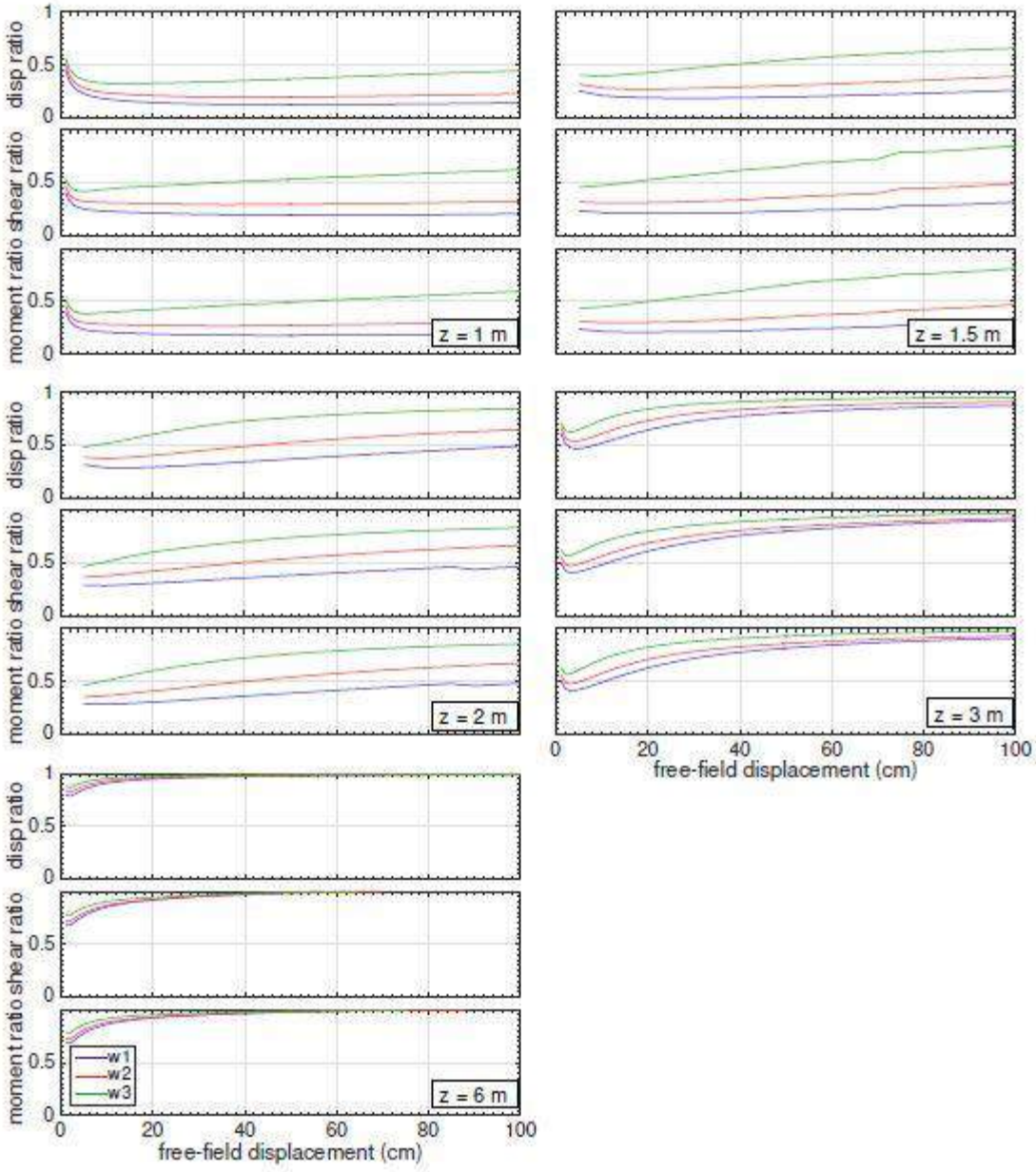

Figure 4.18 Bending demand ratios taken against the full-width embankment case for five crust thicknesses with D = 0.6 m and t = 3 m

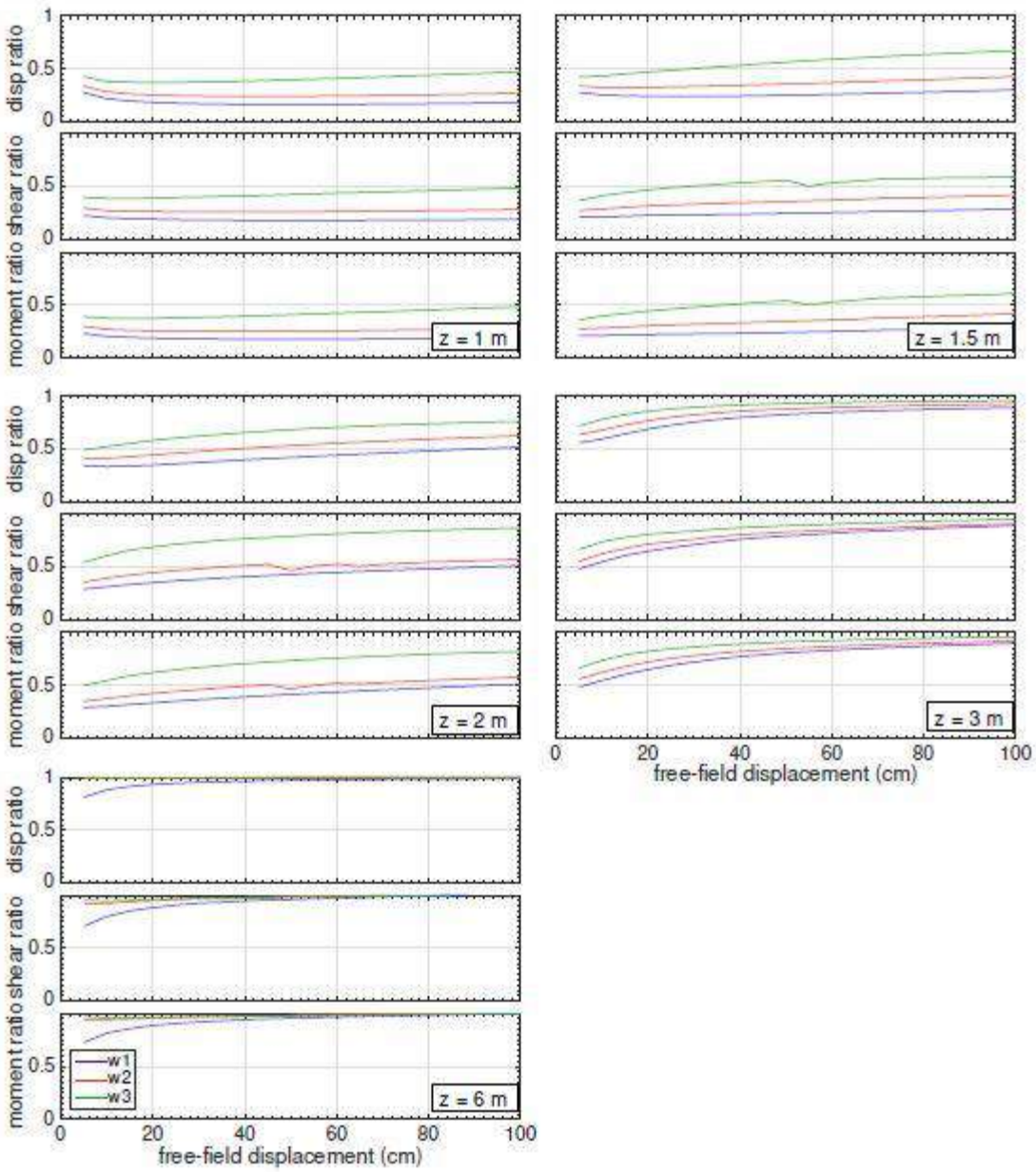

Figure 4.19 Bending demand ratios taken against the full-width embankment case for five crust thicknesses with D = 0.6 m and t = 4 m

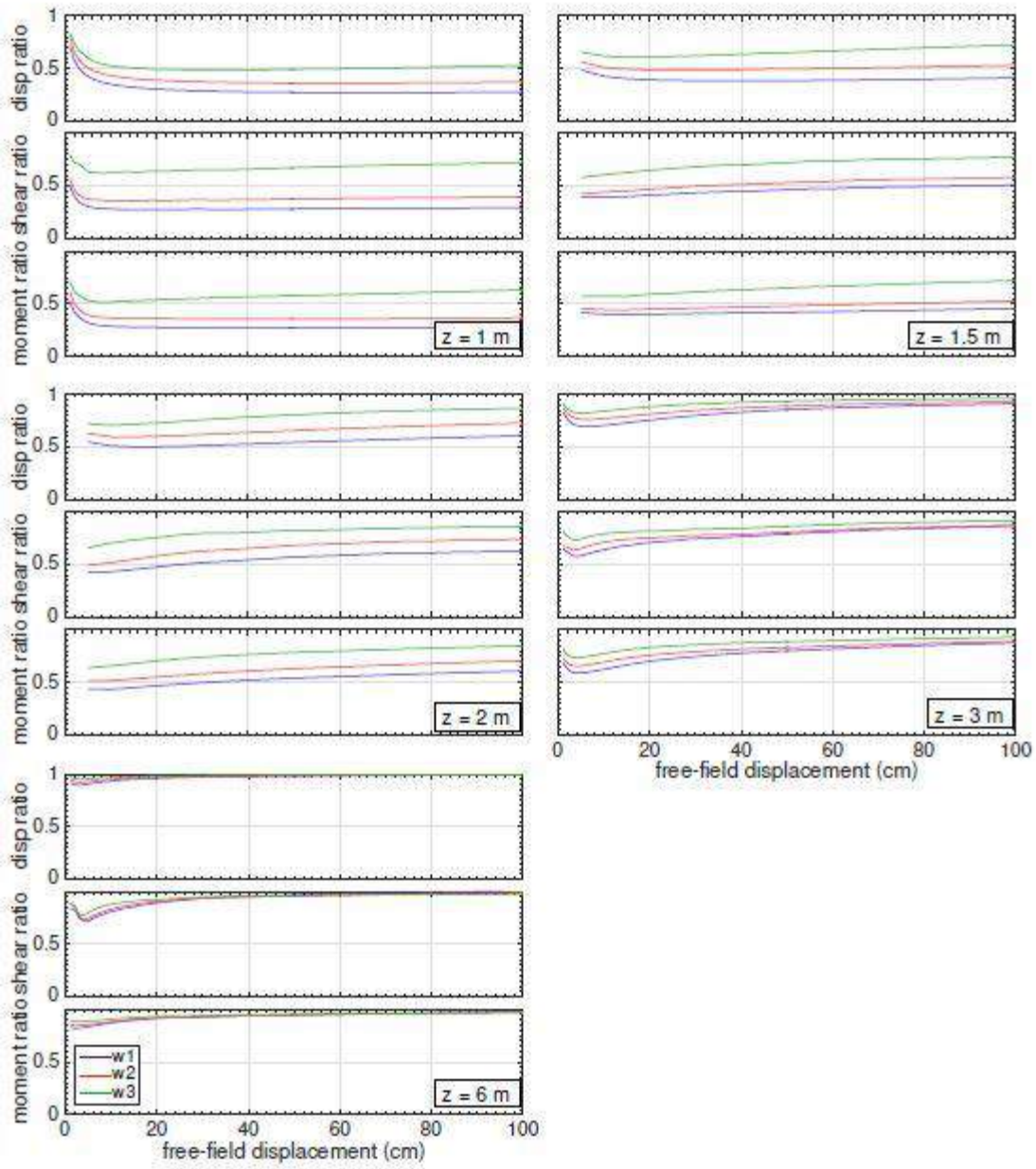

Figure 4.20 Bending demand ratios taken against the full-width embankment case for five crust thicknesses with D = 0.6 m and t = 6 m

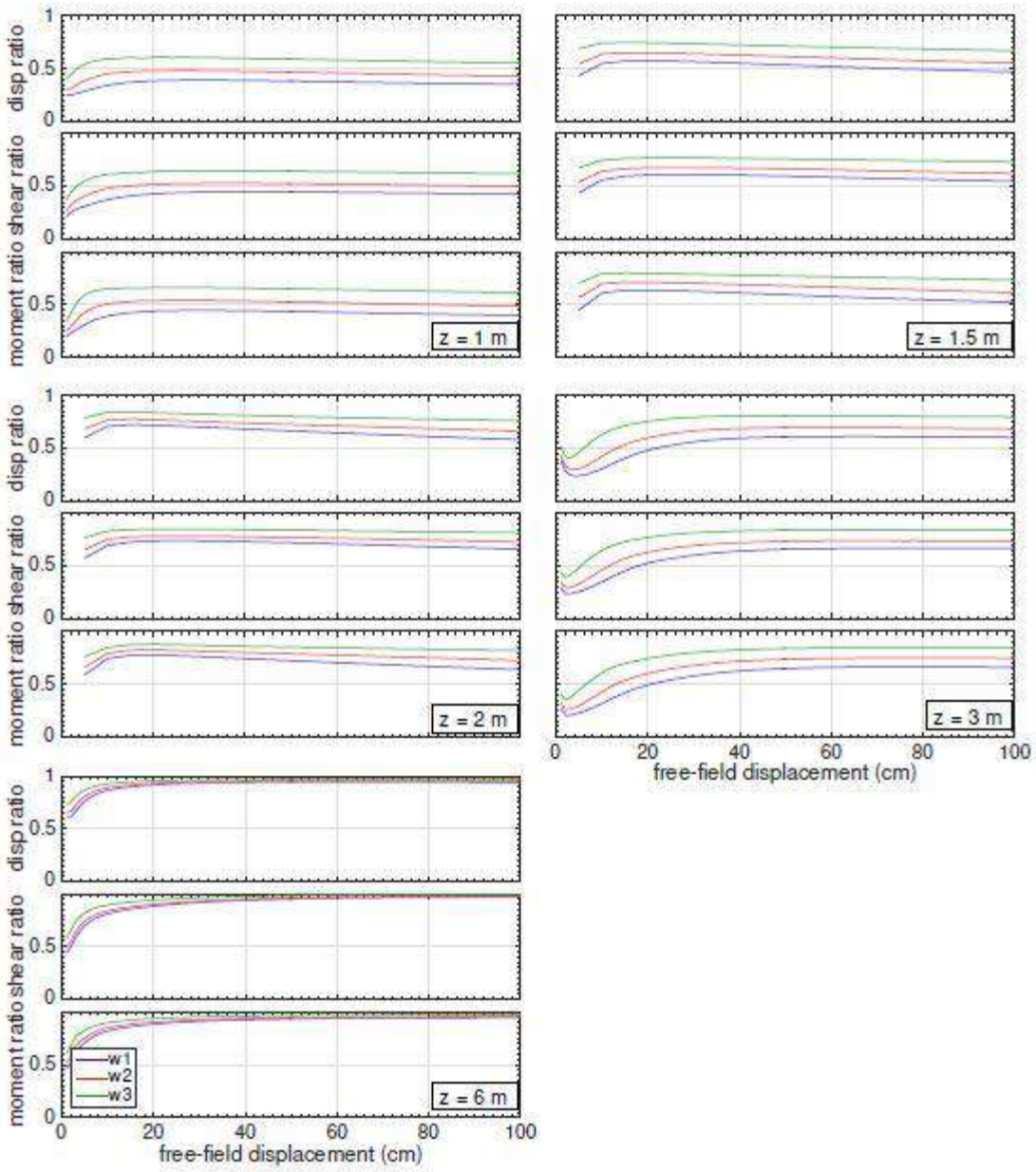

Figure 4.21 Bending demand ratios taken against the full-width embankment case for five crust thicknesses with D = 1.4 m and t = 1 m

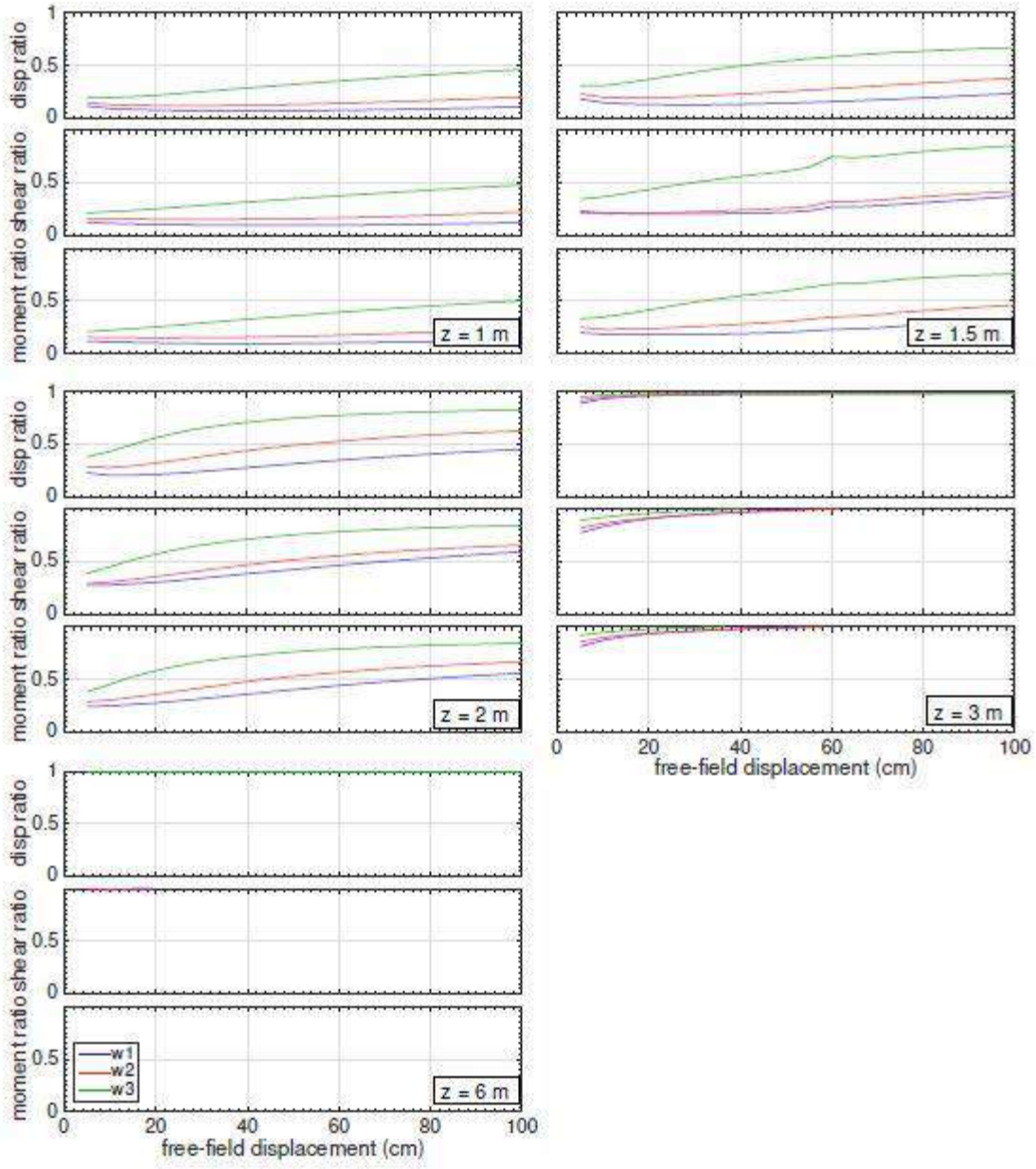

Figure 4.22 Bending demand ratios taken against the full-width embankment case for five crust thicknesses with D = 1.4 m and t = 2 m

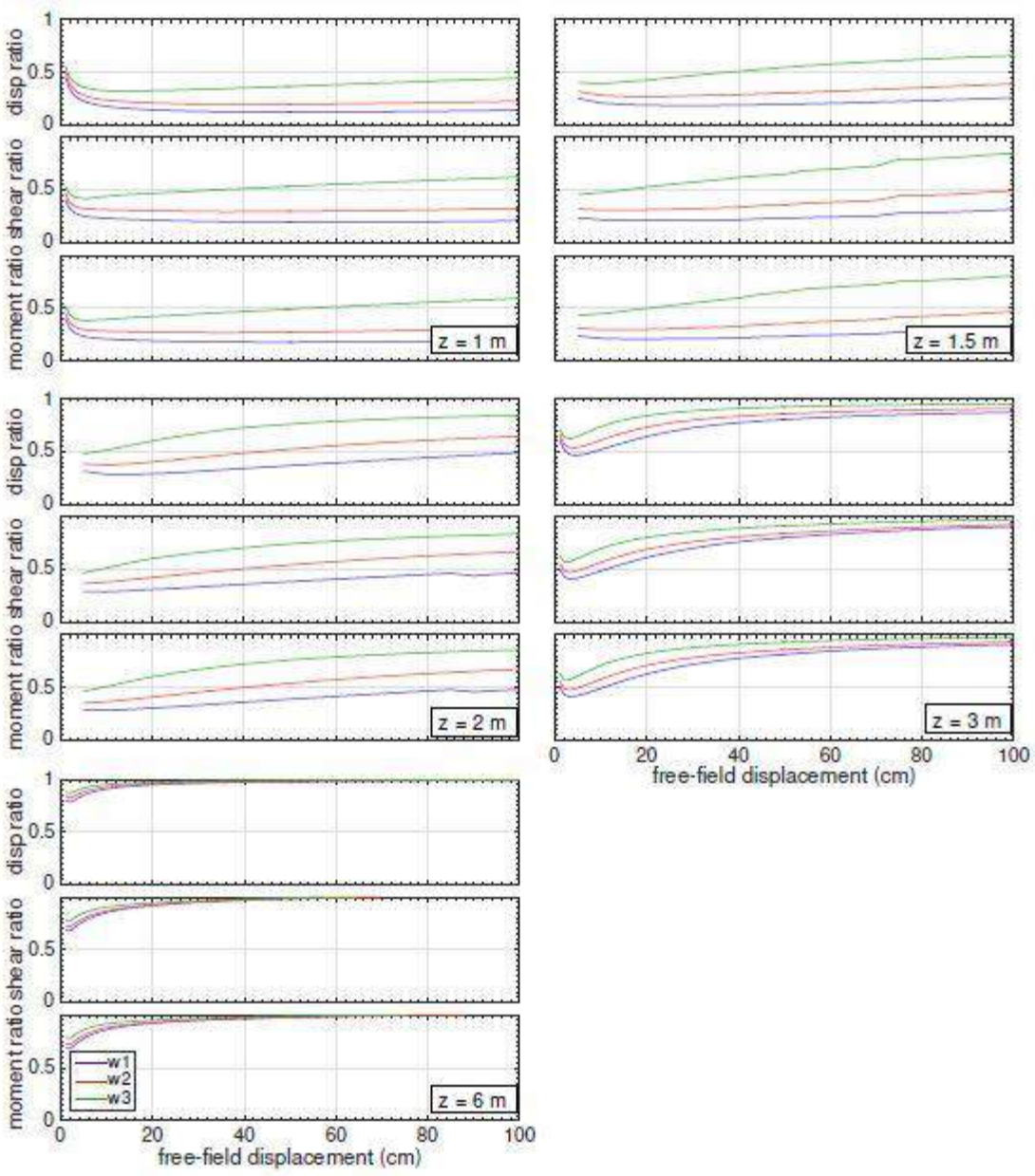

Figure 4.23 Bending demand ratios taken against the full-width embankment case for five crust thicknesses with D = 1.4 m and t = 3 m

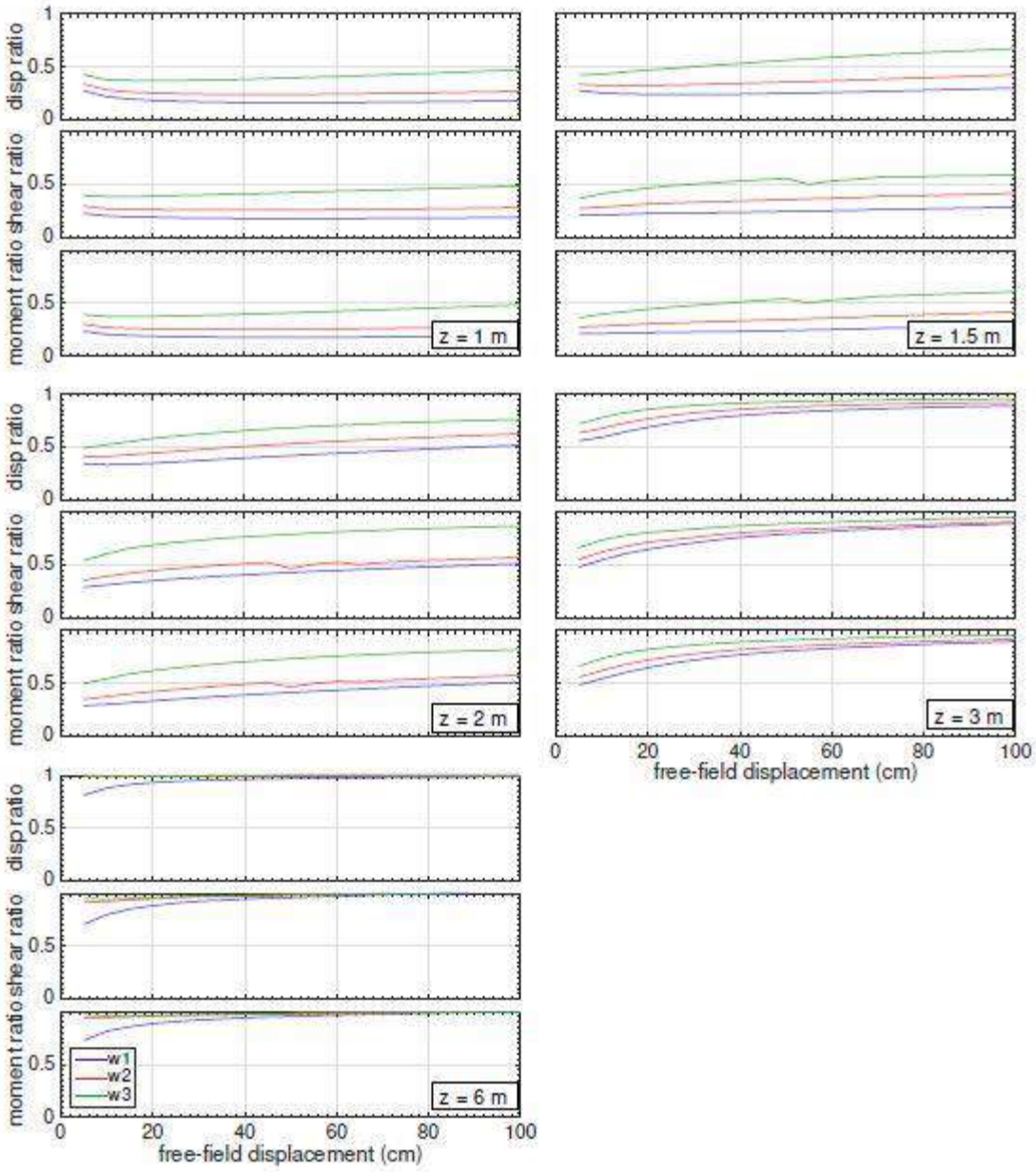

Figure 4.24 Bending demand ratios taken against the full-width embankment case for five crust thicknesses with D = 1.4 m and t = 4 m

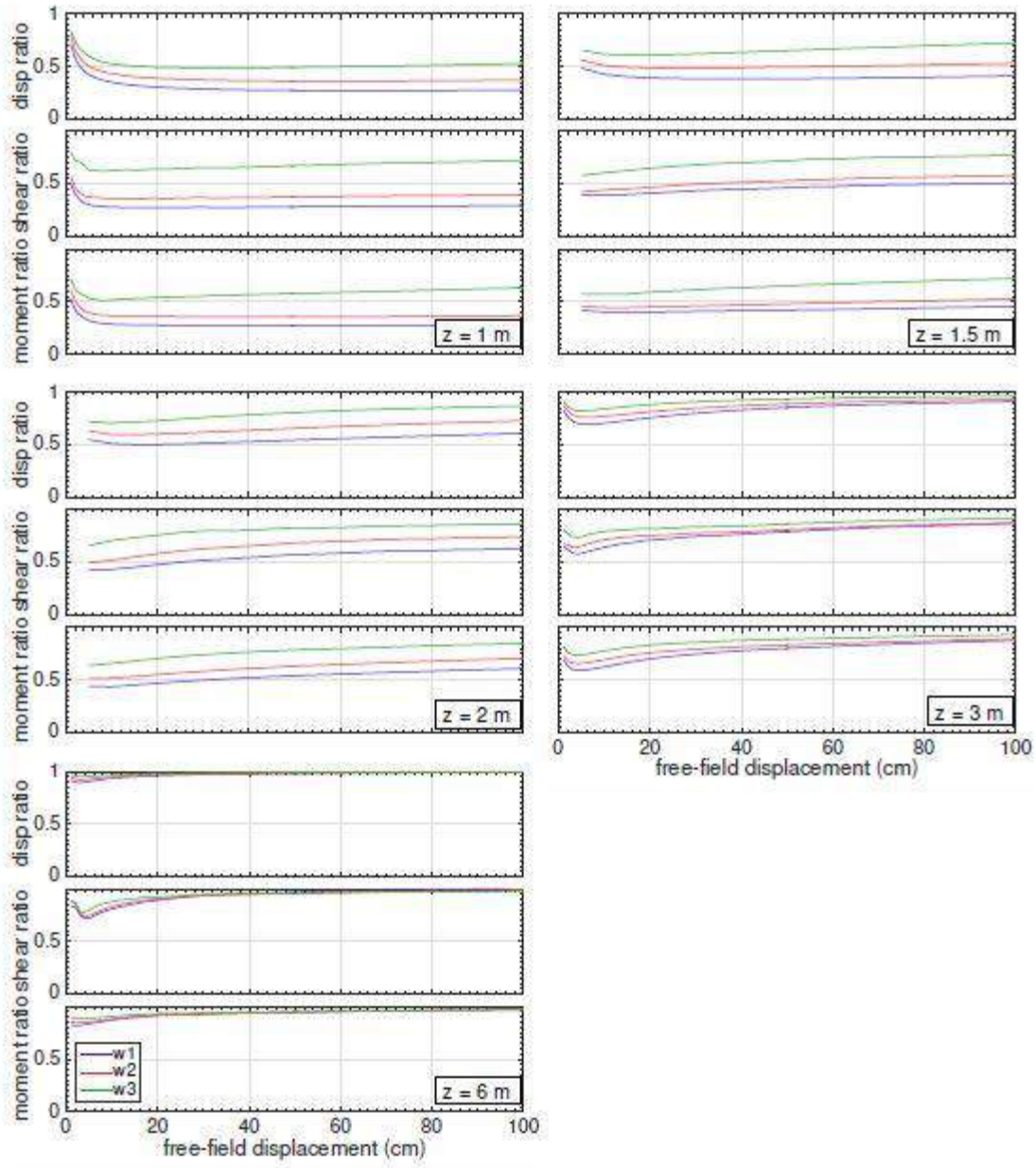

Figure 4.25 Bending demand ratios taken against the full-width embankment case for five crust thicknesses with D = 1.4 m and t = 6 m

4.3.2 Apparent Foundation Pinning from Free-Field Displacement Reduction Ratios

The results in the demand reduction ratio plots of figures 4.16 through 4.25 show that there was little difference between the ratios for the maximum displacement, shear force, and bending moment demands. This lack of difference makes sense in the context of how the models

were configured. Because the shafts were linear elastic, then the shear force and bending moment demands were proportional to the shaft deflections, and because the displaced shapes of the shafts were similar across the four embankment widths for each soil profile, the result was the observed similarity between the displacement, shear force, and moment demand ratios. Because of this similarity, it was possible to assess the bending demand reductions shown in figures 4.16 through 4.25 in terms of the displacement reduction ratios only.

Expanding upon this idea, it was of interest to assess the apparent foundation pinning resistance for each case through an evaluation of the reduction in maximum shaft displacement demand relative to the applied free-field surface displacement. This assessment was made by computing the ratio between the maximum shaft displacement in each case to the corresponding surface displacements applied to the boundaries of the mesh. The free-field reduction ratios for each applied displacement increment were plotted against the corresponding free-field displacement increment for each case in figures 4.26 through 4.35. These free-field reduction ratios provided a more direct evaluation of the apparent foundation pinning resistance in each case than the demand reduction ratios discussed in the previous section, as it was a direct comparison between the free-field and near-field deformation fields.

As expected, the free-field reduction ratios shown in figures 4.26 through 4.35 agreed with the previously discussed results. Increasing embankment crest width resulted in less foundation pinning, and the degree of pinning for each embankment width case depended upon the thickness of non-liquefied crust, thickness of the liquefiable layer, and the shaft foundation stiffness in the ways discussed in previous sections. The insights gained by examining the model results in terms of the free-field reduction ratios relate to how the foundation pinning resistance

changed over the course of the analysis and how this differed for different combinations of site parameters.

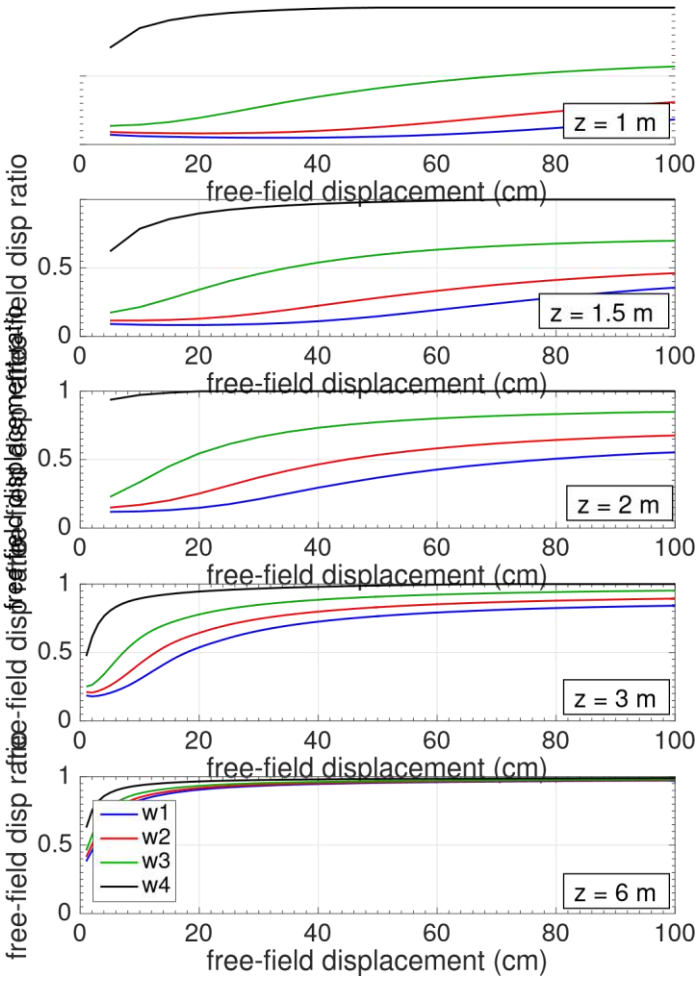

Figure 4.26 Bending demand ratios taken against the free-field displacements for five crust thicknesses with D =0.6 m and t =1 m.

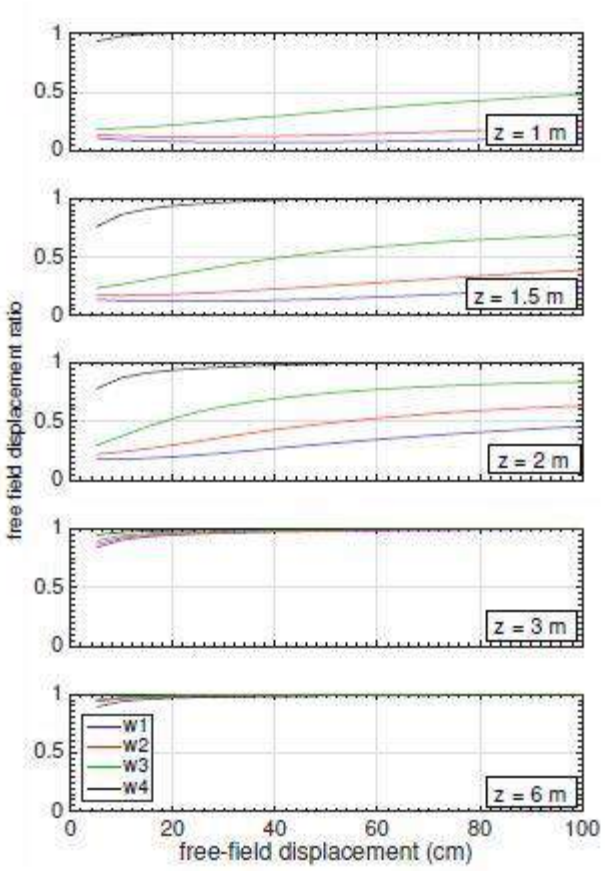

Figure 4.27 Bending demand ratios taken against the free-field displacements for five crust thicknesses with D =0.6 m and t =2 m.

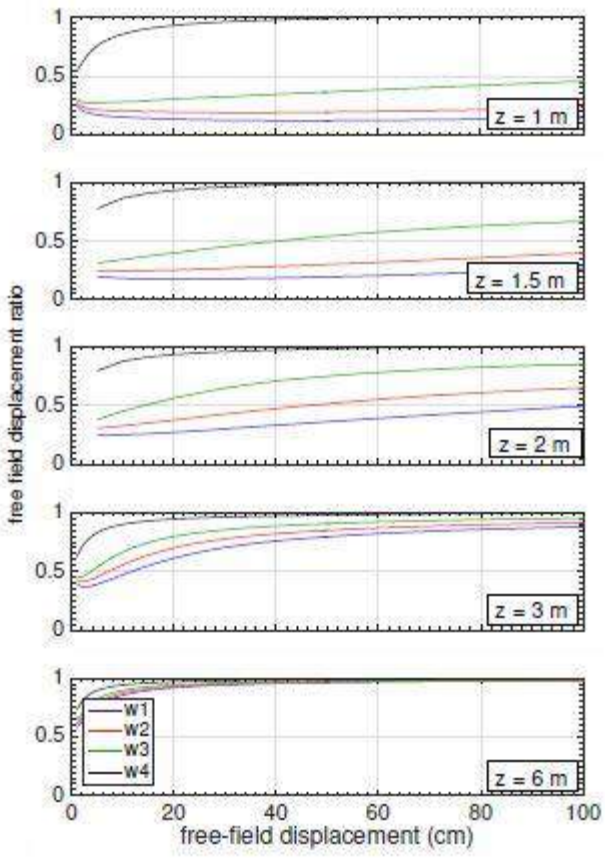

Figure 4.28 Bending demand ratios taken against the free-field displacements for five crust thicknesses with D =0.6 m and t =3m.

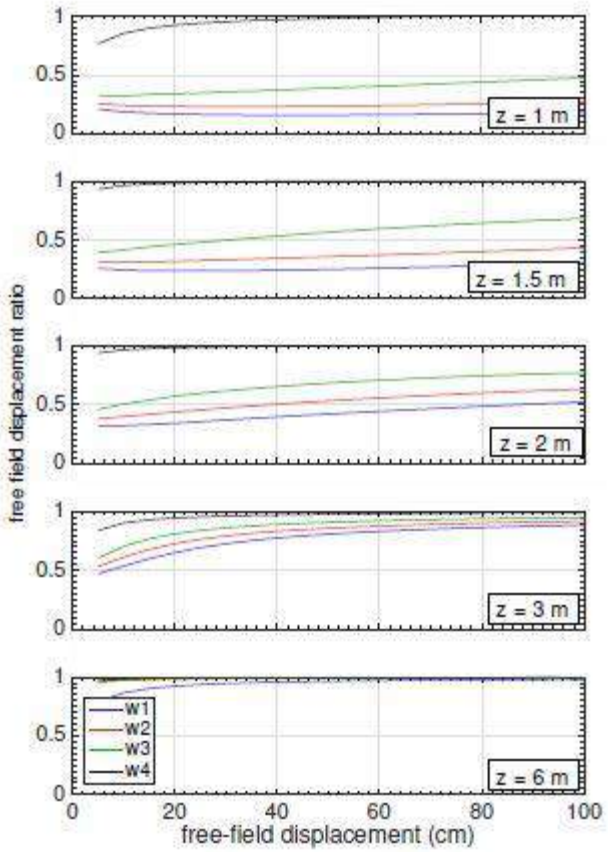

Figure 4.29 Bending demand ratios taken against the free-field displacements for five crust thicknesses with D =0.6 m and t =4 m.

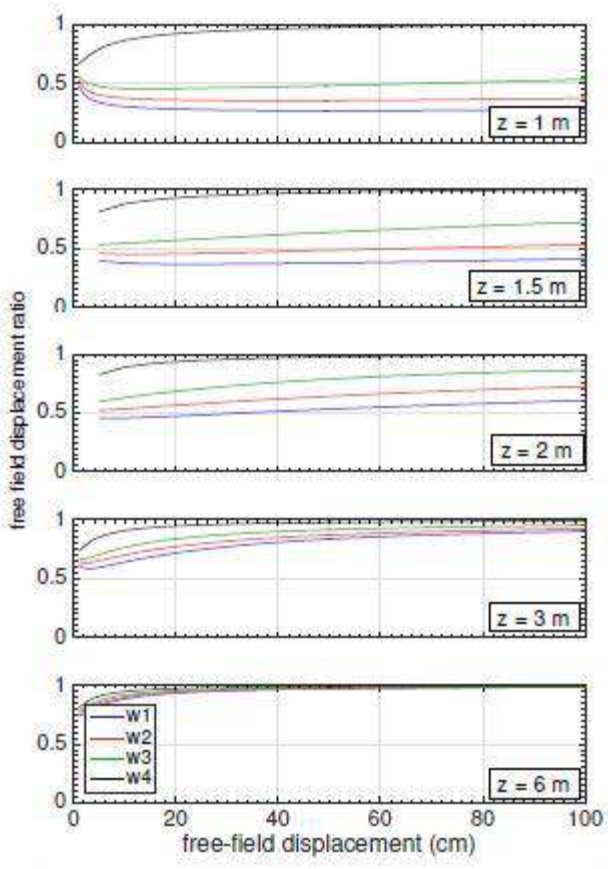

Figure 4.30 Bending demand ratios taken against the free-field displacements for five crust thicknesses with D =0.6 m and t =6 m.

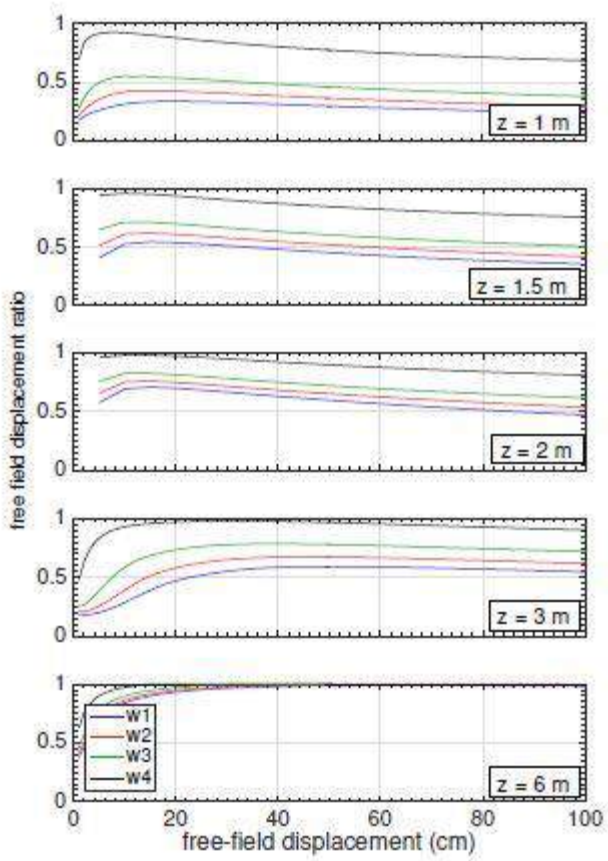

Figure 4.31 Bending demand ratios taken against the free-field displacements for five crust thicknesses with D =1.4 m and t =1 m.

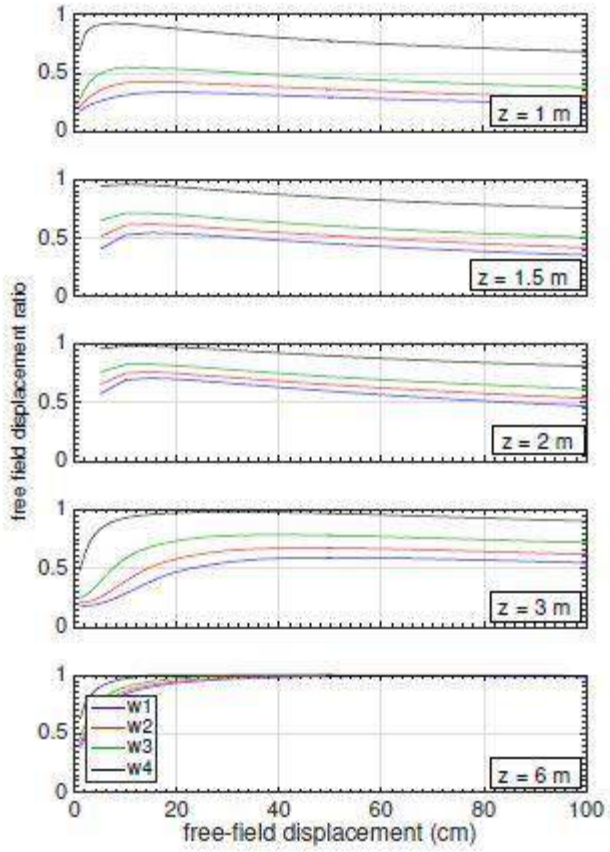

Figure 4.32 Bending demand ratios taken against the free-field displacements for five crust thicknesses with D =1.4 m and t =2 m.

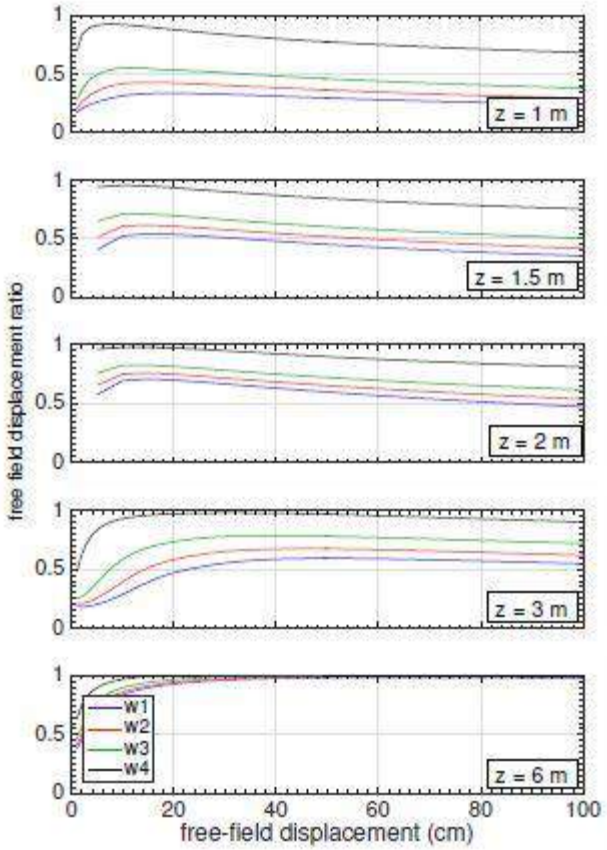

Figure 4.33 Bending demand ratios taken against the free-field displacements for five crust thicknesses with D =1.4 m and t =3 m.

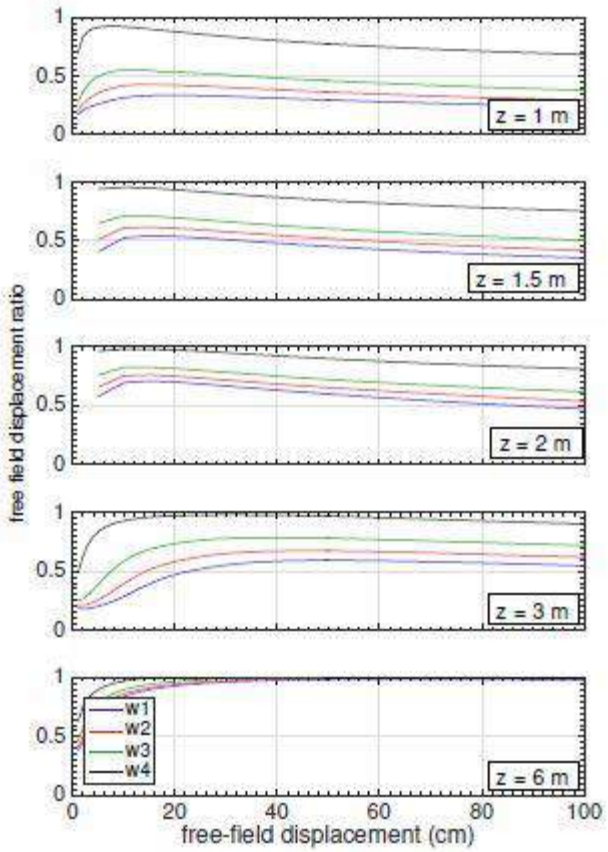

Figure 4.34 Bending demand ratios taken against the free-field displacements for five crust thicknesses with D =1.4 m and t =4 m.

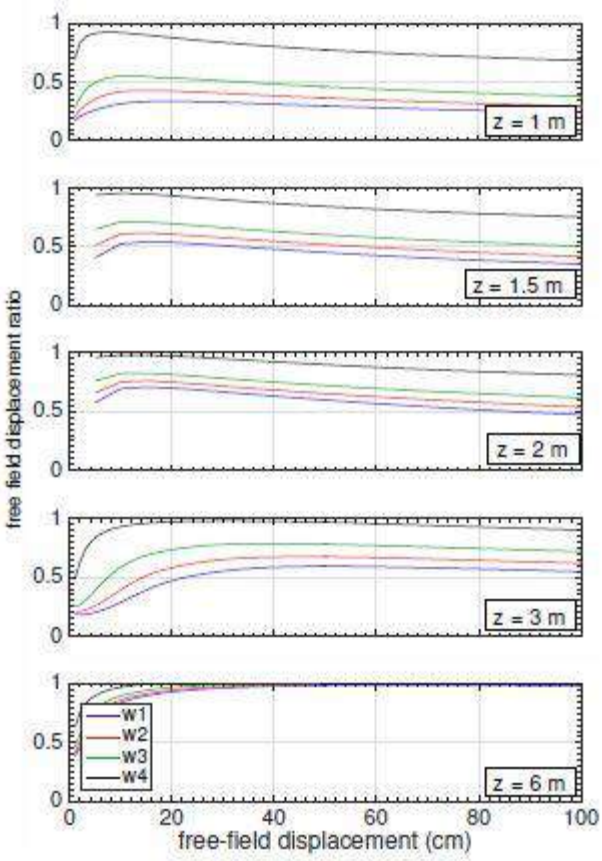

Figure 4.35 Bending demand ratios taken against the free-field displacements for five crust thicknesses with D =1.4 m and t =6 m.

For the 0.6-m-diameter shaft cases of figures 4.26-4.30, it was apparent that for all of the cases, the pinning resistance at the beginning of the analysis was greater than when the full displacement profile had been applied, even for the full embankment width (w4) cases. There was also a clear difference between the z < 3 m and z > 3 m cases for this smaller shaft diameter. When the crust was relatively thin (z < 3 m), the decrease in pinning resistance was more gradual for the w1, w2, and w3 cases, and the pinning resistances at the end of the analyses remained quite large, with free-field reduction ratios of ≤ 80 percent. For the thicker crustal cases (z > 3 m), the decrease in pinning resistance with increasing free-field displacement was more rapid, particularly for the z =6 m cases. These results support the previously made observations related

to crustal thicknesses of 3 m tending to denote the point at which the presence of the approach embankment became less important on the system response. Note also that for the z =1 m cases, there was very little change in the apparent pinning resistance with increasing free-field demands for the 4- and 8-m-wide embankment cases, whereas the 16-m-wide cases showed a much more substantial decrease in resistance over the course of the analysis.

The 1.4-m-diameter shaft results of figures 4.31-4.35 display a different overall trend than those for the 0.6 m diameter shaft. As shown in this second set of figures, the apparent pinning resistance had a low point near the beginning of the analysis where the free-field reduction ratio was larger, then the apparent pinning resistance tended to increase over the course of the analysis as the reduction ratio got smaller. This trend is evident in all of the 1.4-m-diameter shaft results except the deepest liquefiable layer cases with z =6 m. The degree to which the apparent pinning resistance increased differed on the basis of the thickness of the crust, with greater increases in resistance (decreases in ratio) for thinner crusts. On the basis of these results, it did not appear that there was any significant overarching effect of the liquefiable layer thickness on how the reduction ratios changed, as the results were generally similar for all of the liquefiable layer thicknesses.

Figures 4.36 and 4.37 summarize the overall trends in the computed free-field reduction ratios by plotting the average reduction ratio over the 100 cm of displacement against the embankment width and crust thickness for each case, respectively. For this purpose, the tributary embankment width of Boulanger et al. (2006) (see fig. 2.7) was used in lieu of the crest width. Several key trends were observed in figures 4.36 and 4.37. The first observation is given by the lower rows of plots in each figure, where the marker color indicates the thickness of the liquefiable layer; it is clear that there was no definite trend in reduction ratio based on the

liquefiable layer thickness (i.e., the color of the markers is randomly scattered). This supports previous observations in this regard and is in stark contrast to the trends revealed in the upper rows of plots, in which the marker color represents the crust thickness (for fig. 4.36) and embankment width (for fig. 4.37). On the basis of the clear bands of marker color in these plots, it is clear that increasing embankment width and crust thickness led to less reduction in foundation bending demands.

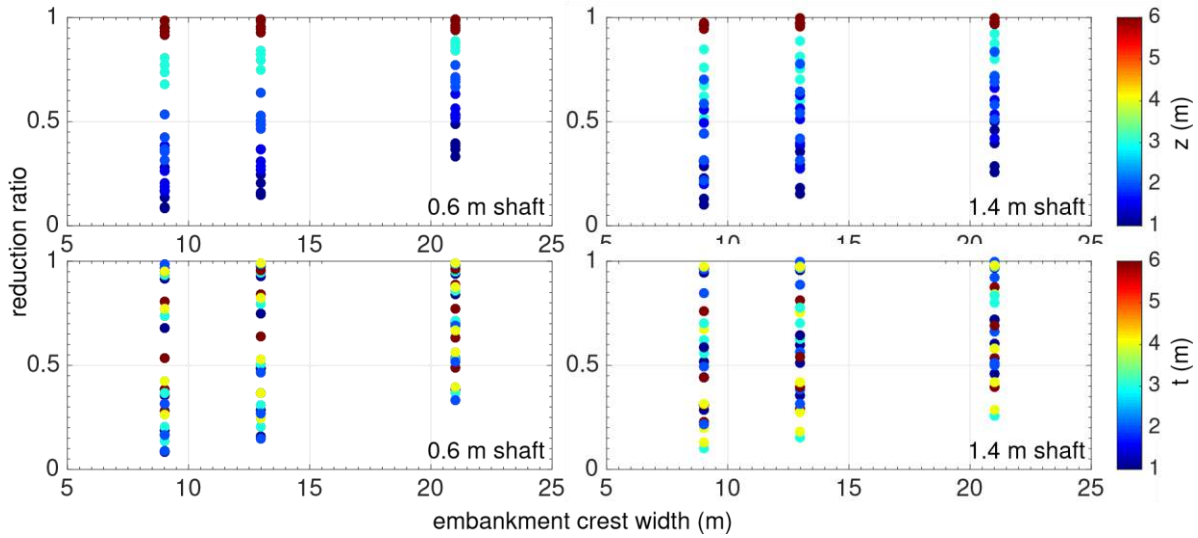

Figure 4.36 Variation in bending demand reduction ratio with tributary embankment width for 0.6- and 1.4-m-diameter shaft cases. In upper row, marker color denotes thickness of crust (z). In lower row, marker color denotes thickness of liquefiable layer (t).

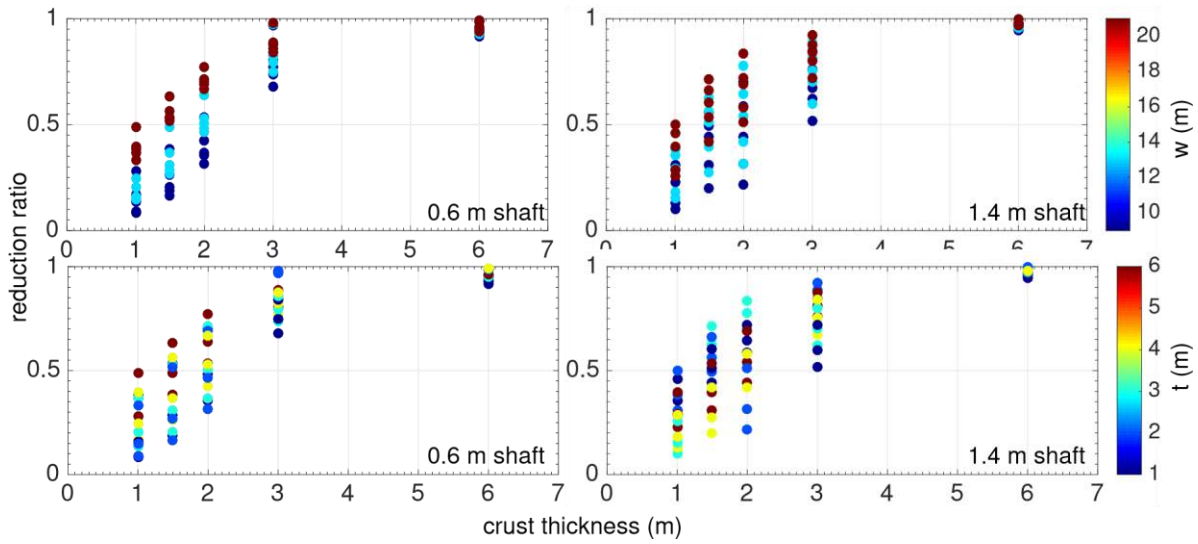

Figure 4.37 Variation in bending demand reduction ratio with non-liquefied crust thickness for 0.6- and 1.4-m-diameter shaft cases. In upper row, marker color denotes embankment width (w). In lower row, marker color denotes thickness of liquefiable layer (t).

Perhaps the most interesting observation gained from figures 4.36 and 4.37 is that the crust thickness appeared to be a more prominent factor in the determination of the reduction ratio than the embankment width. This can be observed by comparing the non-trend displayed by the plots of figure 4.36 with the clearly indicated trend suggested by the plots of figure 4.37. This can also be observed directly from the upper left plot of figure 4.36. As shown, increasing the width of the embankment reduced the spread in the reduction ratio values and shifted the lowest reduction ratio value from about 0.1 to 0.3; however, the difference affected by increasing the crust thickness was much larger. For example, increasing the crust thickness from 2 to 3 m resulted in an increase in the lowest reduction ratio from about 0.3 to about 0.7 for the narrowest embankment width case.

Also note that changing the size and stiffness of the shaft foundation did not have a significant effect on the overall results shown in figures 4.36 and 4.37. The data points for the 1.4-m-diameter shaft cases are more clustered toward the bottom of the reduction ratio ranges for

each embankment width, whereas the points for the 0.6 m cases are concentrated more towards the top, but the overall ranges of reduction ratios indicated in figures 4.36 and 4.37 are not really very different across the two foundation cases. Obviously, the trends identified in the previous discussion still hold, i.e., for a larger/stiffer shaft, greater increases in embankment width and/or crust thickness were necessary to affect the same change in reduction ratio as for the 0.6-m shaft, but the apparent trends in reduction ratio are actually quite similar. This could be due to the fact that these single shafts did not have bending stiffness difference sufficient to affect dramatic changes in the results. Perhaps a third, much stiffer shaft could be considered in any future iterations of this research.

4.4 Estimation of Foundation Pinning Resistance from 3D FEA Parameter Study Results

The results shown in figures 4.36 and 4.37 provide a general overview of the results of the entire 3D FEA parameter study regarding how the different site geometric parameters affect the level of apparent foundation pinning resistance during lateral spreading (with the reduction ratio as the descriptive parameter for level of resistance). Because of the general similarity between the forms of the plots for the two pile diameters, and the clear linear trends denoting the upper and lower bounds for different crust thicknesses in figure 4.36, it is possible to generalize these results into a single chart that can be used to estimate the expected level of pinning resistance given a particular embankment width and crustal thickness. The chart developed through this generalization is shown in figure 4.38. Each of the colored bands represents a different crust thickness, with the band for z =4-5 m filled in from the boundaries suggested for z =6 and z =3 m in figure 4.36. The white zone below z =1 m theoretically represents crusts of less than 1 m thick; however, it is not recommended that the results be extrapolated into this zone.

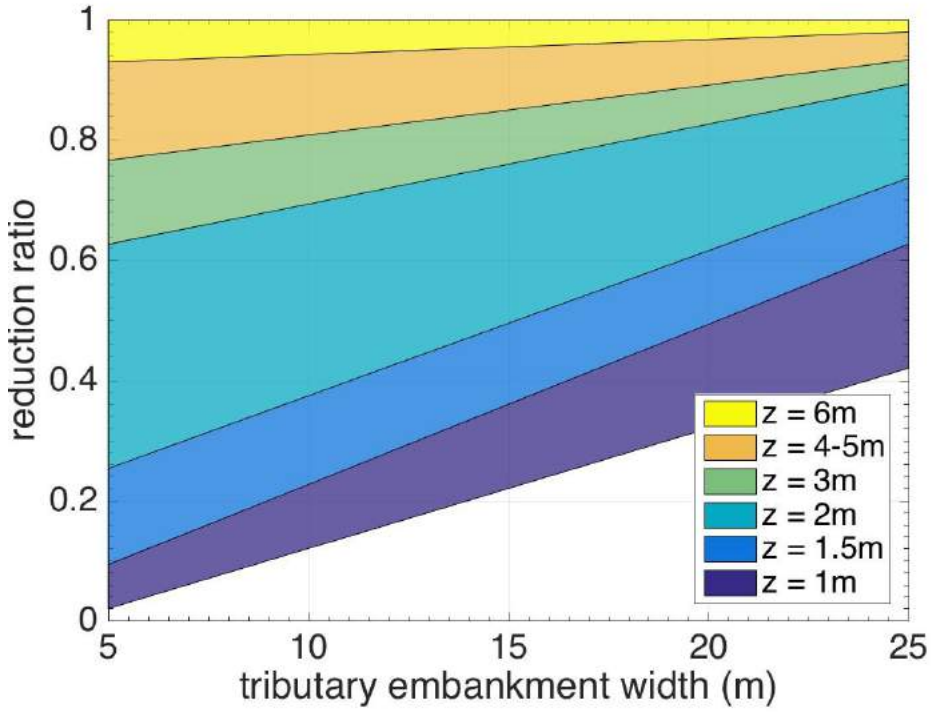

Figure 4.38 Chart for estimation of expected level of pinning resistance, given embankment crest width and thickness of non-liquefiable crust.

To use this chart to determine the reduction ratio (which indicates the expected level of pinning in a general sense) for a given tributary embankment width and crust thickness, one simply needs read up the chart for the particular embankment width value, select the colored band corresponding to the crust thickness, and read off the corresponding bounding reduction ratio values. These values provide an idea of the level of pinning resistance that may be expected based on the results of the 3D FEA parameter study, with lower values of reduction ratio indicating greater pinning resistance, and reduction ratios near 1.0 indicating essentially no expected pinning resistance. On the basis of the results of figures 4.36 and 4.37, the 0.6-m-diameter shaft results plot closer to the upper bound lines for each constant *z* zone, while the 1.4-m-diameter shaft results tend to plot lower down in the zones; thus it is suggested that users of

this chart use reasonable judgment in the particular placement within the crust thickness zones based on the expected stiffness of the foundation to be considered.

4.4.1 Limitations and Caveats

The results shown in figure 4.38 have already been extrapolated such that they depict the trends for the full range of tributary embankment widths from 5 to 25 m. Therefore, it is not recommended that these results be extrapolated further for widths not represented here. It is also not recommended that the reduction ratio values obtained from this plot be used to supplant or supersede results from other lateral spreading analyses, such as those from the equivalent static analysis (ESA) approach discussed in Chapter 2. Rather, the intended use of this figure is to provide an idea of the expected level of pinning resistance for a given site. This information can be used, for example, to help make the decision to use the restrained or unrestrained ground displacement cases from the ESA approach, or it can be used as an independent first-order approximation to determine whether the results from an ESA make sense in the context of the 3D FEA parameter study presented in this report. The scope and level of validation in the 3D FEA parameter study are not nearly at a level for this chart to be used for lateral spreading design in the absence of other analytical methods. It is recommended that care be used whenever this chart is applied to any particular site or project.

4.5 Summary

A series of 3D finite element models were used to examine the influence of various geometric site parameters on the response of a single deep foundation to the kinematic demands of lateral spreading. These models focused on assessing the effects of changes in the embankment width, the thickness of non-liquefied crust, the thickness of the liquefied layer, and the bending stiffness of the foundation. The observed effects were framed within the context of a

reduction in foundation bending demands in comparison to a quasi-plane strain description of the site in which the embankment extends across the full width of the model domain. The apparent foundation pinning resistance for each combination of site geometric parameters was assessed through the ratio of the maximum shaft displacement demand (the near-field deformation) to the applied ground surface demand on the boundaries of the mesh (the free-field deformation demands). The results showed that there is a clear effect of the site geometry on apparent pinning resistance and the demand reduction ratios, and that there is an interplay between the various considered geometric parameters such that variations in no one parameter can fully explain the differences among the various cases. A chart that synthesizes the overall findings of the parameter study regarding the expected level of foundation pinning was produced. While it is not recommended that this chart be used to supplant more established design and analysis procedures, it offers a first-order approximation of the level of pinning resistance that may be expected for a particular site.

Chapter 5 Development and Analysis of Equivalent Static Analysis Models

The restrained ground deformation case as laid out by Ashford et al. (2011) and Caltrans (2011), and as described in detail in Chapter 2 of this report, was used to develop and analyze equivalent static analysis (ESA) models for each of the geometric combinations discussed in Chapter 3. To this purpose, beam on nonlinear Winkler foundation (BNWF) models were generated and analyzed with OpenSees (McKenna et al., 2010; McKenna, 2011), and pseudo-static slope stability models were generated and analyzed with SLOPE/W (GEO-SLOPE, 2016). The details of these model development and analysis activities are discussed in the following sections, followed by a discussion of the overall results of the ESA parameter study and comparisons to the results of the 3D FEA parameter study.

5.1 Equivalent Static Model Development for Parameter Study Cases

5.1.1 BNWF Model Development

The BNWF models for the ESA parameter study were developed and analyzed with the open source finite element analysis platform OpenSees. Displacement based beam-column elements were used to represent the shaft foundation, and *p-y* springs linked to each beam node were used to model the soil response to lateral loading. The PySimple01 uniaxial material implemented in OpenSees after the work of Boulanger et al. (1999, 2003) was used for this purpose, along with zero-length spring elements. The *p-y* materials for the embankment fill, dry loose sand, and dense sand layers were created by using the sand-type backbone curve and the properties of table 3.1, with ultimate strengths defined on the basis of the method of Brinch Hansen (1961) and initial stiffness values defined by using the API (2007) approach, with the depth dependent stiffness correction of Boulanger et al. (2003). For consistency with the 3D FEA, the response of the embankment fill was modeled with the same approach as the other non-

liquefiable soil layers, rather than the trilinear soil response curve and rigid abutment section that would normally be used in an application of the pile pinning ESA to a bridge foundation. The *p-y* materials for the liquefiable loose sand layer were defined with the clay-type backbone curve. The ultimate strength and initial stiffness for the *p-y* curves in this layer were defined by using the same methods as the other layers, but with the undrained strength listed in table 3.1 as the input into the Brinch Hansen (1961) and API (2007) equations. To account for the presence of the softer liquefied layer in the *p-y* curves of the surrounding stiffer layers, the ultimate strength profiles within the loose and dense sand layers were reduced linearly following the approach summarized in figure 2.2.

The beam-column elements representing the shaft foundations were assigned the linear elastic material and section properties listed in table 3.2. The overall modeling approach for the shafts in these ESA models is identical to that employed in the 3D finite element analyses discussed in the Chapter 4. The BNWF models were analyzed by using a lateral spreading pushover approach, with a set displacement profile applied to the soil end of the *p-y* curve spring elements as indicated in figure 2.4. The surficial displacement applied in all models was 200 cm, though as is clear in the ensuing discussion, this does not mean that the top of the shaft was displaced by this amount in all cases. The inclusion of the two shaft diameters/designs in the parameter study necessitated a total of 50 individual BNWF pushover models for the ESA version of the parameter study, i.e., five crust thicknesses, five liquefiable layer thicknesses, and two shaft diameters (embankment widths could be explicitly considered in this context).

5.1.2 Slope Stability Model Development

The slope stability models for the ESA parameter study were developed and analyzed by using a pseudo-static procedure with the commercial limit equilibrium slope stability analysis

software package SLOPE/W (GEO-SLOPE, 2016). An example of the model layout for these analyses is provided in figure 5.1. The embankment fill, dry loose sand, and dense sand layers were modeled with a Mohr-Coulomb failure surface with the friction angles listed in table 3.1.

The liquefiable loose sand layer was modeled as an undrained material, with an S_u/σ_v ratio of 0.1 and a baseline value taken from table 3.1. The forward face of of the embankment was assigned a 2H:1V slope in the loading direction, as shown in figure 5.1, and the presence of the shaft foundation was considered by using a constant resisting force applied at the center of the liquefiable soil layer. As discussed by Armstrong et al. (2014), this approach neglects any additional resistance from the internal shaft bending moment, but because the moment is at (or very near) zero in the center of the liquefiable layers for the 3D analyses (see figures 4.4 and 4.5), this is a reasonable simplification. The method of Spencer (1967) was used to compute all factors of safety in the slope stability analyses. For consistency with the 3D FEA, a deck resisting force was not considered in these slope stability analyses (as there was no deck resisting force in the 3D models).

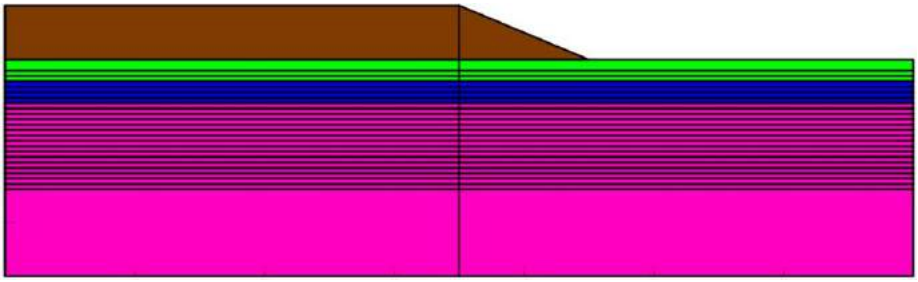

Figure 5.1 Example model domain set-up for pseudo-dynamic slope stability analysis. Layer colors correspond to those in chapters 3 and 4.

The slope stability analyses for the ESA parameter study were carried out by determining the horizontal yield acceleration values that result in a stability factor of safety of 1.0 for a series of seven shaft resisting forces (V =0, 50, 100, 200, 400, 800, and 1600 kN) for each of the 25

combinations of crustal and liquefiable layer thicknesses. The yield accelerations determined for each case are listed in table 5.1. For the purposes of discussion (and to simplify the labels for this table) the five crust thickness cases are referred to as z1, z2, z3, z4, and z5 for the 1.0-, 3.0-, 6.0-, 1.5-, and 2.0-m crusts, respectively. Similarly, the liquefiable layer thickness cases are referred to as t1, t2, t3, t4, and t5 for the 1.0-, 3.0-, 6.0-, 2.0-, and 4.0-m liquefiable layer thicknesses, respectively. The case IDs in the first column of table 5.1 refer to the site geometries in this manner, e.g., case z1t4 has a 1-m-thick crust and a 2-m-thick liquefiable layer.

In order to obtain curves describing the expected level of deformation for each resisting force and site geometry, the rigid Newmark sliding block regression equation of Bray and Travasarou (2007) was used to compute displacements from the yield acceleration values listed in table 5.1 for each case. To this purpose, a reference magnitude M =7.0 and a reference PGA of 0.4 g were assumed. The displacement values computed from the Bray and Travasarou (2007) equation for each yield acceleration were obviously influenced by these assumed values but were not overly sensitive to minor variations in M or PGA. The necessity for these assumed values was a shortcoming of the current analysis approach; however, because the important factor for comparisons within the results of the ESA parameter study, and to the results of the 3D FEA parameter study, was that the values for all ESA cases were computed in a consistent manner, the assumption of constant values (however arbitrary) met the needs of the current study.

Table 5.1 Yield acceleration values for range of foundation resisting forces V for all considered soil profiles (forces listed in kN, accelerations listed in g).

Soil Profile	V =0	V =50	V =100	V =200	V =400	V =800	V =1600
z1t1	0.085	0.175	0.234	0.250	0.385	0.530	0.787
z1t2	unstable	0.022	0.055	0.115	0.195	0.325	0.585
z1t3	unstable	0.005	0.025	0.058	0.118	0.225	0.453

z1t4	unstable	0.055	0.085	0.185	0.265	0.415	0.715
z1t5	unstable	0.006	0.035	0.085	0.155	0.288	0.532
z2t1	0.225	0.250	0.270	0.305	0.365	0.490	0.710
z2t2	0.105	0.125	0.140	0.163	0.216	0.325	0.550
z2t3	0.074	0.088	0.100	0.125	0.175	0.284	0.545
z2t4	0.148	0.165	0.180	0.215	0.285	0.420	0.665
z2t5	0.085	0.100	0.115	0.145	0.205	0.325	0.550
z3t1	0.360	0.407	0.415	0.440	0.480	0.560	0.720
z3t2	0.240	0.250	0.260	0.288	0.330	0.415	0.580
z3t3	0.200	0.210	0.220	0.235	0.270	0.348	0.575
z3t4	0.300	0.310	0.320	0.350	0.400	0.478	0.624
z3t5	0.210	0.220	0.230	0.245	0.281	0.362	0.590
z4t1	0.118	0.170	0.200	0.268	0.350	0.450	0.732
z4t2	unstable	0.035	0.065	0.120	0.191	0.330	0.600
z4t3	unstable	0.017	0.040	0.065	0.115	0.225	0.475
z4t4	0.031	0.078	0.110	0.170	0.255	0.340	0.615
z4t5	unstable	0.020	0.048	0.090	0.150	0.265	0.506
z5t1	0.160	0.200	0.235	0.288	0.360	0.420	0.710
z5t2	0.035	0.065	0.094	0.135	0.193	0.319	0.568
z5t3	0.025	0.045	0.059	0.080	0.129	0.228	0.495
z5t4	0.075	0.110	0.140	0.180	0.258	0.366	0.620
z5t5	0.029	0.049	0.073	0.108	0.164	0.270	0.495

The cases listed as *unstable* in table 5.1 had a factor of safety of less than 1.0 for yield accelerations of 0.0 g. This only occurred when no foundation resisting force was considered, and a particular type of site profile seemed prone to this instability. As shown in table 5.1, the unstable cases were for site profiles with thin crust thicknesses (z1 = 1.0-m thick; z4 = 1.5-m thick) and generally thicker liquefiable layer configurations (with the exception of case z1t4, all had liquefiable layer thicknesses of ≥ 3 m). The Bray and Travasarou (2007) rigid Newmark equation was not applied to the unstable cases to determine corresponding displacement values; therefore, these data points were not used in the subsequent determination of the compatible displacement states, as discussed in the following section.

5.2 Equivalent Static Analysis Results – Determination of Compatible States

The compatibility points for the BNWF pushover and slope stability/deformation analysis phases were determined by plotting the force-displacement curves obtained from each phase for each case and finding the points of intersection of the two curves. Figures 5.2–5.6 show these plots for the 0.6-m-diameter shaft cases, and figures 5.7–5.11 show them for the 1.4-m-diameter shaft cases, with the numerical results summarized in tables 5.2 and 5.3, respectively.

In accordance with Ashford et al. (2011), the results from the BNWF pushover analyses are presented in terms of the running average shear force in the center of the liquefiable layer for increasing levels of displacement at the top of the shaft foundation. This use of the running average attempted to correct for the incompatibility in how the two analysis phases considered the shear force, i.e., shear force increased with increasing foundation displacement in the BNWF models but was constant for all displacement levels in the slope stability/deformation analyses. The effect of the embankment width was considered in these comparisons by scaling the slope stability resisting forces (which were technically on a force-per-unit-length basis) by the tributary

embankment crest width after Boulanger et al. (2006) and Ashford et al. (2011) and as summarized in figure 2.7. For the full width (w4) cases, the actual model width of 35-m was used for this purpose, as there was not a side slope with which to compute a tributary width. For cases, such as the t =2 m case in figure 5.2, where one or more of the slope deformation curves did not intersect the pushover curve, the compatibility points were determined by visual extrapolation of the force-displacement curves. This extrapolation was not ideal, but it was deemed appropriate given the relatively low number of cases for which it was necessary.

The case naming scheme introduced for table 5.1 was adopted for tables 5.2 and 5.3, with z1, z2, z3, z4, and z5 corresponding to the 1.0-, 3.0-, 6.0-, 1.5-, and 2.0-m crust thicknesses, respectively, and t1, t2, t3, t4, and t5 for the 1.0-, 3.0-, 6.0-, 2.0-, and 4.0-m liquefiable layer thicknesses, respectively. The embankment width cases are designated in figures 5.2–5.11 and tables 5.2–5.3 using the same scheme used previously throughout Chapter 4 of this report, with w1, w2, w3, and w4 corresponding to the 4-m, 8-m, 16-m, and full width cases, respectively.

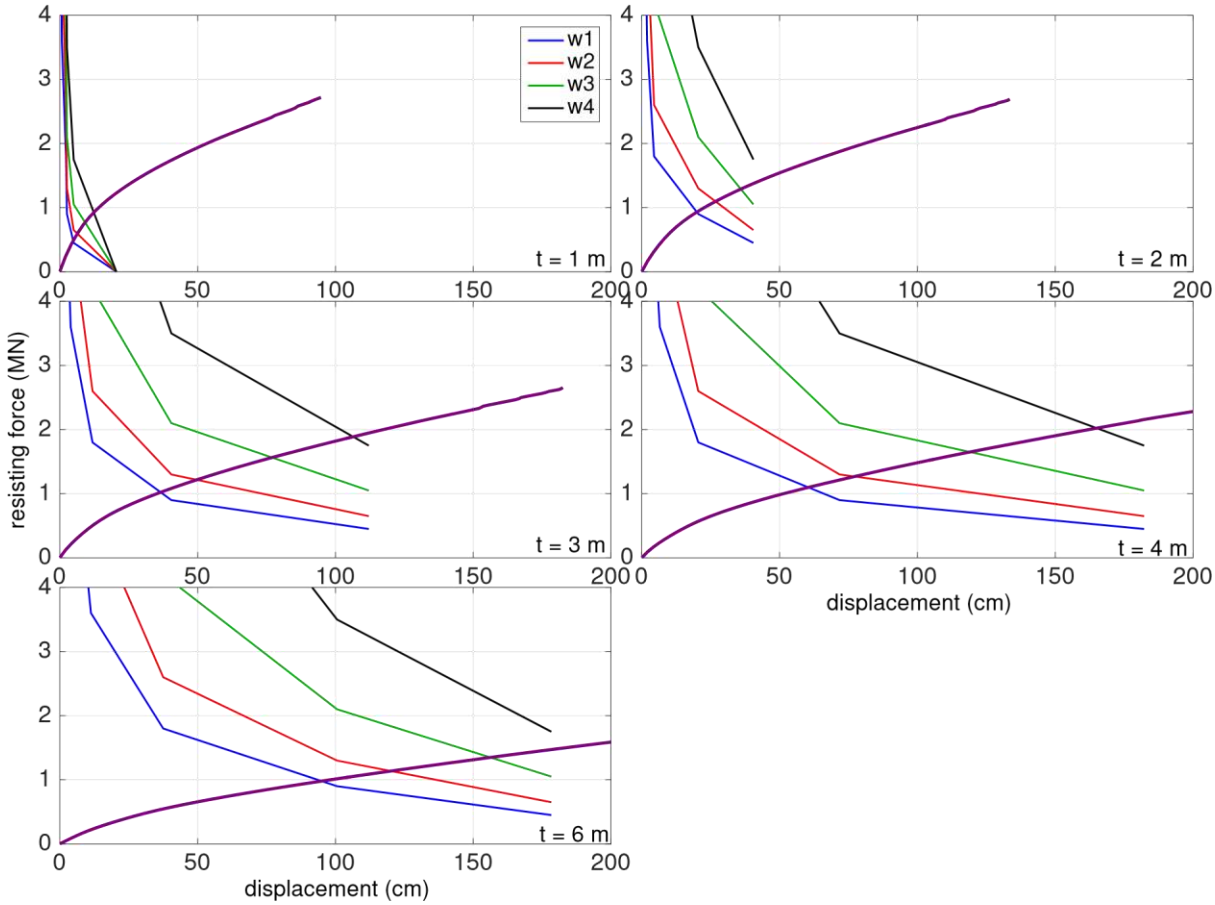

Figure 5.2 Determination of compatible displacement from pushover and slope deformation curves for five liquefiable layer thicknesses and four embankment crest widths with a 1.0-m crustal thickness and 0.6-m diameter shaft

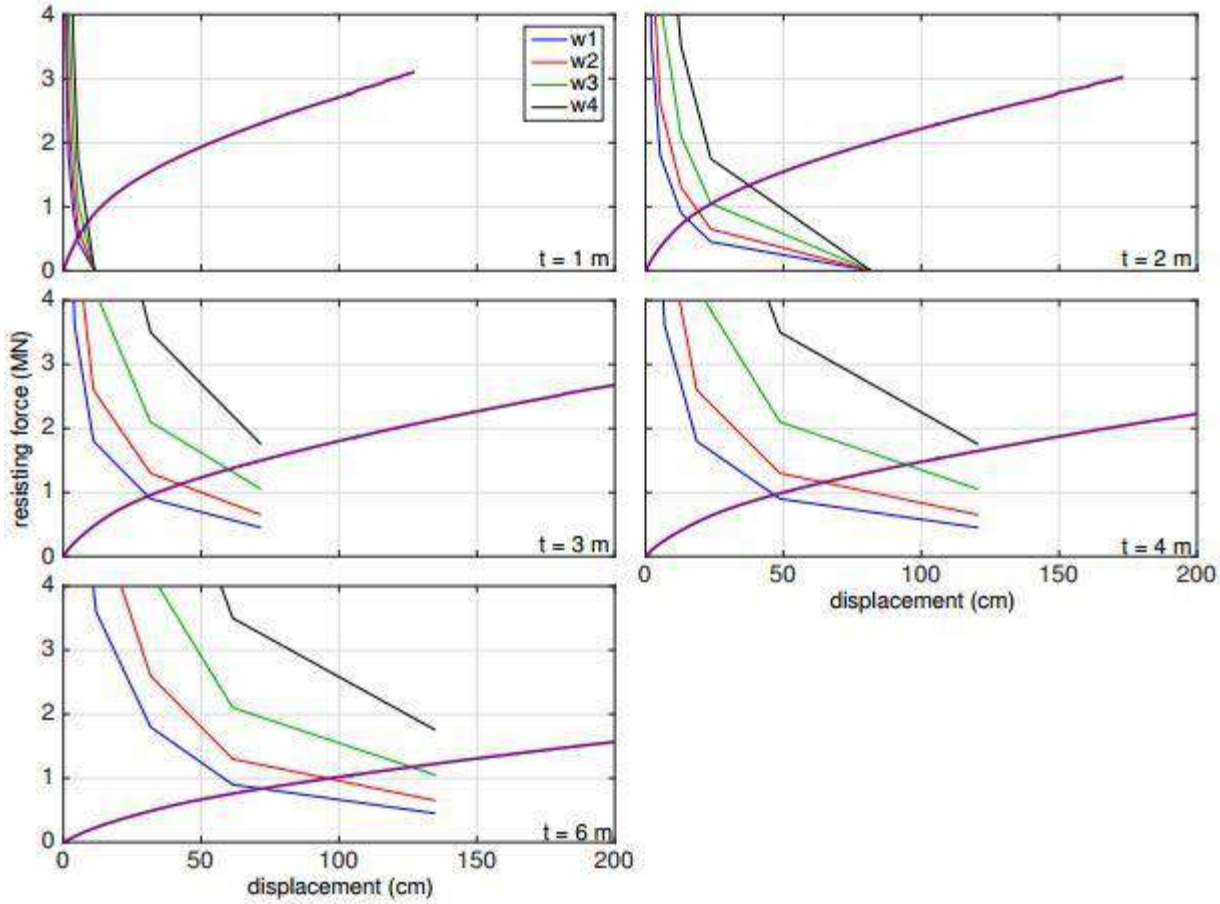

Figure 5.3 Determination of compatible displacement from pushover and slope deformation curves for five liquefiable layer thicknesses and four embankment crest widths with a 1.5-m crustal thickness and 0.6-m diameter shaft

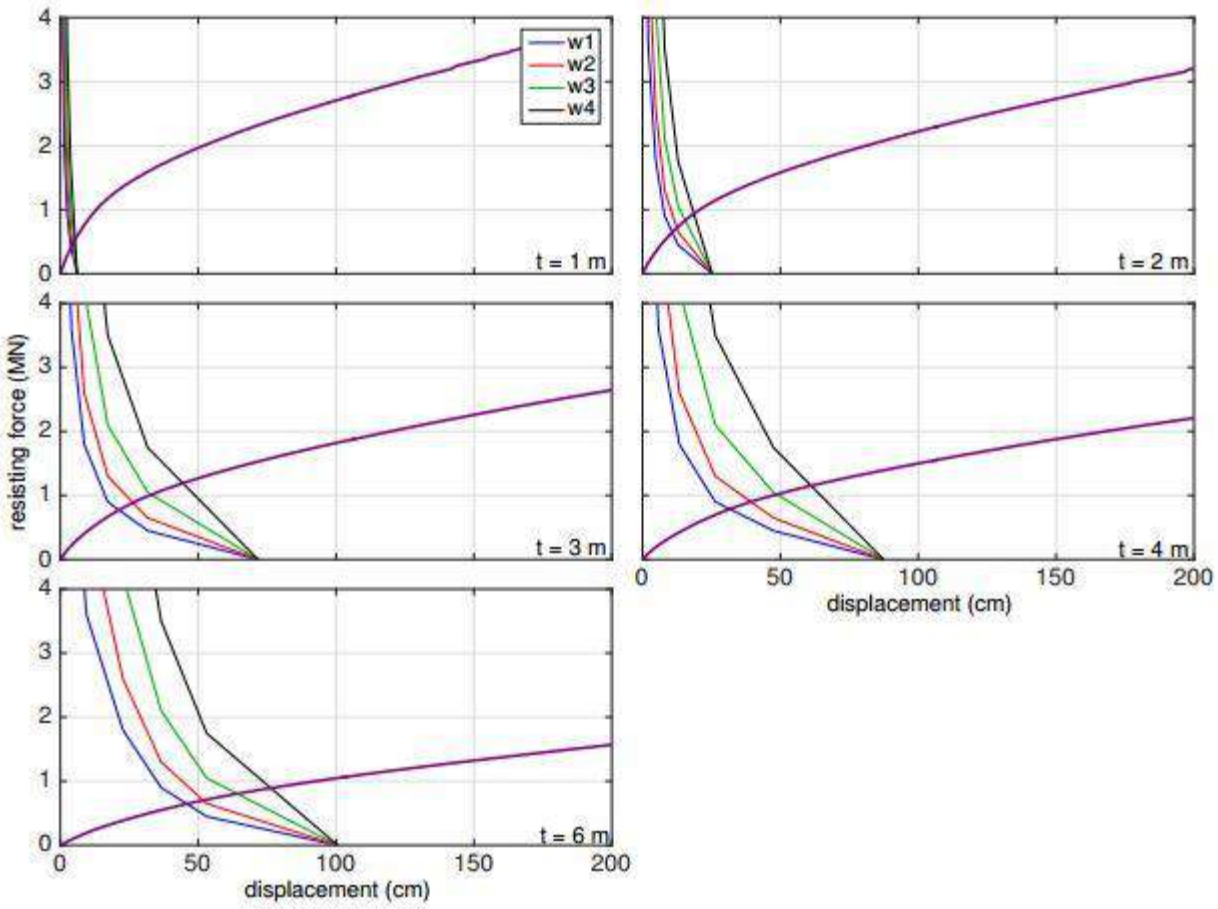

Figure 5.4 Determination of compatible displacement from pushover and slope deformation curves for five liquefiable layer thicknesses and four embankment crest widths with a 2.0-m crustal thickness and 0.6-m diameter shaft

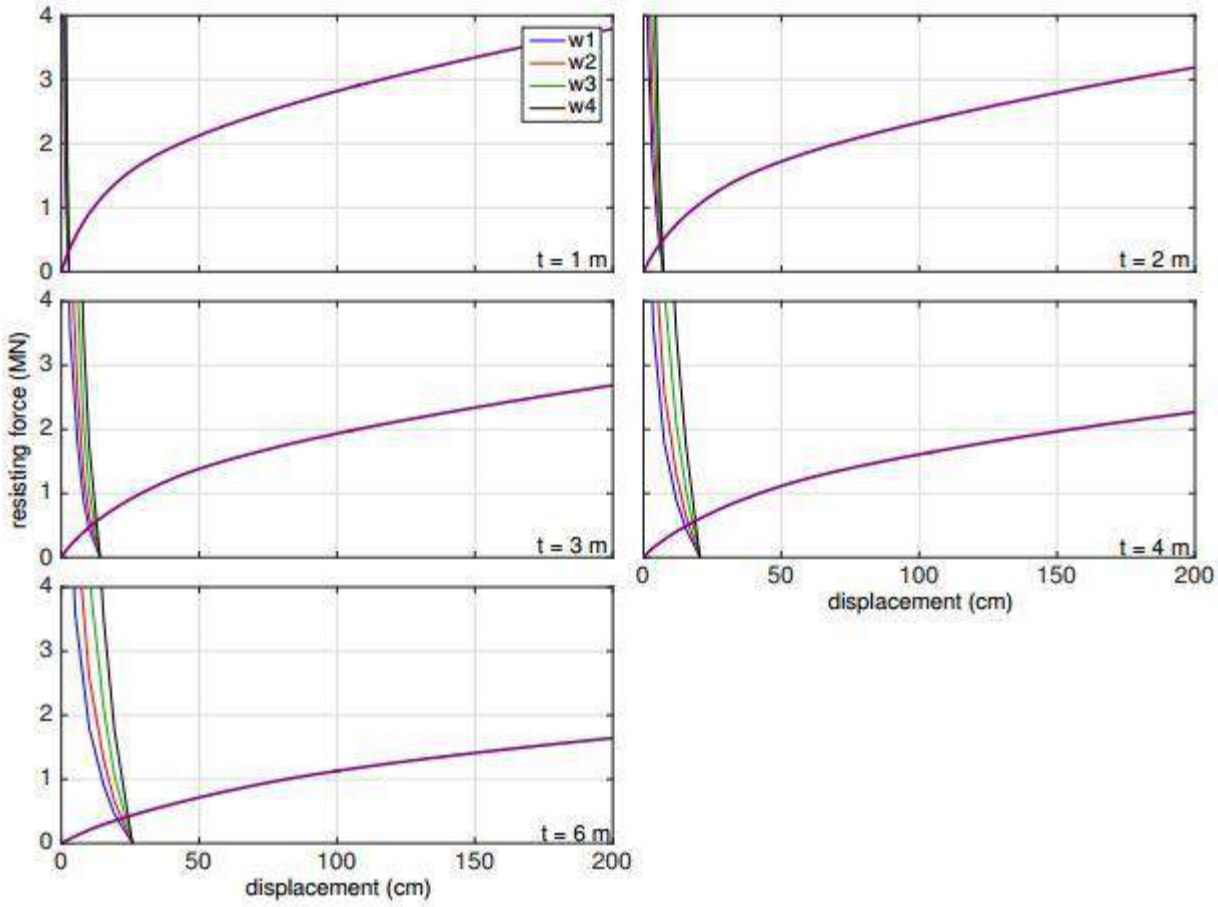

Figure 5.5 Determination of compatible displacement from pushover and slope deformation curves for five liquefiable layer thicknesses and four embankment crest widths with a 3.0-m crustal thickness and 0.6-m diameter shaft

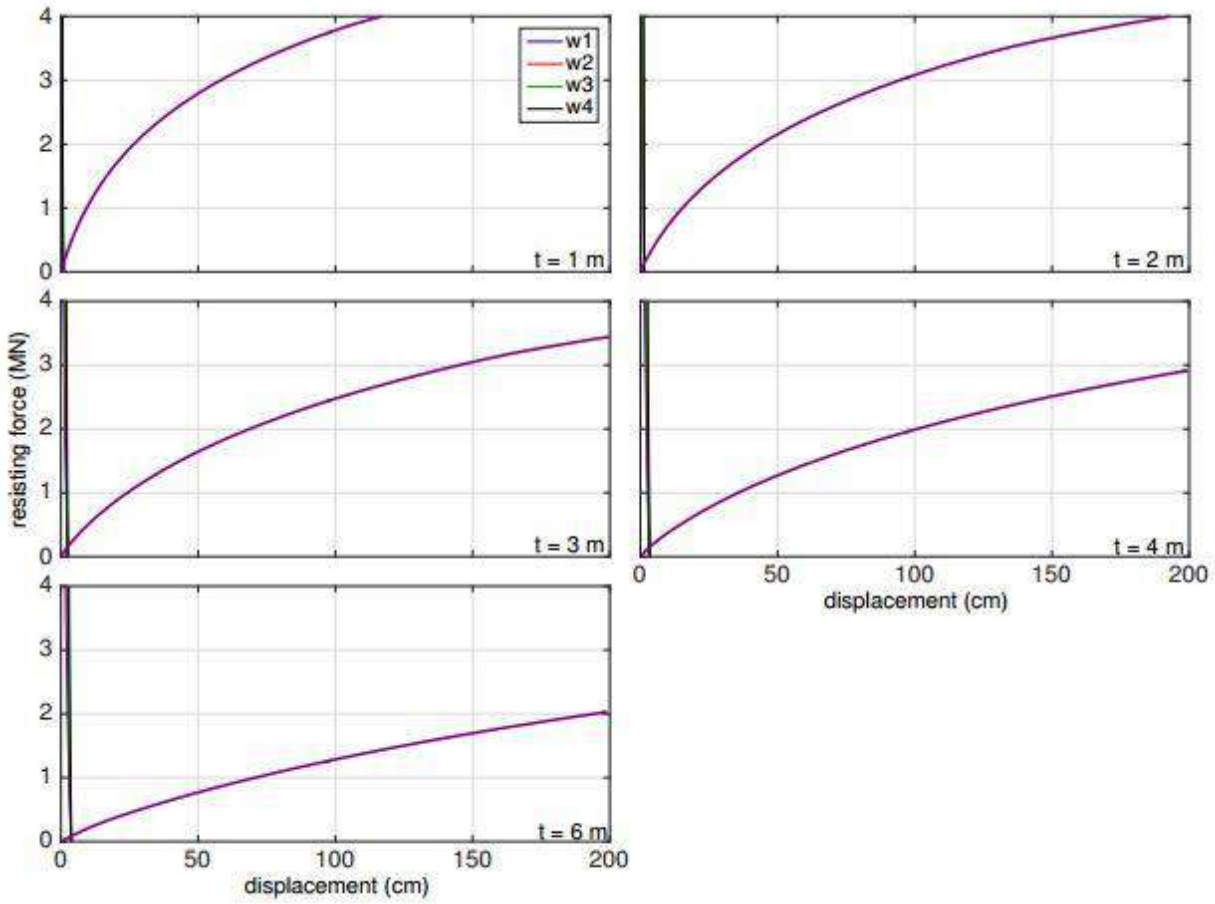

Figure 5.6 Determination of compatible displacement from pushover and slope deformation curves for five liquefiable layer thicknesses and four embankment crest widths with a 6.0-m crustal thickness and 0.6-m diameter shaft

Table 5.2 Compatible displacements (in cm) determined from figures 5.2-5.6 for the 0.6-m diameter shaft for four embankment crest widths.

Soil Profile	w1	w2	w3	w4
z1t1	4.86	6.35	9.18	12.34
z1t2	36.60	49.70	77.00	106.45
z1t3	95.00	120.02	156.20	187.00
z1t4	19.97	26.75	35.93	47.00
z1t5	60.45	77.19	119.05	165.05
z1t1	2.43	2.55	2.65	2.72
z2t2	10.02	11.00	12.04	12.80
z2t3	20.52	21.96	23.31	24.27
z2t4	5.80	6.18	6.53	6.78
z2t5	15.14	16.45	17.84	18.84
z3t1	0.81	0.83	0.85	0.86
z3t2	2.36	2.38	2.40	2.42
z3t3	3.66	3.68	3.70	3.71
z3t4	1.37	1.38	1.39	1.40
z3t5	3.23	3.26	3.29	3.31
z4t1	5.16	6.06	7.51	8.76
z4t2	30.72	42.40	59.91	77.00
z4t3	71.95	96.05	126.25	155.00
z4t4	15.24	19.14	23.85	37.53
z4t5	46.72	64.74	94.57	123.50
z5t1	3.92	4.43	4.97	5.38
z5t2	21.30	26.39	33.07	44.45
z5t3	45.90	51.78	64.20	76.35
z5t4	10.80	12.43	15.49	18.65
z5t5	31.65	39.35	48.74	61.16

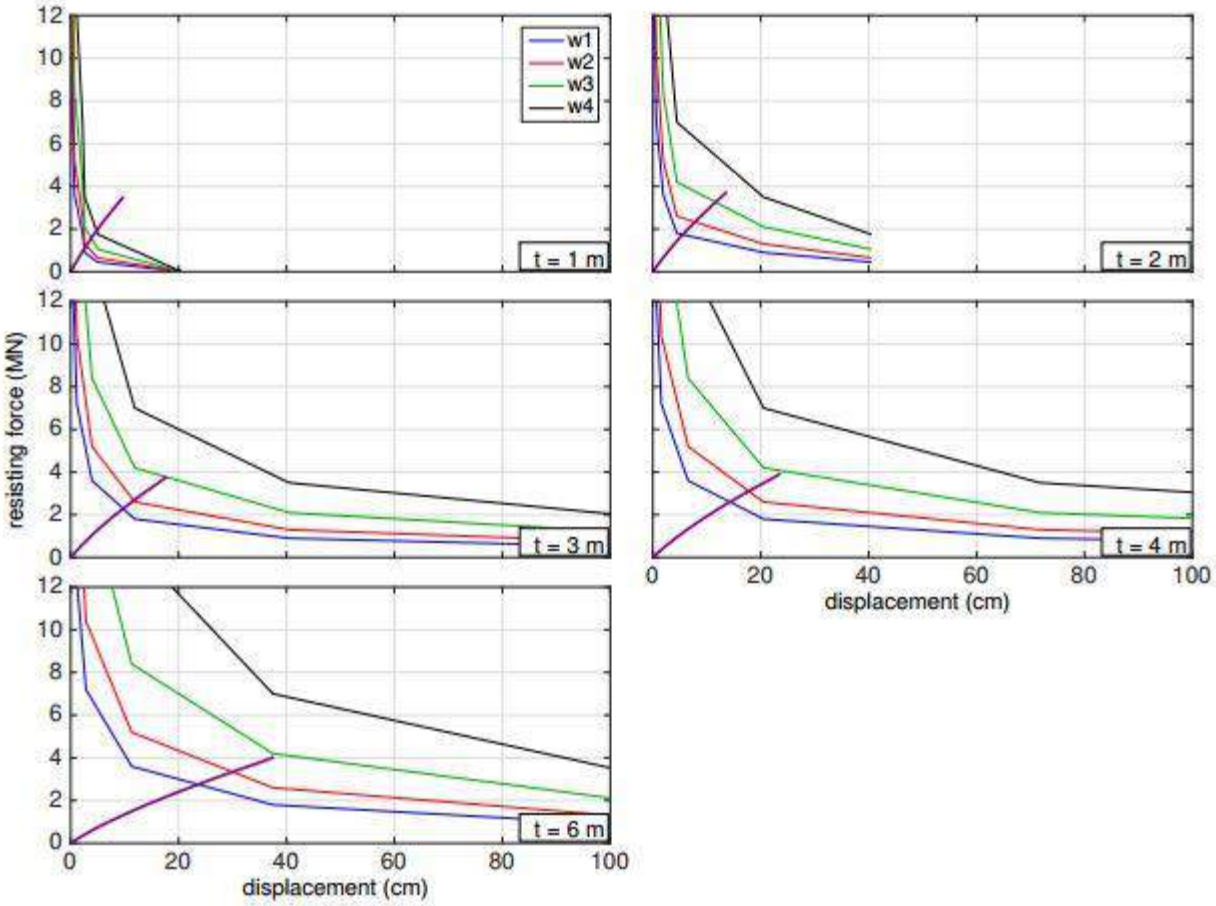

Figure 5.7 Determination of compatible displacement from pushover and slope deformation curves for five liquefiable layer thicknesses and four embankment crest widths with a 1.0-m crustal thickness and 1.4-m diameter shaft

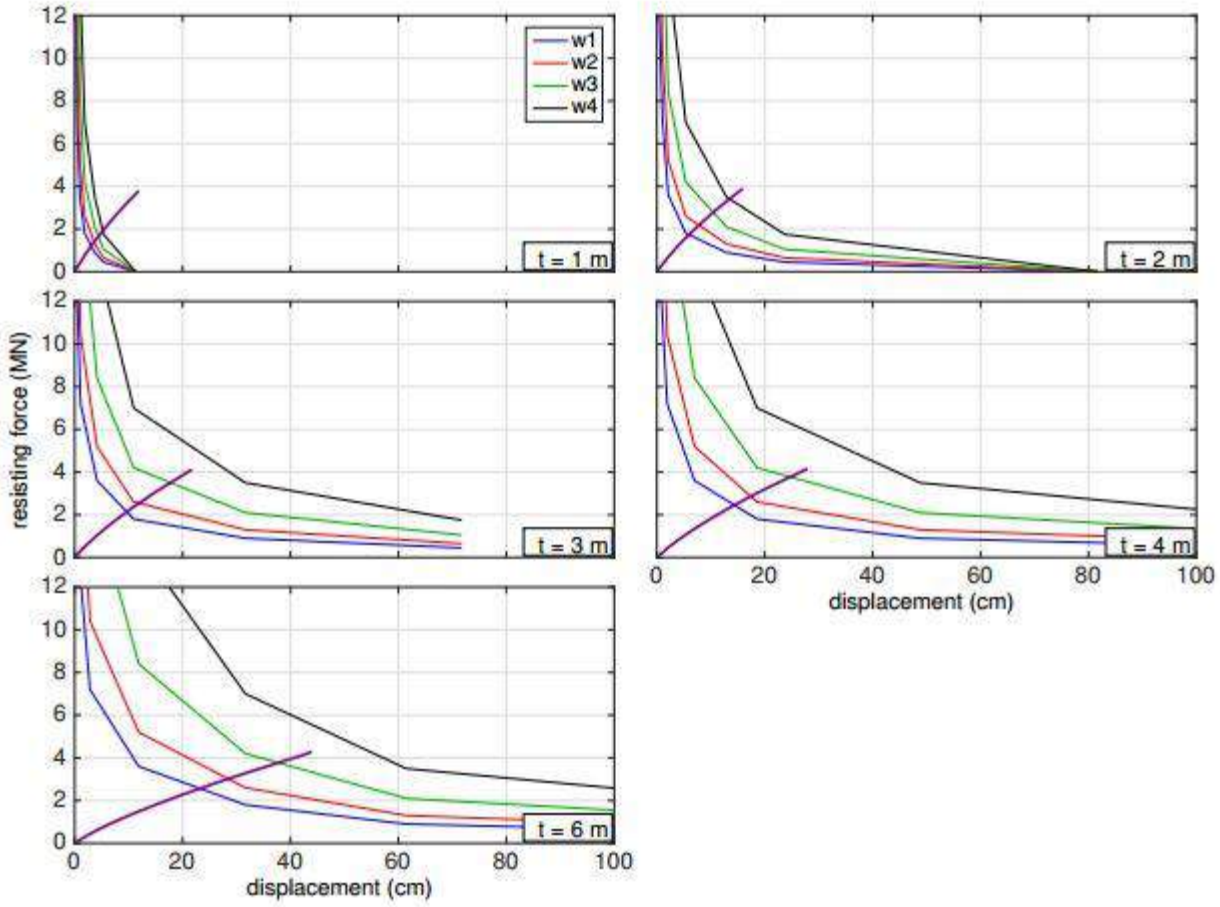

Figure 5.8 Determination of compatible displacement from pushover and slope deformation curves for five liquefiable layer thicknesses and four embankment crest widths with a 1.- m crustal thickness and 1.4-m diameter shaft

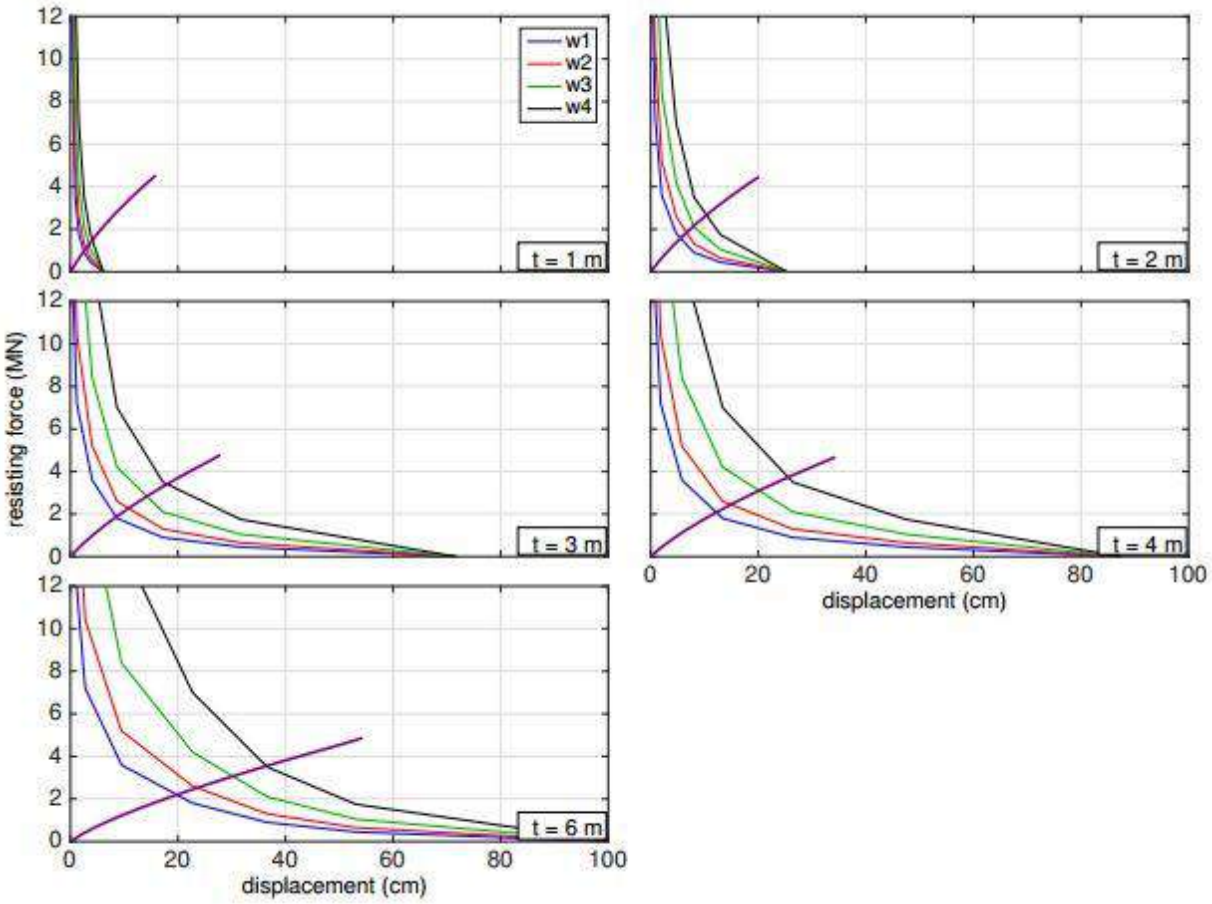

Figure 5.9 Determination of compatible displacement from pushover and slope deformation curves for five liquefiable layer thicknesses and four embankment crest widths with a 2.0-m crustal thickness and 1.4-m diameter shaft

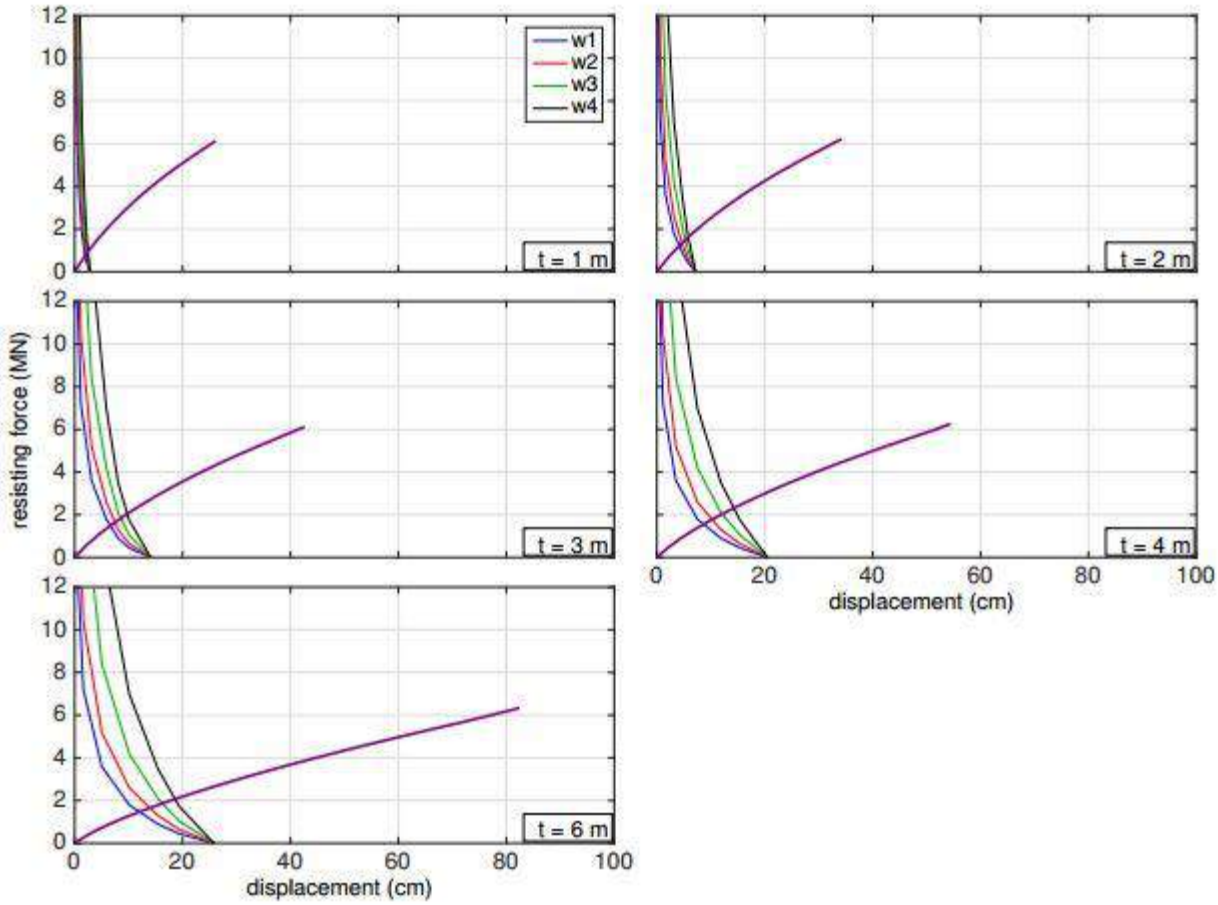

Figure 5.10 Determination of compatible displacement from pushover and slope deformation curves for five liquefiable layer thicknesses and four embankment crest widths with a 3.0-m crustal thickness and 1.4-m diameter shaft

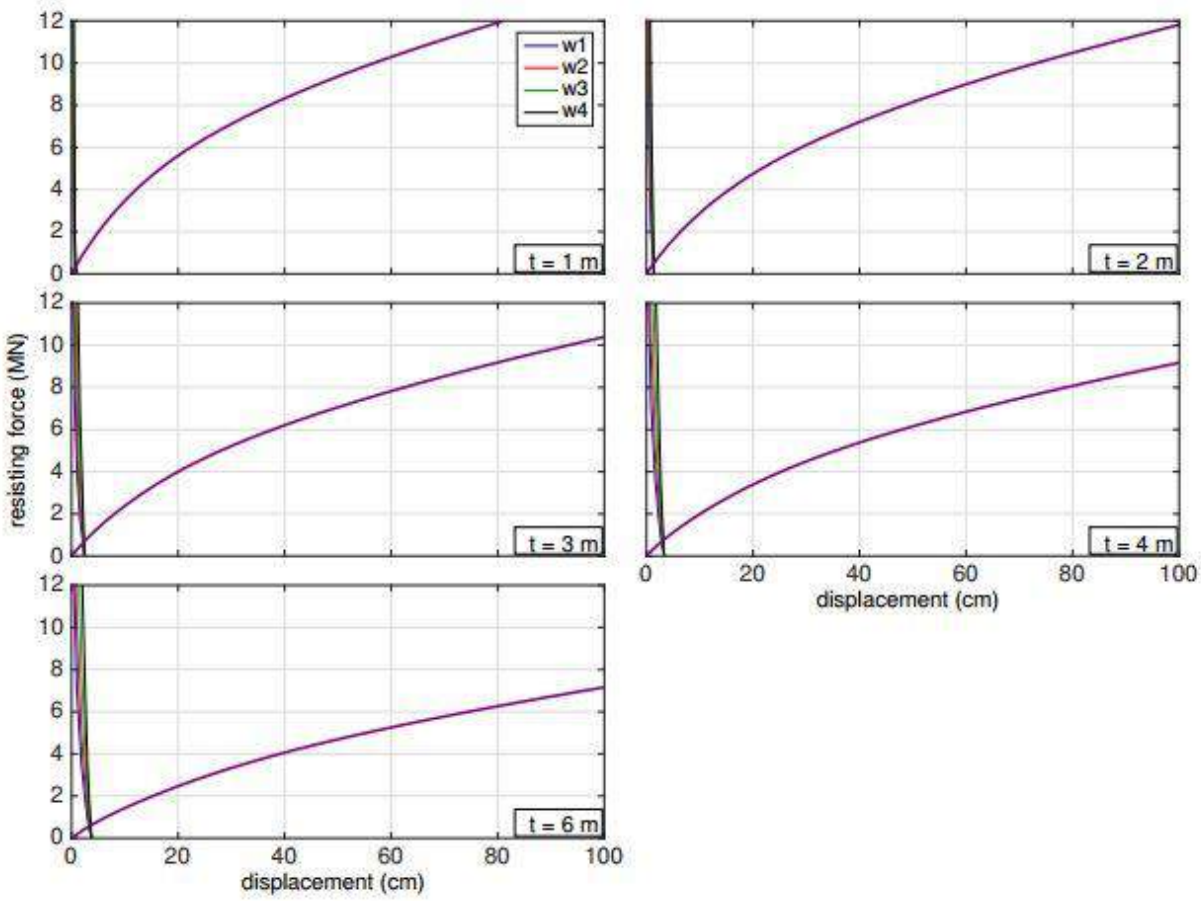

Figure 5.11 Determination of compatible displacement from pushover and slope deformation curves for five liquefiable layer thicknesses and four embankment crest widths with a 6.0-m crustal thickness and 1.4-m diameter shaft

Table 5.3 Compatible displacements (in cm) determined from figures 5.7-5.11 for the 1.4-m diameter shaft for four embankment crest widths.

Soil Profile	w1	w2	w3	w4
z1t1	2.51	2.89	3.82	4.79
z1t2	9.72	11.67	17.76	26.00
z1t3	23.61	30.03	39.10	62.50
z1t4	5.54	7.78	11.65	17.00
z1t5	14.29	17.78	24.70	40.00
z2t1	1.95	2.11	2.31	2.50
z2t2	6.62	7.47	8.56	9.76
z2t3	12.03	13.95	16.28	18.61
z2t4	4.17	4.68	5.30	5.82
z2t5	8.67	10.25	12.10	14.27
z3t1	0.70	0.75	0.79	0.82
z3t2	2.13	2.21	2.29	2.35
z3t3	3.26	3.38	3.51	3.59
z3t4	1.29	1.32	1.35	1.37
z3t5	2.84	2.97	3.10	3.19
z4t1	3.09	3.61	4.41	5.20
z4t2	9.67	11.91	17.78	25.50
z4t3	23.24	28.48	37.76	51.00
z4t4	5.93	7.80	10.46	13.48
z4t5	14.38	17.42	24.74	36.00
z5t1	2.50	2.92	3.47	4.08
z5t2	8.50	10.83	14.23	17.99
z5t3	19.80	23.57	30.20	36.40
z5t4	5.50	6.65	7.98	10.38
z5t5	12.20	14.90	20.10	25.54

5.3 Summary of Overall ESA Parameter Study Results

Certain overall trends were apparent from the results shown in figures 5.2–5.11 and tables 5.2 and 5.3. To expand upon these results, a second BNWF lateral spreading pushover analysis was completed with the compatible displacements of tables 5.2 and 5.3 taken as the surface

displacement in the displacement profile applied to the soil end of the *p-y* curve elements for all of the ESA parameter study cases. The results of these additional pushover analyses are shown in figures 5.12 and 5.13 for the 0.6- and 1.4-m-diameter shaft cases, respectively. The overall results of the ESA parameter study are discussed using the same scheme as that used for the 3D FEA, with the general effects of each considered parameter discussed independently in the following sections.

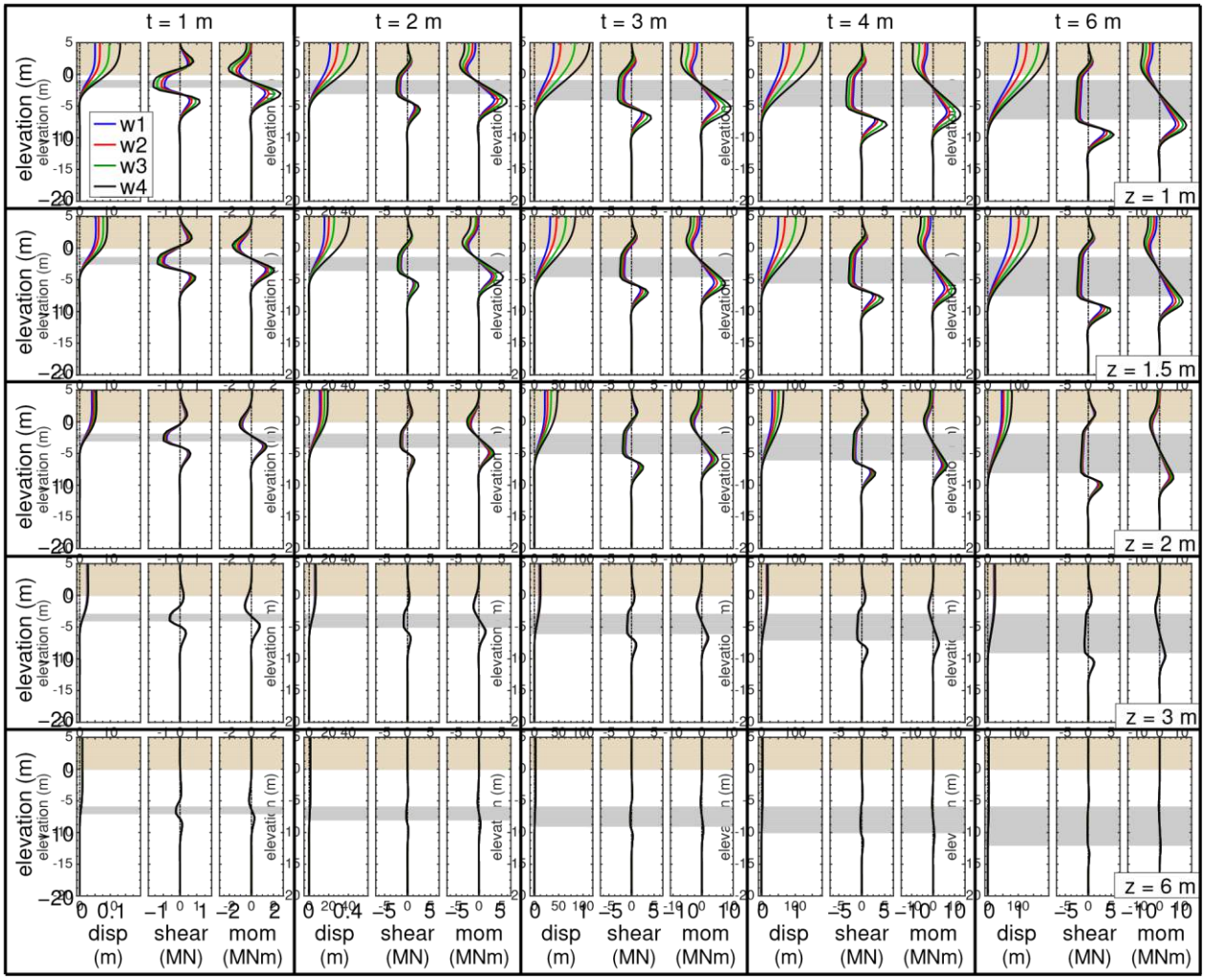

Figure 5.12 Shaft displacement, shear force, and bending moment demands at compatible displacement for all ESA parameter study cases for 0.6-m-diameter shaft.

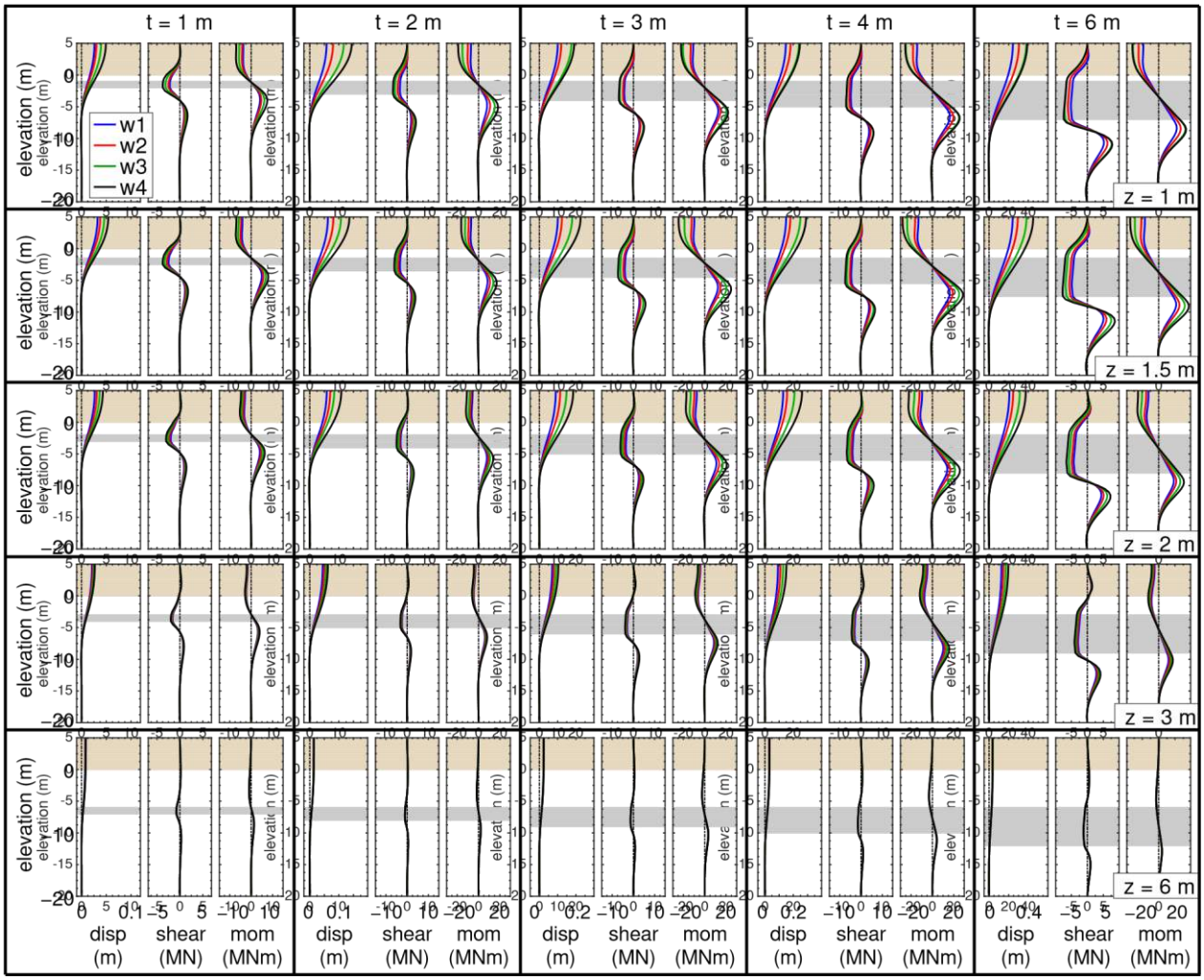

Figure 5.13 Shaft displacement, shear force, and bending moment demands at compatible displacement for all ESA parameter study cases for 1.4-m-diameter shaft.

5.3.1 Effects of Embankment Crest Width

The expected trend for increasing embankment width was apparent in the ESA parameter study results. A wider approach embankment pushed the slope stability/deformation curve upward, which pushed the corresponding compatible displacement to the right (i.e., a large value). Because the embankment width was only accounted for in converting the slope stability/deformation results from a force per length basis to a force only basis, no effect was observed on the pushover curves resulting from the BNWF analyses. The larger compatible

displacements naturally led to larger bending demands on the shafts when applied in the secondary BNWF analyses, as shown in figures 5.12 and 5.13, and were naturally larger for larger applied displacements.

5.3.2 Effects of Non-Liquefied Crust Thickness

Changes in the thickness of the non-liquefied crust had perhaps the greatest impact on the compatible displacement determined from the ESA procedure. As shown in figures 5.2–5.11 and tables 5.2 and 5.3, increasing the crustal thickness led to a marked decrease in the compatible displacement, given constant values of w, t, and diameter. The BNWF pushover curves, at least in regard to the running average shear force curves plotted in this study, were not affected much by changes in z, however, the slope stability/deformation analyses were significantly affected. This was a natural result of the pseudostatic slope stability analysis method adopted by the ESA procedure. Increasing the crust thickness increased the portion of the yield surface that passed through competent soil, which as shown in table 5.1 greatly increased the lateral yield acceleration required to achieve failure of the slope—even with the very weak liquefiable material in the soil profile. When applied to the rigid Newmark sliding block analysis using the Bray and Travasarou (2007) equation with M =7 and PGA=0.4, this increase in yield acceleration led to smaller displacement values as the yield accelerations approached or even exceeded the reference PGA. The use of a larger reference earthquake would clearly result in larger displacements for these thick crust cases; however, it would also result in larger displacements for the remaining cases, and the trend of decreasing compatible displacement with increasing crust thickness would not go away.

5.3.3 Effects of Liquefied Layer Thickness

Unlike the 3D FEA parameter study, where no consistent trend with respect to liquefiable layer thickness was observed aside from the expected concentration of shear force demands that come with a thinner layer, there was a clear trend in the ESA results based on the liquefied layer thickness. As shown in any of the compatible displacement determination plots of figures 5.2–5.11, for constant crust thickness and embankment width, an increased liquefiable layer thickness tended to push the slope stability/deformation curves to the right while simultaneously lowering the running average shear force curves from the pushover analysis. The net effects were an increase in the compatible displacement point and an apparent reduction in the demonstrated foundation pinning resistance. These effects were observed for all crust thicknesses and for both shaft diameters, but they were most significant for the thinner crust thickness cases, where the slope stability/deformation curves were most affected.

The mechanism behind this observation made sense in the context of the individual analyses that composed the ESA procedure. In regard to the slope stability analyses, increasing the thickness of the liquefiable layer for constant crust thickness increased the proportion of the failure surface that passed through weaker material. The results of this can be clearly seen in table 5.1, which shows that for constant z and resisting force V, the yield acceleration resulting in FS=1 decreases with increasing thickness. (Note that the ordering in table 5.1 is in regard to t1, t2, t3, t4, and t5, which indicate liquefiable layer thicknesses of 1.0, 3.0, 6.0, 2.0, and 4.0 m, respectively.) This decrease in yield acceleration resulted in an increase in deformation, given constant seismic demands across all cases. In regard to the BNWF analyses, the reduction in running average shear force in the middle of the liquefiable layer with increasing liquefiable layer thickness occurred because of decreased concentration of the shear demands from the

applied displacement profile. This was the same mechanism observed in the 3D models, where thin liquefiable layers displayed large (and concentrated) shear force demands, while layers that were more thick displayed lower maximum shear demands, and the shear force in the liquefiable layer was more spread out.

5.3.4 Effects of Shaft Bending Stiffness

Similar to the effects of embankment width on the ESA cases, the effects of shaft diameter was precisely as would have been expected. The increased bending stiffness for the 1.4-m-diameter shaft resulted in a steeper pushover curve from the BNWF analyses, which pushed the compatible displacement point to smaller values than those of the corresponding 0.6-m-diameter case. It is important to point out that the slope stability/deformation curves in the compatibility plots were not affected by the shaft diameter/stiffness; it only affected the pushover curves. The slope deformation curves in figures 5.2–5.6 for the 0.6-m-diameter shaft design are identical to those shown in figures 5.7–5.11 for the 1.4-m shaft. The only difference was the change in limits for the displacement axis (200 cm for the 0.6-m shaft; 100 cm for the 1.4-m shaft).

5.4 Comparison Between Results of 3D FEA and Simplified ESA Parameter Studies

Overall, the results of the ESA and 3D FEA parameter studies seemed to indicate the same general trends with corresponding changes in site geometry. Both studies clearly indicated the expected trends that increasing embankment width results in larger foundation demands, and larger and more stiff foundations provide more pinning resistance to lateral spreading deformations. It was also apparent that both studies indicated a similar interaction between the embankment width and crustal thickness in the observed foundation bending demands. For both studies, there was little significant difference with increasing embankment width for crustal

thicknesses ≥ 3 m (though the exact 'cutoff' thickness depended on the stiffness of the foundation). There were two areas of apparent difference between the modeling approaches that are worthy of further discussion: the apparent difference in the effects of crustal thickness, and the differences in the effects of liquefiable layer thickness. The mechanisms behind these two aspects are discussed separately in the following sections.

5.4.1 Differences in the Effects of Crust Thickness

On the basis of a comparison of figures 4.4 and 4.5 with figures 5.12 and 5.13, the effects of increasing crustal thickness on the results of the 3D FEA and ESA parameter studies appeared to be quite different. The lower compatible displacements in the ESA cases with z =3 and 6 m indicated quite a bit of foundation pinning resistance for the chosen scenario earthquake, and the minimal shaft bending demands for these cases reflected this expected pinning resistance. In contrast, the corresponding 3D cases in Figures 4.4 and 4.5 display much larger shaft bending demands. While this seems to indicate the opposite effect as observed in the ESA, it is important to keep two things in mind:

1. The 3D results were intrinsically tied to the assumption that there was a seismic event large enough to cause full liquefaction at depths of 3 or 6 m, and that this resulted in free-field lateral spreading displacements of 1 m despite the increase in competent crustal soil.
2. In the 3D results, apparent pinning resistance was driven by the difference between the different embankment width cases, as all of the cases were subject to the same 1-m free-field lateral spreading displacement.

In regard to the first point, the lower compatible displacements for the z =3 and 6-m cases in the ESA study were driven in part by the selected reference earthquake used in converting the yield accelerations to deformations. Were the reference earthquake to be assumed large enough

to cause the deformations inherently assumed in the 3D analyses (which may be unrealistically large), then the compatible displacements for the thicker crust cases would increase. This increase would not necessarily bring the shaft bending demands into alignment with the 3D models, but such behavior would not and should not be expected, if only because of the differences in how the soil response was represented in each model type. In regard to the second point, the key observation from the 3D analyses was that increasing the crust thickness resulted in a decrease in the influence of the embankment width, as all of the cases tended toward similar demands. This similarity was backed up by the ESA results, which, as shown in tables 5.2 and 5.3, showed very little difference in the compatible displacement states for the z2 and z3 cases (z =3 and 6 m, respectively) for different w values relative to the differences for thinner crustal thicknesses.

When interpreted in light of these two points, it is clear that the 3D FEA and ESA parameter study results told the same story in regard to the effects of crust thickness, just in different ways. From the ESA it was observed that increasing crustal thickness should lead to less foundation displacement because of the increase in seismic demands necessary to affect large lateral spreading deformations. From the 3D FEA and ESA results it was observed that given some amount of lateral spreading deformation at a site with a relatively thick crust, the differences between approach embankment width became negligible with increasing crust thickness. It is also important to note that both studies emphasized the importance of the entire soil profile on the overall response, rather than simply indicating that increasing embankment width would lead to increasing foundation bending demands. It is also important to note that both studies indicated that a crust thickness of 3 m was the apparent boundary between the two behavior mechanisms. For crusts ≤ 3 m, embankment width would affect differences in

foundation response, whereas for crusts > 3 m, little difference was observed in the foundation response with increasing embankment width. This 3-m value is certainly dependent on the ratio of soil to foundation stiffness, as the 1.4-m-diameter shaft cases displayed more differences across the embankment widths at z =3 m than the 0.6-m shaft; however, datawere insufficient in the results of the current studies to provide a relationship between these values.

5.4.2 Differences in the Effects of Liquefiable Layer Thickness

The differences and similarities in how the liquefiable layer thickness affected the overall results for the two parameter studies have previously been stated; however, it is important to consider the mechanisms for these differences and the potential implications in terms of model verification. As with the effects of crust thickness discussed in the previous section, the ESA results revealed a mechanism for the system that was masked by the approach adopted in the 3D FEA, in which all of the cases were subjected to the same free-field displacement. It is apparent that the model trends did not disagree but, instead, offered different insights into the problem. The trend evident in the ESA cases, in which increased liquefiable layer thickness resulted in a greater compatible displacement point (and corresponding foundation demand), makes inherent sense in the context of the problem. The surficial deformation from lateral spreading is due to the accumulation of shear strain over the height of the soil profile. As the largest shear strains develop in the liquefied material, increasing the scope of the liquefiable layer will naturally result in larger surface deformations. The apparent discrepancy suggested by the 3D cases, that given everything else remaining constant there is no definite difference in the shaft bending demands for changes in liquefiable layer thickness, is, again, intrinsically tied to the assumption of equal deformations for all of the 3D cases. This provides no other information beyond the fact that, given two soil profiles that have undergone equal surficial lateral spreading displacements (and

similar overall shear strain profiles), the models suggested that there would be no discernible trend in how different liquefiable layer thicknesses affect any embedded foundations.

5.5 Summary

A series of simplified equivalent static analyses (ESA) were carried out using the procedure set forth by Ashford et al. (2011) and Caltrans (2011) for the 200 distinct cases previously analyzed using 3D FE models and discussed in Chapter 4. These ESA models consisted of two separate sub-models: a beam on nonlinear Winkler foundation (BNWF) pushover analysis carried out with finite element or finite difference models, and a slope stability/deformation analysis carried out with pseudostatic limit equilibrium slope stability models combined with Newmark rigid sliding block analyses. The necessary sub-models were developed and analyzed for each of the separate site geometries, and the force-displacement results obtained from each sub-model and for each case were compared to determine the compatible displacement state for each combination of site geometric parameters. The overall results of these ESA models were presented and discussed, and it was shown that the trends suggested by the overall data set make sense in the context of the problem. The ESA results were also compared to the corresponding results from the 3D FEA parameter study, and they both agreed with and supplemented each other. The similarities in the trends and results obtained from the 3D FEA and ESA studies provide important verification of the two modeling approaches. The agreement between the two model types also provides increased confidence in the results returned by the simplified ESA approach, and it emphasizes the strengths of this approach, which is undoubtedly the more practical modeling approach of the two.

Chapter 6 Summary and Conclusions

6.1 Summary of Research

Field observations from numerous earthquakes have shown that there can be huge demands on piled abutments because of deformations of the bridge approach embankments caused by earthquake-induced liquefaction in the underlying soils. It has also been observed that the displacement in the soils near the abutment are often less than the free-field displacements away from the foundation, and it is understood that the resistance provided by the bridge foundation results in a reduction in the near-field soil displacements, and subsequently a reduction in the foundation demands relative to what they would be under the full free-field deformations. The design approach for lateral spreading for the approach embankment case is based on the pile pinning concept, in which it is assumed that the resisting forces developed in the foundations and superstructure during lateral spreading can be significant relative to the driving inertial forces.

Because of the complexity of the lateral spreading problem, and the difficulties associated with rigorously modeling every aspect in the course of engineering design, equivalent static analysis (ESA) procedures based on sound judgment and reasonable simplifying assumptions have been developed to aid in the design of foundations for this case. In this research, a parameter study of 200 distinct cases was undertaken by using both 3D finite element analysis (FEA) and the lateral spreading ESA procedure detailed by Ashford et al. (2011) and Caltrans (2011). The case matrix for this parameter study comprised different combinations of approach embankment width, non-liquefiable crust and liquefiable layer thickness, and shaft diameter/stiffness. The intentions of this study were two-fold: (1) to attempt to quantify the effects of 3D site geometry on the foundation response to the demands of lateral spreading with

the ultimate goal of providing guidance on the expected level of foundation pinning for different site layouts; and (2) to verify the lateral spreading ESA procedure through comparison of the results of the corresponding cases from the 3D FEA and ESA parameter studies. The research outcomes and conclusions gained in the pursuit of these primary research objectives are summarized in the following discussion, along with other miscellaneous lessons learned along the way.

6.2 Research Outcomes and Conclusions

Two sets of models were developed and analyzed to investigate the effects of various geometric site parameters on the response of a single deep foundation to the demands of liquefaction-induced lateral spreading and lateral soil deformation: (1) a series of 3D FE models using a continuum description of the soil, beam-column elements for the foundation, and the beam-solid contact element of Petek (2006) to consider the soil-foundation interaction; and (2) a series of beam on nonlinear Winkler foundation (BNWF) and pseudostatic limit equilibrium slope stability models developed and analyzed following the procedure set forth by Ashford et al. (2011) and Caltrans (2011).

This modeling effort provided further evidence that consideration for the 3D geometry of the site is an important factor in the analysis of bridge foundations subject to lateral spreading, and it was determined that for a given level of lateral spreading deformation, the lateral response of the foundation for a particular site is governed by the interaction of multiple site parameters, including the location and size of the liquefied layer, the width of the approach embankment, and the size and stiffness of the foundation. The comparison of the results from each modeling approach also provided important verification of both modeling approaches.

6.2.1 Effects of Site Geometry on Foundation Demands During Lateral Spreading

Both the 3D FEA and ESA cases demonstrated a general increase in foundation demands with increasing embankment width (given everything else constant). This is a somewhat obvious finding from the results of the ESA case, as embankment width is considered by multiplying the slope stability/deformation curves by the tributary embankment width, which clearly will increase the compatible displacement in all cases. The important findings with respect to embankment width are that a quantifiable effect was observed in the context of the fully three-dimensional description of the problem provided by the 3D models, and that the importance of the embankment width on the foundation response depends on other aspects of the system, such as the thickness of the non-liquefied crust and the size and stiffness of the foundation. The other "expected" outcome from both modeling approaches was the observation that given all else constant, increasing the foundation size and stiffness leads to greater pinning resistance and less foundation deformation. That both of these expected trends were evident in the results for both modeling approaches provides confidence that they provide sensible results overall.

The results from the 3D models showed that, given constant deformation demands (and holding everything else constant), the importance of 3D geometry (i.e., embankment width) decreases with increasing crust thickness and identified a cutoff' thickness of approximately 3 m beyond which significant 3D effects should not be expected (though the exact value of this cutoff thickness is dependent on the foundation stiffness). The corresponding ESA cases identified a sharp decrease in foundation demands with increasing crust thickness, due primarily to a decrease in the likelihood of large lateral spreading deformations developing at all for these configurations. In addition to this observation that could not be made from the 3D FEA because of the loading conditions assumed, the ESA results agreed well with the 3D results in regard to

the reduction in importance of the embankment width on the foundation demands with increasing crust thickness; it was just masked somewhat by the small compatible displacements computed for these cases.

The 3D and ESA approaches demonstrated an expected concentration of foundation shear force demand with decreasing thickness of the liquefiable layer. This was a natural consequence of both the adopted simplified applied free-field displacement profile and the underlying mechanics of the problem. While the 3D FEA displayed no discernible trend in foundation response with changing liquefiable layer thickness—given equal surface displacement, similar strain profiles, and everything else constant—the corresponding ESA cases showed an increase in foundation deformation for increasing liquefiable layer thickness. This increase was due to the reduction in yield acceleration for the slope stability considerations brought about by an increase in the proportion of the yield surface passing through liquefied material.

6.2.2 Verification of Simplified Lateral Spreading ESA Procedure

The overall agreement in the qualitative and quantitative assessments of the results obtained from the 3D FEA and simplified ESA modeling efforts offers important verification of each modeling approach and the assumptions associated with each. Though 3D effects are handled in the ESA procedure in a somewhat *ad hoc* manner, the net effect on the results is consistent with the 3D FEA, which explicitly consider the three-dimensionality of the problem. Both approaches provided consistent information in regard to the other geometric effects, particularly with respect to the thickness of the non-liquefied crust. Additionally, the strengths of the ESA procedure were highlighted through the comparison of the two modeling approaches; namely that the assessment of the foundation demands provided by the ESA explicitly accounts for the expected seismic demands and corresponding free-field lateral spreading deformations at

a particular site. This is not considered in the current application of the 3D models, though it could be considered through dynamic effective stress analysis using a similar 3D modeling approach.

6.2.3 First-Order Assessment of Expected Foundation Pinning

On the basis of the clear evidence of geometric site effects on the foundation response to the simulated lateral spreading demands in the parameter studies, particularly in regard to the width of the approach embankment and the thickness of the non-liquefied crust, a chart was developed with which to obtain a first-order estimation of the expected level of foundation pinning at a given site. This chart (shown in figure 4.38) was based on the results of the 3D FEA parameter study and frames the expected level of foundation pinning in terms of the ratio of the foundation deformation to the applied free-field lateral spreading deformation. With this chart, it is possible to obtain an idea of the expected level of foundation pinning, given knowledge of two most important geometric features identified in this research: the width of the embankment and the thickness of non-liquefiable crust. Caution should be used in the application of this chart, as it is not a substitute for a more rigorous analysis. Instead it offers insight that can be used to inform the design/analysis procedure that is most applicable to the site (e.g., should the restrained or unrestrained ESA cases be used), as well as an independent check for the results of a simplified ESA or other analysis of the problem.

As a final note in this discussion, it is of interest to evaluate the results summarized in the estimation On the basis of the discussion presented in Chapter 5, it is clear that the primary advantage of the application of the ESA procedure to the parameter study cases lies in the differences in what each modeling approach (i.e., 3D FEA and ESA) returns. Whereas the 3D FEA cases provide information on the effects of site geometry, given equal surficial lateral

spreading demands for all cases, the ESA cases provide information on the level of lateral spreading deformation that should be expected for each geometric combination. So while the chart developed from the 3D FEA states that very little near-field deformation reduction should be expected for a site with a 6-m thick crust, the findings from the corresponding ESA cases show that very large seismic demands are necessary to affect significant lateral deformations for such soil profiles. Therefore, it may not be overly important that the free-field and near-field deformations are the same if the deformations in general are less than 5 cm. This difference in the information provided by each modeling approach reinforces the importance of the ESA and the caution that should be applied if the chart developed in the work is used.

References

American Association of State Highway and Transportation Officials (AASHTO) (2010). *LRFD Bridge Design Specifications*. Washington, D.C., 5th edition.

American Petroleum Institute (API) (2007). *Recommended Practice for Planning, Designing and Constructing Fixed Offshore Platforms–Working Stress Design*. API Recommended Practice 2A-WSD (RP 2A-WSD), 21st edition. Errata and Supplement 3, October 2007.

Armstrong, R. J., Boulanger, R. W., and Beaty, M. H. (2014). "Equivalent static analysis of piled bridge abutments affected by earthquake-induced liquefaction." *Journal of Geotechnical and Geoenvironmental Engineering, ASCE*, 140(8), 04014046.

Ashford, S. A., Boulanger, R. W., and Brandenberg, S. J. (2011). "Recommended design practice for pile foundations in laterally spreading ground." *PEER Report No. 2011/04*, Pacific Earthquake Engineering Research Center, University of California, Berkeley.

Boulanger, R. W., Chang, D., Gulerce, U., Brandenberg, S. J., and Kutter, B. L. (2006). "Evaluating pile pinning effects on abutments over liquefied ground." *Seismic Performance and Simulation of Pile Foundations in Liquefied and Laterally Spreading Ground*, R. W. Boulanger and K. Tokimatsu, eds., GSP 145, ASCE. 306–318.

Boulanger, R. W., Curras, C. J., Kutter, B. L., Wilson, D. W., and Abghari, A. (1999). "Seismic soil-pile-structure interaction experiments and analyses." *Journal of Geotechnical and Geoenvironmental Engineering, ASCE*, 125(9), 750–759.

Boulanger, R. W., Kutter, B. L., Brandenberg, S. J., Singh, P., and Chang, D. (2003). *Pile Foundations in liquefied and laterally spreading ground during earthquakes: Centrifuge experiments and analyses*. Center for Geotechnical Modeling, University of California at Davis, Davis, CA. Rep. UCD/CGM-03/01.

Brandenberg, S. J., Boulanger, R. W., Kutter, B. L., and Chang, D. (2007a). "Liqufaction induced softening of load transfer between pile groups and laterally spreading crusts." *Journal of Geotechnical and Geoenvironmental Engineering, ASCE*, 133(1), 91–103.

Brandenberg, S. J., Boulanger, R. W., Kutter, B. L., and Chang, D. (2007b). "Static pushover analyses of pile groups in liquefied and laterally spreading ground in centrifuge tests." *Journal of Geotechnical and Geoenvironmental Engineering, ASCE*, 133(9), 1055–1066.

Bray, J. D. and Travasarou, T. (2007). "Simplified procedure for estimating earthquake-induced deviatoric slope displacements." *Journal of Geotechnical and Geoenvironmental Engineering, ASCE*, 133(4), 381–392.

Brinch Hansen, J. (1961). "The ultimate resistance of rigid piles against transversal forces." *Bulletin No. 12*, Geoteknisk Institute, Copenhagen, 5–9.

California Department of Transportation (Caltrans) (2011). *Guidelines on Foundation Loading and Deformation Due to Liquefaction Induced Lateral Spreading*. Internal Policy Proposal, February 2011.

CIMNE (2008). *GiD The Personal Pre and Post Processor*. International Center for Numerical Methods in Engineering (CIMNE).

Cubrinovski, M., Winkley, A., Haskell, J., Palermo, A., Wotherspoon, L. M., Robinson, K., Bradley, B. A., Brabhaharan, P., and Hughes, M. (2014). "Spreading-induced damage to short-span bridges in Christchurch, New Zealand." *Earthquake Spectra*, 30(1), 57–83.

Elgamal, A., Yang, Z., Parra, E., and Ragheb, A. (2003). "Modeling of cyclic mobility in saturated cohesionless soils." *International Journal of Plasticity*, 19, 883–905.

Faris, A. T., Seed, R. B., Kayen, R. E., and Wu, J. (2006). "A semi-empirical model for the estimation of maximum horizontal displacement due to liquefaction-induced lateral spreading." *Proceedings, 8th U.S. National Conference on Earthquake Engineering*, San Franciso, CA, April 18-22, Paper No. 1323.

Federal Highway Administration (FHWA) (2011). *Post-Earthquake Reconnaissance Report on Transportation Infrastructure: Impact of the February 27, 2010, Offshore Maule Earthquake in Chile*. W.-H. P. Yen, G. Chen, I. Buckle, T. Allen, D. Alzamora, J. Ger, and J. G. Arias, Publication No. FHWA-HRT-11-030, U.S. Department of Transportation, McLean, VA.

Geo-Engineering Extreme Events Reconnaissance (GEER) Association (2010a). *Geo-engineering Reconnaissance of the 2010 Maule, Chile Earthquake*. J. Bray and D. Frost, eds., Report No. GEER-022.

Geo-Engineering Extreme Events Reconnaissance (GEER) Association (2010b). *Geotechnical Reconnaissance of the 2010 Darfield (New Zealand) Earthquake*. R. A. Green and M. Cubrinovski, eds., Report No. GEER-024.

Geo-Engineering Extreme Events Reconnaissance (GEER) Association (2011). *Geotechnical Reconnaissance of the 2011 Christchurch, New Zealand Earthquake*. M. Cubrinovski, R. A. Green, and L. Wotherspoon, eds., Report No. GEER-027.

GEO-SLOPE (2016). *SLOPE/W*. https://www.geo-slope.com/products/slope-w, Accessed March 2017.

Ghofrani, A., McGann, C. R., and Arduino, P. (2016). "Influence of modeling decisions on 3D finite element analysis of two existing highway bridges subjected to lateral spreading." *Transportation Research Record: Journal of the Transportation Research Board No. 2592*.

Hamada, M. and O'Rourke, T., eds. (1992). *Case Studies of Liquefaction and Lifeline Performance During Past Earthquakes, Volume 1, Japanese Case Studies*. Technical Report NCEER-92-0001, National Center for Earthquake Engineering Research, Buffalo, NY.

Idriss, I. M. and Boulanger, R. W. (2008). *Soil Liquefaction During Earthquakes*. Earthquake Engineering Research Institute (EERI), MNO-12.

Janbu, N. (1973). "Slope stability computations." *Embankment Dam Engineering – Casagrande Volume*, R. C. Hirschfeld and S. J. Poulos, eds., John Wiley & Sons, New York. 47–86.

Ledezma, C., Hutchinson, T., Ashford, S. A., Moss, R., Arduino, P., Bray, J. D., Olson, S., Hashash, Y. M. A., Verdugo, R., Frost, D., Kayen, R., and Rollins, K. (2012). "Effects of ground failure on bridges, roads, and railroads." *Earthquake Spectra*, 28(S1), S119–S143.

LPILE (2010). *A Program for the Analysis & Design of Piles and Drilled Shafts Under Lateral Loads*. http://www.ensoftinc.com. Ensoft, Inc. Engineering Software, Austin, Texas.

Martin, G. R., March, M. L., Anderson, D. G., Mayes, R. L., and Power, M. S. (2002). "Recommended design approach for liquefaction induced lateral spreads." *Proc., 3rd Natl. Seismic Conf. and Workshop on Bridges and Highways*, MCEER-02-SP04, Buffalo, NY.

Matlock, H. (1970). "Correlations for design of laterally loaded piles in soft clay." *Proceedings of the 2nd Offshore Technology Conference*, Houston, TX. (OTC 1204), 577–594.

McGann, C. R. and Arduino, P. (2014). "Numerical assessment of three-dimensional foundation pinning effects during lateral spreading at the Mataquito River Bridge." *Journal of Geotechnical and Geoenvironmental Engineering, ASCE*, 140(8), 04014037.

McGann, C. R. and Arduino, P. (2015). "Numerical assessment of the influence of foundation pinning, deck resistance, and 3D site geometry on the response of bridge foundations to demands of liquefaction-induced lateral soil deformation." *Soil Dynamics and Earthquake Engineering*, 79, 379–390.

McGann, C. R., Arduino, P., and Mackenzie-Helnwein, P. (2012). "Development of simplified analysis procedure for piles in laterally spreading layered soils." *PEER Report No. 2012/05*, Pacific Earthquake Engineering Research Center, University of California, Berkeley.

McGann, C. R., Arduino, P., and Mackenzie-Helnwein, P. (2015). "A stabilized single-point finite element formulation for three-dimensional dynamic analysis of saturated soils." *Computers and Geotechnics*, 66, 126–141.

McKenna, F. (2011). "OpenSees: A framework for earthquake engineering simulation." *Computing in Science and Engineering*, 13(4), 58–66.

McKenna, F., Scott, M. H., and Fenves, G. L. (2010). "Nonlinear finite element analysis software architecture using object composition." *Journal of Computing in Civil Engineering*, 24(1), 95–107.

McKenna, F. T. (1997). *Object-Oriented Finite Element Programming: Frameworks for Analysis, Algorithms and Parallel Computing*. Ph.D. Dissertation, University of California, Berkeley.

Mokwa, R. L. and Duncan, J. M. (2001). "Laterally loaded pile groups and *p-y* multipliers." *Foundations and Ground Improvement: Proceedings of a specialty conference: June 9-13, Blacksburg, VA*, T. L. Brandon, ed., Geotechnical Special Publication No. 113. ASCE, 728–742.

Mokwa, R. L. and Duncan, J. M. (2003). "Rotational restraint of pile caps during lateral loading." *Journal of Geotechnical and Geoenvironmental Engineering, ASCE*, 129(9), 829–837.

National Cooperative Highway Research Program (NCHRP) (2002). *Comprehensive Specification for the Seismic Design of Bridges*. NCHRP Report 472, National Academy Press, Washington, D.C.

Newmark, N. M. (1965). "Effects of earthquakes on dams and embankments." *Géotechnique*, 15(2), 139–160.

OpenSees (2007). *Open System for Earthquake Engineering Simulation*. http://opensees.berkeley.edu. Pacific Earthquake Engineering Research Center (PEER), University of California, Berkeley.

Petek, K. A. (2006). *Development and Application of Mixed Beam-Solid Models for Analysis of Soil-Pile Interaction Problems*. Ph.D. Dissertation, University of Washington.

Reese, L. C., Cox, W. R., and Koop, F. D. (1974). "Analysis of laterally loaded piles in sand." *Proceedings of the 6th Offshore Technology Conference*, Vol. 2, Houston, TX. 473–483.

Reese, L. C. and Welch, R. C. (1975). "Lateral loading of deep foundations in stiff clay." *Journal of the Geotechnical Engineering Division, ASCE*, 101(GT7), 633–649.

Spencer, E. (1967). "A method of analysis of the stability of embankments assuming parallel inter-slice forces." *Géotechnique*, 17(1), 11–26.

Wang, C.-H. (2003). *Prediction of the Residual Strength of Liquefied Soils*. Ph.D. Dissertation, University of Washington.

Washington State Department of Transportation (WSDOT) (2011a). *Bridge Design Manual (LRFD)*. Technical Manual M 23-50.05, May 2011.

Washington State Department of Transportation (WSDOT) (2011b). *Geotechnical Design Manual (LRFD)*. Technical Manual M 46-03.04, April 2011.

Youd, T. L. (1993). "Liquefaction-induced damage to bridges." *Transportation Research Record No. 1411*, 35–41.

Youd, T. L., Idriss, I. M., Andrus, R. D., Arango, I., Castro, G., Christian, J. T., Dobry, R., Finn, W. D., Harder, L., Haynes, M. E., Ishihara, K., Koester, J. P., Liao, S. S. C., Marcuson, W. F., Martin, G. R., Mitchell, J. K., Moriwaki, Y., Power, M. S., Robertson, P. K., Seed, R. B., and Stokoe, K. H. (2001). "Liquefaction resistance of soils: Summary report from the 1996 NCEER and 1998 NCEER/NSF workshops on evaluation of liquefaction resistance of soils." *Journal of Geotechnical and Geoenvironmental Engineering, ASCE*, 127(10), 817–833.

Zha, J. (2004). "Lateral spreading forces on bridge abutment walls/piles." *Geotechnical Engineering for Transportation Projects*, M. K. Yegian and E. Kavazanjian, eds., GSP 126, ASCE. 1711–1720.

Zhang, G., Robertson, P. K., and Brachman, R. W. I. (2004). "Estimating liquefaction-induced lateral displacements using the standard penetration test or cone penetration test." *Journal of Geotechnical and Geoenvironmental Engineering, ASCE*, 130(8), 861–871.